Simulation studies of the expected background for X-ray missions

Diploma Thesis

submitted by
Sabina Pürckhauer

January, 2015

Institut für Astronomie und Astrophysik
High Energy Astrophysics
Kepler Center for Astro and Particle Physics
Mathematisch-Naturwissenschaftliche Fakultät
Eberhard Karls Universität Tübingen

Meinem Vater Peter Pürckhauer
(1955-2005)
Für das Leben, das er mir ermöglicht hat
- in vielerlei Hinsicht -

Zusammenfassung

Simulationen zur Funktionalität und zum Hintergrund von astronomischen Instrumenten für Weltraummissionen gehören heute zu den Schlüsselpunkten in der Vorbereitung eines Projekts. Dabei kann der Einfluss der unterschiedlichen Bestandteile der Detektor- und Teleskopgeometrie, wie beispielsweise Abschirmungen oder die Position elektronischer Komponenten, getestet und optimiert werden, ohne dabei große Mengen an Zeit und Material für Labormessungen zu benötigen. Eine Möglichkeit, diese Simulationen durchzuführen, bietet das Monte-Carlo-Simulations-Toolkit Geant4, welches u.a. vom europäischen Kernforschungszentrum CERN entwickelt und bereitgestellt wird. Es erlaubt die Untersuchung von Wechselwirkungen zwischen Teilchen und Materie bei Vorgabe einer detaillierten Beschreibung des Aufbaus sämtlicher Bauteile eines Instruments sowie einer sorgfältig ausgewählten Liste an physikalischen Prozessen.

Diese Arbeit soll zu Beginn einen kurzen Überblick über die Geschichte und die Handhabung des Geant4-Codes geben. Zudem wurden verschiedene Versionen des Codes gegeneinander getestet, um die Vergleichbarkeit der Ergebnisse bezüglich der z.T unterschiedlich implementierten physikalischen Prozesse zu gewährleisten.
Neben diesen allgemeinen Untersuchungen beschäftigt sich die Arbeit mit Simulationen zu unterschiedlichen astronomischen Röntgenobservatorien. So wurden für eROSITA, eine geplante Weltraummission, die 2016 gestartet werden soll, Simulationen der Quanteneffizienz der verwendeten pnCCDs durchgeführt, welche die Ergebnisse aus vorangegangenen Laborexperimenten bestätigen sollten und auch haben.
Des Weiteren wurde eine bildgebende Methode zur Positionsrekonstruktion von Röntgenquellen in bekannter Entfernung mit Hilfe einer Comptonkamera untersucht sowie die Änderungen in der Quanteneffizienz, die dabei durch unterschiedliche Aufbauten wie Anzahl, Material und Dicke der sensitiven Schichten entstehen. Im Vergleich zu früheren Arbeiten auf diesem Gebiet wurde für die Positionsrekonstruktion nicht die Näherung von so genannten Ereigniskreisen verwendet, sondern ein realistischerer Ansatz mit Ellipsen untersucht.
Die gefundenen Ergebnisse wurden dann zur Untersuchung der Vorgänge im Polarimeter eines Teststands im institutseigenen Labor verwendet, dessen Aufbau dem eines Comptonteleskops entspricht. Hierbei wurden neben der Positionsrekonstruktion auch die homogene Ausleuchtung der Detektoren und der Fluoreszenzhintergrund, der von Quellphotonen beispielsweise in den umgebenden Abschirmungen induziert wird, untersucht. Die Ergebnisse der Simulation trugen zum Verständnis der Linienbildung im Energiespektrum der Labormessung entschieden bei.
Schließlich wurde der Einfluss des kosmischen Röntgenhintergrunds, weicher Protonen aus solaren Winden sowie hochenergetischer Protonen aus der kosmischen Strahlung auf den IXO Wide Field Imager analysiert, einem Instrument, das in weiterentwickelter Form für die ESA-Mission ATHENA verwendet werden soll, deren Start für 2028 geplant ist. Zudem wurde die Abschirmung des Hintergrunds mit Hilfe eines *Graded-Z shields* untersucht. Es sollten dabei sowohl die Simulationsergebnisse, die im Rahmen einer Dissertation an der Universität Darmstadt gefunden wurden, bestätigt wobei zwei verschiedene Geometrien und Materialien des Schildes getestet werden.

Abstract

Simulations of functionality and of background effects of astronomical instruments designed for space missions are one of the key points in the preparation phase of a project. The influence of the various geometry parts of the detector and the telescope like shieldings or the position of electronic components as well as the detector response for the required energy range can be tested and optimised without spending large amounts of time and material for laboratory measurements. Such simulations can be performed e.g. by using the Geant4 Monte-Carlo simulation toolkit developed among others at the European nuclear research centre CERN. It allows to study interactions of radiation with matter after the implementation of a user-defined, detailed description of all parts of an astronomical instrument as well as of a carefully chosen list of physical processes.

After an introduction to X-ray astronomy, this work gives a short overview of the history and the handling of the Geant4 code. Also, various versions of the code are tested against each other to ensure comparability of the results focusing on the occurring physical processes.
Besides these general studies, this work describes dedicated simulations for several astronomical X-ray observatories. For eROSITA, a future space mission that will be launched in 2016, simulations are performed to confirm the results regarding the quantum efficiency for the pnCCDs found in former laboratory measurements. By comparison the results are in good agreement.
Furthermore, an imaging method for the position reconstruction of X-ray sources in a known distance by a Compton camera is studied as well as differences in quantum efficiency appearing for various configurations of the telescope like the number, the material and the thickness of sensitive detector layers. Compared to former works on this topic, instead of using the approximation of event circles for the reconstruction of position, realistic ellipses are studied. The results found are used for the analysis of the processes in a Compton polarimeter operated in a laboratory of the institute. Besides the reconstruction of the source position also the homogeneous illumination of the detectors and the fluorescence background induced by the interaction of source photons with the detector surroundings are analysed. The results explain the lines of the energy spectrum found for the laboratory measurement very well.
Finally, the effect of the cosmic X-ray background as well as of low energy protons originating from solar winds and high energetic cosmic rays on the IXO Wide Field Imager (WFI) are studied. The WFI is an instrument that shall be further developed and used at the ATHENA mission that is planned to be launched in 2028. Additionally, the reduction of the background with the help of a *Graded-Z shield* is analysed. Thereby, the results found in a former simulation in the context of a dissertation at the University of Darmstadt, Germany, should be re-evaluated whereby two compositions of the shield in terms of geometries and materials are tested.

Contents

1 Introduction

Throughout time, people were fascinated by the sky and the celestial bodies moving within, making astronomy one of the oldest field of interests in human history. Instrumental astronomy and with it the systematic examination of the universe started in 1609 when Galileo Galilei pointed his telescope to the sky for the first time in order to study the surface of the Moon. Since then, telescopes and astronomical instruments have been improved and new astrophysical domains have been established. In the mid 20th century, the step from ground-based to space-borne astronomy was taken. Among the fields of research in modern astronomy, one important branch is X-ray astronomy that leads to a better understanding concerning some of the most unusual and extreme sources and processes in our universe.

1.1 A short history of X-ray astronomy

In 1895 Wilhelm Conrad Röntgen studied the path of electrons in a cathode ray tube. In order to shield his experiment from stray light, he covered the tube in black cardboard. By chance, he found that a screen of photosensitive material near the tube showed fluorescence effects although no visual light escaped from the tube. He recognised it as a new kind of radiation being able to penetrate a variety of different materials. This radiation differed from any radiation known so far therefore he called it X-radiation.

It took several decades until X-ray technologies found their way into astronomical research. Earth's atmosphere is transparent to visual light and partially transparent in the radio, infrared and UV-range of the electromagnetic spectrum. X-rays and higher energetic gamma rays ionize the molecules in the atmosphere and are absorbed in this process, so they cannot be detected by ground-based telescopes and even hardly with balloon-based instruments. Figure 1.1 summarises the opacity of Earth's atmosphere for electromagnetic radiation.
It was not until 1949 when the first rocket-based mission was launched and a detector could be brought to an altitude of 87 km where Earth's atmosphere became sufficiently transparent that the first X-rays from an astrophysical source could be detected by Friedman et al. (1951). These 3 keV X-rays originated from the hot corona of the Sun, and most astronomers assumed that it would remain the only astronomical X-ray source strong enough to ever be detectable. Nevertheless, in 1962 the first extra-galactic X-ray source was found. When Riccardo Giacconi et al. searched for X-ray fluorescence of the Moon induced by the powerful solar winds, they detected a strong X-ray signal from a star inconspicuous in the visible light (13th magnitude). It was called Sco X-1 as it was the first X-ray source in the star constellation Scorpius (Giacconi et al., 1962).
As a consequence, about 75 years after Wilhelm Conrad Röntgen had observed the new radiation, the NASA[1] satellite Uhuru was launched in 1970. During its three year all-sky survey, 300 new X-ray sources were detected. With the data of this long-term measurement, X-ray radiation from sources like Sco X-1 could finally be explained. Today Sco X-1 is known to be a binary system consisting of a neutron star and a low mass companion star.

[1] NASA: National Aeronautics and Space Administration

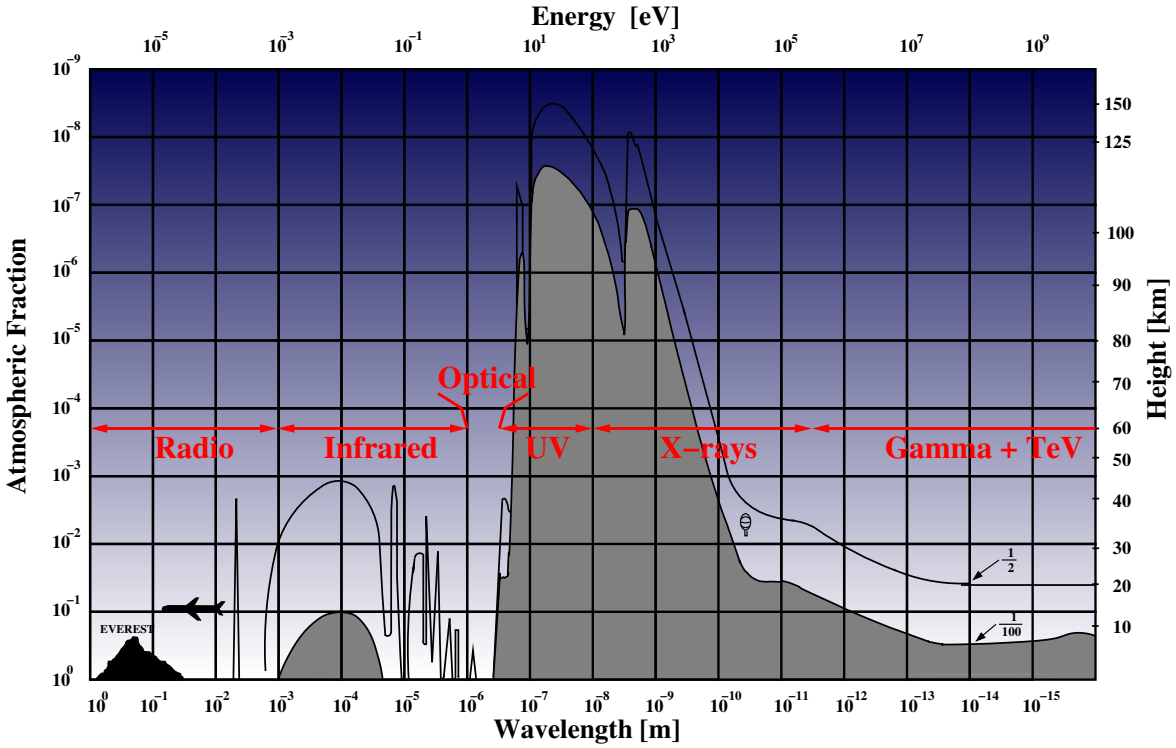

Figure 1.1 Molecules in the atmosphere absorb large parts of the electromagnetic spectrum originating from galactic or extra-galactic sources. In this image the solid line indicates an absorption of 50 % of the incident radiation whereas the top of the grey area corresponds to an absorption of 99 %. The scale *Atmospheric Fraction* gives the fraction of the atmosphere that lies above the corresponding height. While it is possible to observe optical and radio photons with ground-based telescopes, it requires satellites to detect high energetic X- and gamma rays. Image by Thomas Schanz and Chris Tenzer (Institut für Astronomie und Astrophysik Tübingen) based on an image by Giacconi et al. (1968).

The processes leading to the emission of X-rays and the sources showing these processes are briefly described in the Sections 1.2 and 1.3.
Other space missions followed, e.g. as ROSAT[2] launched in 1990 and performed an imaging survey of the whole sky which added 80,000 X-ray sources to the catalogue (Trümper et al., 1999).
Sky surveys were also performed in other energy ranges. One year after ROSAT, the Compton Gamma Ray Observatory by NASA began to study the sky in the gamma ray range. One of the instruments on board was COMPTEL, the first successful Compton telescope in the MeV range.

Currently, there are two large space missions focused on imaging in the X-ray band of the electromagnetic spectrum. The Chandra X-ray Obervatory was named after the Indian-American physicist Subrahmanyan Chandrasekhar, who found the upper mass limit for white dwarfs. The observatory is a NASA project that was launched in July 1999. Details about the mission as well as scintific results from the actual fifteen years of operation can be found in Weisskopf et al. (2014).

The European counter-part to Chandra is the ESA[3] project XMM Newton, launched in December of the same year. XMM is an acronym for **X**-ray **M**ulti-**M**irror, chosen because it contains three telescopes, each of which consists of 58 Wolter-type I mirror shells (Jansen et al., 2001). While Chandra has a high angular resolution of 0.5", XMM benefits from its large collecting area of 1500 cm^2 for each telescope. Results of the observatory are summarised in Schartel (2012).
For 2016 a new mission is planned. The eROSITA instrument on the joint Russian SRG mission is designed by the *Max-Planck-Institut für extraterrestrische Physik* in Garching, Germany, as the successor of the ROSAT mission and will perform an even more detailed survey of the X-ray sky.

The field of X-ray astronomy is very productive. There are further active as well as planned missions that cannot all be stated here. This thesis will have reference to some selected current missions.

1.2 Astronomical X-ray sources

Since the early 1960s, several sky surveys in X-rays were performed in order to catalogue and identify the X-ray sources. X-rays are emitted by a range of very different astronomical objects which are presented in the following.

1.2.1 Hot stars

Stars are traditionally categorized into seven main stellar classes–O, B, A, F, G, K and M–depending on their emitted light spectrum. From O to M, effective temperatures decrease while the occurrence of absorption lines in the spectrum increases. O stars can have surface temperatures above 50,000 K, whereas M stars reach only temperatures of about 2500 K (Novotny, 1973). According to Planck's radiation law (see Equation 1.7), this temperature is not high enough for the emission of photons in the X-ray energy range.

[2]ROSAT: ROentgenSATellit
[3]ESA: European Space Agency

Due to the Stefan-Boltzmann law, the irradiance j of a hot object depends strongly on its temperature T.

$$j = \sigma T^4 \tag{1.1}$$

In this formula σ is the Stefan-Boltzmann constant. At the surface of a hot star, this radiative flux can outweigh the gravitational pressure which binds the matter to the star. Particles will be accelerated away from the star, forming stellar winds. Therefore, O stars are known to suffer a mass loss of up to $10^{-4}\,M_\odot$ (solar masses) per year. Shock fronts and cooling zones inside these winds (Feldmeier et al., 1997) as well as strong magnetic fields (Gagné et al., 2011) can heat up the winds sufficiently to produce thermal X-rays.

X-rays are also detected from members of other stellar classes. Those cooler stars have convective zones that force hot plasma in the interior of a star to move outwards and cooler material from the surface to sink down. Through the movement of the plasma, generated by the high temperatures inside the star, a magnetic field is induced that can rise to the surface inside a convective bubble. For the Sun those bubbles are known as sun spots. At the surface those magnetic fields are converted into thermal energy, and act as the main heating process in the the corona of a star next to thermal conduction and mass flow. Through magnetic heating, coronal temperatures can reach several $10^6\,K$, enough to produce thermal X-rays (Withbroe and Noyes, 1977).

1.2.2 White Dwarfs

Main sequence stars with initial masses up to $8\,M_\odot$ end their lives as white dwarfs. There are different types of white dwarfs depending on this initial mass. Typically the progenitors of white dwarfs pass through phases of hydrogen and helium burning. After burning all helium (that remained in the core after the mass loss due to stellar winds in the red giant phase) to carbon, the nuclear fuel in the core is exhausted, radiative pressure decreases and gravitation dominates. The core collapses until the electron gas of the core degenerates. The pressure rises, bringing the collapse to an end. The remaining object is a white dwarf consisting usually of a carbon core with a thin helium atmosphere. Typical radii of white dwarfs with one solar mass are about 10,000 km.
The mass of a white dwarf is limited to the so called *Chandrasekhar mass* which is about $1.4\,M_\odot$. This is the maximum mass that can be supported by the degenerated gas of electrons. Some low mass stars never gain enough energy to start the helium burning process. Those stars later become helium white dwarfs with a typical mass of $0.5\,M_\odot$. On the other hand, some main sequence stars with masses between 8 and $11\,M_\odot$ can ignite carbon and can even produce neon and magnesium before reaching the core collapse phase. Those ONeMg white dwarfs come close to the Chandrasekhar limit with masses between 1.2 and $1.4\,M_\odot$ (Ryan and Norton, 2010).
If a white dwarf collects additional mass for instance by accretion and thereby exceeds the Chandrasekhar limit, the core pressure of the degenerated electron gas cannot withstand gravity and the white dwarf explodes in a thermonuclear explosion called supernova type Ia.

Because the nuclear burning stops when the white dwarf state is reached, single stars afterwards start the terminating cooling phase. With initial temperatures of about $10^6\,K$ they have enough thermal energy to produce soft X-rays and the star cools at an almost constant rate. The process is well understood and can be used to determine the age of white dwarfs (Salaris, 2008).

1.2.3 Cataclysmic variables

Cataclysmic variables (CV) are binary systems containing a white dwarf which accretes material from a regular companion star. Depending on their magnetic field CVs are divided into magnetic CVs or polars, intermediate polars and non-magnetic CVs. All types of CVs radiate X-rays but the processes leading to the emission depend on the strength of the magnetic field.

In *non-magnetic CVs* the white dwarfs have a magnetic field strength of $B \leq 10^4\,\mathrm{G}$ (Kuulkers et al., 2003). Therefore, an accretion disc can form around the compact object. Because the disc rotates with a higher velocity than the white dwarf, a boundary layer evolves between the surface of the dwarf and the innermost edge of the disc where the accreted matter is slowed down. In the course of this process kinetic energy is converted into thermal energy.
If the accretion rate is low, the material in the boundary layer cannot cool down efficiently and the layer increases, forming a hot corona around the white dwarf. Temperatures can rise up to $10^8\,\mathrm{K}$ and electrons in the surrounding of the star are accelerated to relativistic velocities. From this hot corona soft thermal X-rays can be observed (Hellier, 2001).
At higher accretion rates, the boundary layer becomes optically thick, cooling is more efficient and X-rays are produced by thermal Bremsstrahlung. Additionally, at a critical density, viscosity increases and the accreted matter can be transported to the hot surface of the white dwarf. Thereby the material abruptly releases its gravitational energy which leads to a so-called *dwarf nova outburst* (Kuulkers et al., 2003).

Polars have strong magnetic fields above $10^7\,\mathrm{G}$ that force the companion star to corotate with the white dwarf. A disc cannot emerge and the accreted matter follows the magnetic field lines, impacting on the dwarf in a single point near one of the magnetic poles. In a so called *accretion shock* the total kinetic energy is converted into an intense emission of soft X-rays (Hellier, 2001).

Intermediate CVs are in-between non-magnetic CVs and polars. The magnetic field is not strong enough to force the companion star to corotate. The stream of accreted matter is therefore forced to change direction with the altering magnetic field lines. Sometimes it is even possible to form a disc but the inner layer of those discs will be cleared from any matter by currents induced by the magnetic field at the border of the magnetosphere. Matter can only access the star's surface by following the magnetic field lines. There are several accretion points on the surface of the white dwarf producing X-rays by converting gravitational energy into thermal energy (Hellier, 2001).

Finally, all types of CVs can produce thermal X-rays during *classical nova outbursts*. By accreting hydrogen-rich matter from the companion star, the pressure of the degenerated material inside the white dwarf rises along with the temperature. If the temperature reaches a critical point, hydrogen reignites, leading to a *thermal runaway* producing temperatures of above $10^8\,\mathrm{K}$. In this process, thermal X-rays can be generated (Hellier, 2001).

1.2.4 Neutron stars and X-ray pulsars

Stars with main sequence masses of more than $11\,\mathrm{M}_\odot$ evolve by burning elements inside the core from hydrogen to silicon. The last burning process generates an iron core. Because no energy can be gained by the burning of iron, the nuclear fusion stops, initiating a core collapse. The pressure of the gravitational collapse is high enough to cause neutronization. In this process protons combine with the high energetic electrons from the degenerated gas to neutrons. The neutrinos that are additionally produced in this process take away large parts

of the energy. When the neutronized core becomes degenerated again, the pressure rises suddenly and the matter falling on the incompressible core is driven away in a supernova explosion (type II, Ib, Ic). The remaining object is a neutron star. Those stars have densities of above $10^{18}\,\mathrm{kg\ m^{-3}}$ and typical radii of about 15 km at $1.5\,\mathrm{M}_\odot$. The surface can reach temperatures of approximately $10^6\,\mathrm{K}$. The mass of a neutron star is below the Tolman-Oppenheimer-Volkoff limit at $M <$ 1-3 $\mathrm{M}_\odot$. This upper mass limit is not yet known precisely because the equation of state inside a neutron star is still not known (Weigert et al., 2010).

In addition to the production of thermal X-rays caused by the hot surfaces, X-rays can be generated via synchrotron radiation around rotating neutron stars called *pulsars*. When a star collapses into a neutron star, initial angular momentum will be increased with decreasing radius. Therefore, pulsars are very fast rotating objects. Additionally, the rotation induces a strong magnetic field of up to $10^8\,\mathrm{T}$ due to the movement of highly ionised plasma contained inside the neutron star. Those two effects are thought to lead to an acceleration of electrons in the surroundings of pulsars and to synchrotron radiation up to the X-ray energy range emitted in a very narrow emission cone. Due to the fast rotation this cone produces a typical periodic light curve characteristic for pulsars. The periodicity is of few milliseconds to some seconds. It is only due to the high density of the neutron star that the pulsar is not torn apart by the centrifugal forces (Weigert et al., 2010).

1.2.5 Black Holes

For cores with masses above the Tolman-Oppenheimer-Volkoff limit, the object remaining after the supernova explosion is a black hole (BH). Because of their high gravitation, BHs absorb all matter in their surroundings. Physical properties can only be obtained by the behaviour of matter in the gravitational field of a BH. Even light cannot escape from a certain radius around a non-rotating BH, which is called the *Schwarzschild radius* to be found at

$$r_\mathrm{s} = \frac{2\mathrm{G}M}{\mathrm{c}^2}, \tag{1.2}$$

where G is the gravitational constant, M the mass of the black hole and c the speed of light (Weigert et al., 2010).

BHs can be sub-classified into *stellar type black holes* (SBH) for masses $1\mathrm{M}_\odot < \mathrm{M} < 100M_\odot$, *intermediate mass black holes* (IMBH) for $100\mathrm{M}_\odot < \mathrm{M} < 10^6 M_\odot$ and *supermassive black holes* (SMBH) for masses up to $10^{10}\mathrm{M}_\odot$ (P. Natarajan, 2009).

Another way of classification is due to their physical properties. According to Ruffini and Wheeler (1971), for the calculation of the event horizon for a rotating BH the only externally observable parameters accessible are the mass, the angular momentum and the charge of the black hole (*no-hair theorem*). Because nothing can escape from within the event horizon, for the description of the BH all intrinsic properties can be neglected. Thus, excluding mass, there are four combinations of properties by which a BH can be classified.

The most simple is the *Schwarzschild BH*, which has neither a charge nor an angular momentum. As mentioned above, it has an event horizon at the Schwarzschild radius, the minimal orbit from which light can escape from the black hole.

A more complex version is the so called *Kerr BH*, which has an angular momentum but no charge. Because of its rotation, the Kerr BH can develop two horizons. The inner horizon is the Schwarzschild BH. However, there is also an outer horizon where the light is not yet

absorbed by the black hole, but forced to corotate. The area between the two horizons is called *ergosphere* and envelops the event horizon as an oblate spheroid evolving a bulge around the equatorial area while touching the inner horizon sphere at the poles. Due to the different rotation velocities depending on the orbit between the two horizons, accretion discs can form in this region. But, inside this ergosphere particles could still escape from the range of influence of the black hole by gaining energy from the rotation of the BH up to $v > 0.9c$ (Meier, 2012).

The remaining classes of BH are based only on theoretical models. No objects of these classes have been found in obervations yet. The *Kerr-Newman BH* can be described by adding an electric charge to a simple Kerr BH while a *Reissner-Nordström BH* has a charge but no angular momentum.

Black holes produce X-rays by various processes. The most luminous X-ray processes can be found around *active galactic nuclei* (AGN). In the centre of presumably all larger galaxies, super-massive black holes can be found. About 10 % of them are AGNs, having very high luminosities of up to $10^{46}\,\mathrm{erg\ s^{-1}}$. These are the major X-ray sources in the universe.
Because of the high gravitational force of the central black hole, the matter falling towards the compact object can form an accretion disc. As for other accretion processes depending on the accretion rate, the accretion discs can heat up to temperatures of about $10^6\,\mathrm{K}$.
Additionally, the surrounding of the AGNs are typically filled with corona-like hot ionized electrons. Through the movement of those charged particles, magnetic fields are produced that are converted into thermal energy heating up the corona even further. Thermal photons from the accretion disc are inverse Compton scattered at the hot electrons and reach X-ray energies. Characteristic line spectra can also be found superposed the inverse Compton spectrum depending on the abundances of elements inside the accretion discs and the surrounding corona (Gandhi, 2005).

1.2.6 SNR

Matter driven away in a supernova explosion gets strongly accelerated and thereby heats up the interstellar medium it passes. The emission nebulae that are created by those explosions are called *supernova remnants* (SNR) and are divided into three subclasses.
SNRs that form shell-like structures are called *shell type SNRs*. They have temperatures of about $10^6\,\mathrm{K}$ and emit mainly thermal X-rays.

Others, generated by a core collapse supernova, can contain a fast rotating neutron star in their centre. During the rotation, the neutron star loses energy. The freed energy results in a stellar wind of relativistic particles that generates shock fronts and forms a diffuse nebula of ultra-relativistic electrons around the central star. This form of a SNR is called a *pulsar wind nebula*. Inside those nebulae, the electrons produce X-rays by inverse Compton scattering and synchrotron radiation.

An intermediate form of these two types are the *composite SNR*, young pulsars that were able to create a pulsar wind, but have not yet blown away their surrounding shell structure. Therefore, X-rays from both features can be observed (Vink, 2012). Images of these three types of SNR are shown in Figure 1.2.

1.2.7 Hot gas

In general, all areas in space filled with hot gases, mainly heated by acceleration and shock fronts due to supernova explosions, produce thermal Bremsstrahlung. These gases like the

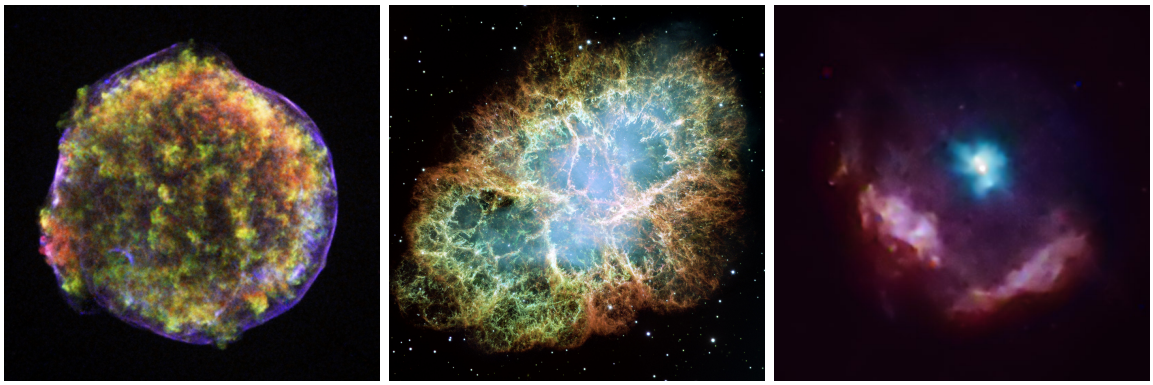

(a) ©NASA/CXC/Rutgers/J.Warren & J.Hughes et al. (b) ©NASA, ESA, J. Hester, A. Loll (ASU) (c) ©NASA/CXC/GSFC/F.P.Gavriil et al.

Figure 1.2 Examples of SNR classification types. In (a) a muliwavelength image of the tycho supernova 1572 SNR is shown. The spheric symmetrical shell structure is visible. Figure (b) displays the Crab Nebular as a pulsar wind SNR. The pulsar in the centre is not apparent. Finally, Figure (c) provides a picture of the supernova remnant Kes 75 which is a composite SNR. Here, the low energy range is coloured in red, the high energy range in blue. The bright blue spot in the centre of the image is the pulsar generated during the core collapse.

interstellar medium (ISM), contain mostly hydrogen and helium as well as some traces of other elements summarized as metals. They are heated up by events like supernova explosions or other processes during which particles are accelerated, generating shock fronts. At temperatures above 10^5 K, atoms inside the gas are assumed to be mainly ionized and ions and free electrons are thought to be in thermal equilibrium. The electrons can then generate Bremsstrahlung in the electric fields of the positively charged ions.

Additionally, electrons in the hot gas can excite atoms that are not fully ionized and generate characteristic radiation. Discrete emission lines appear in the continuum of the thermal emission. The intensity of these lines together with the upper edge of the continuous spectrum can be used for the determination of the gas temperature. The higher the temperature, the more atoms are ionized and therefore fewer lines can be found in the continuum (Charles and Seward, 1995).

1.2.8 Galaxies and clusters of Galaxies

Galaxies contain all types of X-ray sources mentioned above. Besides AGNs, some of the most luminous ones are accreting systems, particularly binary systems containing compact objects like white dwarfs, neutron stars or black holes. They are divided into low mass X-ray binaries (LMXB) for companion stars with masses $M \leq 1\mathrm{M}_\odot$ or high mass X-ray binaries (HMXB) for companion stars with $M \geq 5\mathrm{M}_\odot$ (Mineo, 2011). The accretion processes are very similar to the processes described for the CVs. Here as well, X-rays are produced by the conversion of gravitational energy into thermal energy.
Additional thermal X-rays are produced by hot ionised gas that can be found in and around galaxies.

Clusters of galaxies are the largest gravitationally bound structures in the universe. They contain intra-galactic gas with temperatures up to 10^8 K. Hence, they reach the temperature limit for gas bound to any structure. For higher temperatures the kinetic energy would force

the gas particles to escape. X-rays from galaxy clusters are produced mainly by thermal Bremsstrahlung.
In the X-ray spectra of galaxy clusters once more additional characteristic lines can be found. Those lines originate from the disexcitation of ions up to iron. The only known astronomical processes producing heavy elements such as iron are the nuclear fusion processes inside the stars. Therefore, it is widely assumed that this hot gas was ejected from galaxies inside the cluster where it was produced during supernova explosions (Sarazin, 1986).

1.3 X-ray processes

In astronomy, X-radiation describes the part of the electromagnetic spectrum between 100 eV and about one MeV. A typical limit is the pair production threshold. The spectrum can be subdivided into *soft X-rays* for energies between 100 eV and 10 keV and *hard X-rays* for higher energies. There are two classes of processes generating X-rays.

1.3.1 Non-thermal processes

1.3.1.1 Bremsstrahlung

If an electron is strongly accelerated or scattered in an electric field like the field of an high Z nucleus, all or part of its kinetic energy can be emitted as *Bremsstrahlung*. The spectrum of this radiation is a continuum with an upper limit at the kinetic energy of the initial electron. The spectrum of the Bremsstrahlung follows the Kramers Law.

$$I_\nu(E) = \mathrm{K}Z(E_\mathrm{e} - E) \tag{1.3}$$

Here, I_ν is the spectral intensity, E_e is the energy of the electron, K is a constant and Z is the atomic number of the nucleus (Kramers, 1923).

1.3.1.2 Characteristic radiation

During the interaction of a high energetic photon with an atom, the photon can use part of its energy to raise one of the atom's electrons to a higher energy level. When the raised electron falls back into its original state it emits *characteristic radiation*, which is a discrete spectrum unique for the atom of interaction (Demtröder, 2010).

$$\Delta E = E_\mathrm{UpperShell} - E_\mathrm{LowerShell} \tag{1.4}$$

1.3.1.3 Synchrotron radiation

In sources with high magnetic fields, bypassing relativistic electrons can be deflected, producing magnetic Bremsstrahlung or *synchrotron radiation*. Depending on the magnetic field strength, the resulting intensity spectrum is a power law

$$I(E) = \mathrm{A}E^{-\alpha}, \tag{1.5}$$

where A is a constant and α the spectral index. For astrophysical sources the spectrum is independent from the direction of the scattered photon which in that case is assumed to be distributed isotropic.
This process occurs mostly in supernova remnants (SNR) where the magnetic field can reach $7 \cdot 10^5$ G. The energy of electrons in the surroundings of a SNR is about 1 GeV. X-ray pulsars also emit synchrotron radiation (see Charles and Seward, 1995).

1.3.1.4 Inverse Compton scattering

Inverse to the normal Compton effect at which a high energetic photon is scattered at an electron while losing energy, in the surrounding of high energetic electrons low energetic photons can gain energy during the inverse Compton interaction. Both processes are summarised as *Comptonization*. The intensity spectrum also follows a power law.

$$I(E) \propto I(E_i) \left(\frac{E}{E_\mathrm{i}}\right)^{-\alpha} \tag{1.6}$$

It is $I(E_\mathrm{i})$ intensity at the mean photon energy E_i and α the spectral index depending on the optical thickness of the medium and the mean amplification of the photon energy per scattering (Rybicki and Lightman, 2004).
This process can be found in areas where electrons are extremely accelerated like around compact objects or in areas filled with hot gas.

1.3.2 Thermal processes

1.3.2.1 Black-body radiation

Hot objects emit thermal radiation, referred to as black-body radiation. A black body is an idealized object that is a perfect absorber as well as a perfect emitter for every wavelength. The shape of a spectrum emitted by such a black body is a continuum and the intensity is given via

$$I(E,T) = 2E^3[\mathrm{h}^2\mathrm{c}^2(\mathrm{e}^{E/(\mathrm{k}T)} - 1)]^{-1}, \tag{1.7}$$

where h is the Planck constant and c the speed of light (Charles and Seward, 1995).
For sources with temperatures of about $10^6\,\mathrm{K}$ to $10^8\,\mathrm{K}$, the black-body radiation can enter the X-ray energy range. Wien's displacement law describes the displacement of the peak energy of a thermal spectrum and can be calculated as the maximum value of the Planck spectrum (Planck, 1901).

$$E = \frac{8\pi\mathrm{hc}}{\lambda^5} \frac{1}{\mathrm{e}^{\frac{\mathrm{hc}}{\mathrm{k}\lambda T}} - 1} \tag{1.8}$$

$$\Rightarrow \lambda_\mathrm{max} = \frac{\mathrm{b}}{T} \tag{1.9}$$

where λ is the wave-length and $\mathrm{b} = 2.8977721(26) \cdot 10^{-3}\,\mathrm{mK}$ the Wien displacement constant (Particle Data Group, 2014). Depending on the notation, in Equation 1.7 it is possible to choose between the intensity per unit of frequency or per unit of wave-length by inserting $E = \mathrm{h}\nu$ or $E = \frac{\mathrm{hc}}{\lambda}$. Nevertheless, the Stefan-Boltzmann law requires equality for the total flux in both cases.

$$\int_0^\infty I\nu(\nu,T)\mathrm{d}\nu = \int_0^\infty I_\lambda(\lambda,T)\mathrm{d}\lambda \tag{1.10}$$

Thus, there is no longer a linear correlation between λ_max and ν_max. Instead it is

$$\nu_\mathrm{max} \approx 0.568 \frac{c}{\lambda_\mathrm{max}} \tag{1.11}$$

The maximal energy is then found as

$$E_\mathrm{max} = \mathrm{h}\nu_\mathrm{max} \approx 0.244 \left[\frac{\mathrm{keV}}{10^6\mathrm{K}}\right] T \tag{1.12}$$

Those hot objects can be stars, black holes, neutron stars or white dwarfs, as well as AGNs.

1.3.2.2 Thermal Bremsstrahlung

By adding the energy spectrum of Maxwell distributed electrons to the continuous spectrum of the Bremsstrahlung, the typical spectrum of hot gaseous sources can be found for which the intensity is given as

$$I(E,T) = \mathrm{A}\, G(E,T) Z^2 n_\mathrm{e} n_\mathrm{i}\, (\mathrm{k}T)^{-1/2}\, \mathrm{e}^{-E/(\mathrm{k}T)}. \tag{1.13}$$

Hereby, A is a constant, Z is the charge of the ions, n_e and n_i are the densities of the electrons or the ions in the gas, whereas k is the Boltzmann factor. The function $G(E,T)$ is the so called *Gaunt factor*, which is a correction factor that provides quantum mechanical corrections to classical calculations and which increases for decreasing energy (Charles and Seward, 1995).

1.4 Detection of X-rays

The selection of the appropriate telescope optics and detectors are a key factor for all astronomical missions. Every energy range requires its own techniques. Selected optics and detectors for the X-ray range will be described in the following section.

1.4.1 Wolter Optics

In order to detect X-rays from astronomical sources, special telescope optics are needed. In addition to collimators, coded-masks and rotation modulation collimators that limit the field of view, focusing optics are used for X-ray imaging. In general, focusing X-ray optics are constructed via curved reflecting surfaces. For the reflectivity of a material, an important factor is the refraction index. This index n is greater than one for optical photons scattered at a surface transition from vacuum to matter, but decreases for larger wavelengths. Therefore, the commonly used way of focusing X-rays is by total reflection due to grazing photon incidence. The critical incidence angle for total reflection can be calculated by Snell's law and is approximately

$$\alpha_\mathrm{t} = 5.6\lambda\sqrt{\rho} \tag{1.14}$$

for high Z elements. Hereby, λ is the wavelength of the incident light and ρ is the density of the mirror material.
In 1952 Hans Wolter proposed three types of X-ray telescope geometries from which the so called *Wolter I* is the one used mainly in X-ray astronomy, see Figure 1.3.
Wolter I telescopes consist of a combination of a paraboloid and a hyperboloid surface with a common focus (Wolter, 1952). This construction allows a reduction of aberration effects. Nowadays mostly iridium, platinum and gold are used as materials for the mirrors. In order to maximise the collecting area of the telescope, multiple mirrors are nested (Aschenbach, 2009).

1.4.2 Detectors

In X-ray astronomy two different kinds of detectors are used. Especially in the early X-ray missions, radiation was detected by proportional counters and later on by scintillation counters. These non-imaging instruments are capable of detecting the amount of photons

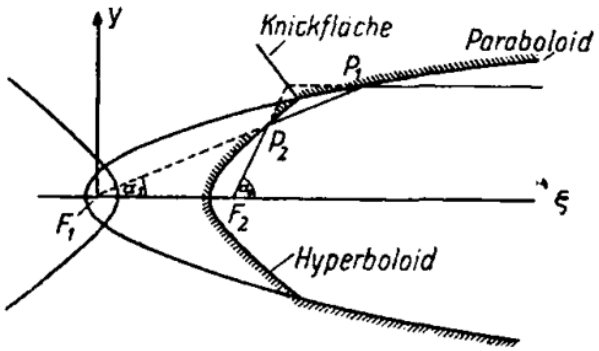

Figure 1.3 Wolter I mirrors consist of a combination of a paraboliod and an hyperboloid surface. Light reflected at the bending area (*Knickfläche*), is collected inside the common focus F2. Image from Wolter (1952).

coming from a source without any spatial information. For the limitation of the field of view, collimators were used.
Later detectors with higher spatial and spectral resolution were constructed. Those are, for example, the charged coupled devices (CCDs). The different detectors are further described in this section.

1.4.2.1 Proportional counter

Proportional counters operate on the same principle as Geiger counters: A capacitor is set inside a gas-filled tube with an high electric field between the two electrodes. Incident X-ray photons are absorbed in the gas via while producing free electrons by ionisation. Those electrons are accelerated inside the electric field of the capacitor. While they drift toward the anode, they can ionize further atoms of the gas and in this way amplify the charge that reaches the electrodes. The current I of those charges that is measured at the electrodes of the capacitor is proportional to the initial number of incident photons. The amplification factor can have values up to 10^6 depending on the applied voltage (Demtröder, 2010).

1.4.2.2 Scintillation counter

Proportional counters can be used for the detection of X-rays with energies below 20 keV. Higher energetic photons cannot be stopped inside the gas filled tube. Instead, solid detectors are needed in order to detect those photons. Scintillation counters are therefore used. Those detectors are made of a certain scintillation material that can be excited by the incident ionising X-rays and then emits fluorescence light. For the material selection, it is important to ensure that photons hitting the detector at a high rate can be detected separately. The time the detector needs to handle one photon and in which he is not able to detect a new photon is called the *dead time* of the detector.
The detector materials can be divided into organic and non-organic materials. Non-organic scintillators have a higher yield of light than the organic ones. They are semiconductor or isolating materials, doped with activators with smaller ionisation energies than the original crystal structure. Examples for those detector materials are sodium iodide (NaI) or caesium iodide (CsI) doped with thallium (Tl) or sodium (Na), respectively.
If an X-ray photon hits the detector, the energy is high enough to raise an electron from the valence band to the conduction band, creating an electron-hole pair. The holes can now ionise

the activators whose ionisation state lies inside the energy gap of the crystal. The electrons that were raised to the valence band can recombine at those activators (typical time scales are 50 to 1000 ns) and emit their energy as lower energetic fluorescence light. If this light is in the visible range it can leave the detector without recreating new electron-hole pairs. The process is shown in Figure 1.4.

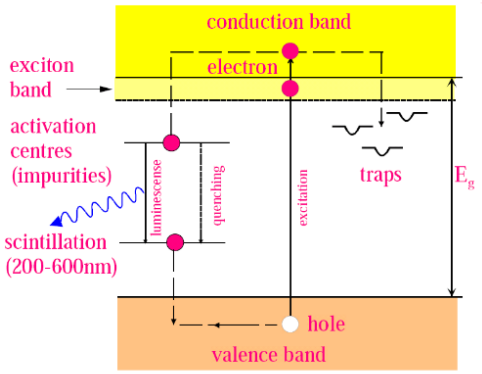

Figure 1.4 Principle of a scintillation counter. An incident X-ray photon generates an electron-hole pair whereby the electron is raised to the conduction band while the hole ionises an activator ion with an energy level inside the energy gap of the original crystalline structure. When the raised electron de-excitates trough the energy states of the activator, it emits low energetic light that is able to leave the detector material. Image by Christian Joram (CERN).

Beside the requested fast fluorescence de-excitation, phosphorisation can also be found inside the scintillation detectors. If an electron is raised into an energy level from which it is not allowed to fall back to the energy ground level, it has to be raised up even higher by collision ionisation with other electrons, to energy levels from which it can once more enter the ground level. This process can limit the accuracy of the detector because the duration is significantly longer than the fluorescence process and multiple photons cannot be distinguished.

The signal from the low energetic photon leaving the detector material can be amplified by a photomultiplier tube. Hereby, the photon collides with a cathode generating an electron due to the photoelectric effect. This electron will itself collide with further electrodes, creating a shower of secondary electrons proportional to the initial photon signal. The process is amplified by applying high voltage to the tube. This way the electrons are further accelerated producing even more secondary electrons. If n is the number of electrodes inside the photomultiplier, the amplification is

$$N_{\text{signal}} = N_{\text{primary}} \mathrm{Q}^n, \tag{1.15}$$

where N is the number of particles and Q the amplification factor typically between 6 and 8. In this way, amplifications up to 10^8 are possible (Birks, 1967).

1.4.2.3 Charge coupled devices

Charged coupled devices (CCDs) were initially constructed as data storage devices, but were soon noticed to be usable as detectors for light of different energy ranges.

There are several kinds of CCDs. The concept of a CCD used for instance for the eROSITA mission is based on a p-n-junction of semiconductors. For typical pnCCDs, silicon crystal

structures are doped with elements that have at least one more valence electron for the n-type layer and with elements that have fewer valence electrons for the p-type layer. If those two layers are brought together, electrons recombine with the holes in the p-layer structure. An electrical field is applied between the two layers to enlarge the recombination zone. This zone contains no more free charge carriers and is called depleted.
If high energetic photons enter the depleted zone, they create electron-hole pairs. Those pairs are separated in the electric field since the holes drifts to the n-layer while electrons travel in the direction of the p-layer where they can be stored in potential wells.

For X-rays this effect is further enhanced. In this case two p-layers are used, enclosing one n-layer. A voltage of about 200 V is applied to one p-layer whereas a much smaller voltage of about 20 V is applied to the other so that in the end the whole layer in between is fully depleted and sensitive to the X-rays. This process was described by Gatti and Rehak (1983) and is known as *sideward depletion*. In Figure 1.5 the principle is illustrated.

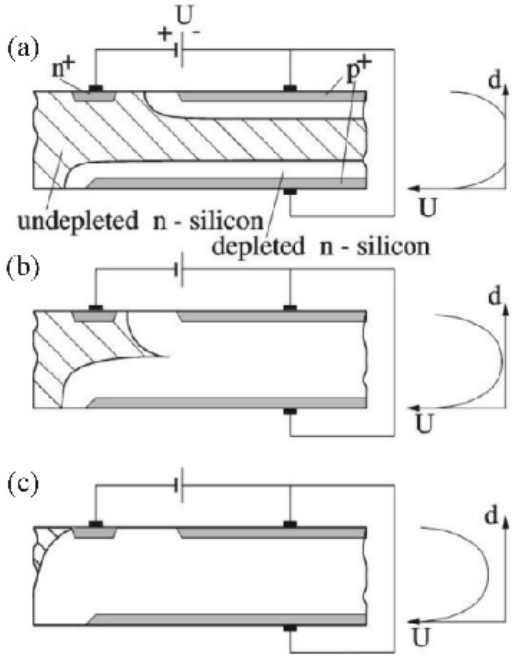

Figure 1.5 Principle of the sideward depletion of a pn-CCD according to Gatti and Rehak (1983). In Figure (a) no voltage is applied to the pn-junction, so only the basic deplation zone has formed. From (b) to (c) the voltage is increased until the zone is fully depleted. Image taken from (Send, 2013)

For astronomical detectors, large arrays of those pnCCD sensors are used. This way an image can be generated that provides spatial information about the incident photons.

An image of such a CCD is shown in Figure 1.6. The pixel array is illuminated as a whole, but read out row by row. For this, the charge of collected in each row has to be converted into a voltage. However, only one edge of the CCD is connected to the charge-voltage converter. This row can be read-out. All other rows has to be shifted to the read-out, step-by-step. This is done by controlling the voltage Φ applied to the individual electrodes. When the charge in the row at the read-out electronics is converted into a measurable voltage signal, the row is empty from charges. To this row a voltage is then applied which is the same as the voltage in the next higher row, so that the stored electrons are spread over the whole area of both

rows. Then, the voltage in the upper row is raised in order to force all remaining electrons to move to the readout row. There they can again be processed by the charge-voltage converter. This way all rows can be read out one by one (Boyle and Smith, 1970).

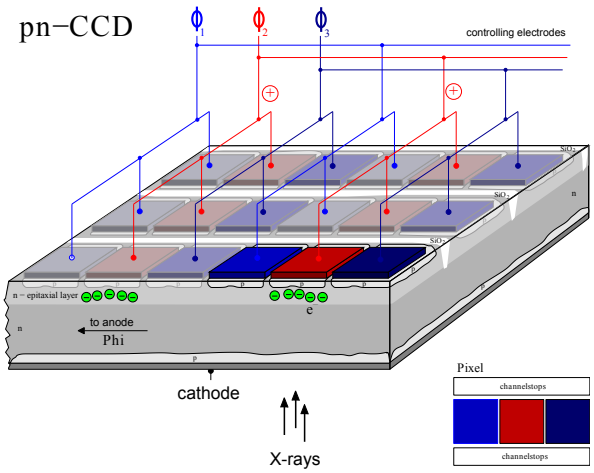

Figure 1.6 Functionality of a pnCCD. Incident X-rays induce charges that are collected in potential wells. Due to the controlling of the voltage applied to the electrodes, the charge can be shifted to the read out converters. Image by Thomas Schanz (IAAT).

1.5 Significance of X-ray background for space missions

For all space missions, a large amount of engineering work is required from the first sketches to material testing and actual construction. With the advent of modern computers, instrumental geometries and material configurations can be tested by simulations during the early phases of a mission. In this way, the influence of the setup that envelops the sensitive part of the detector can be studied and errors in the construction and the amount of spent resources can be reduced. Today, simulations of physical processes and instrumental functionality are a basic component of all fields of physics.

A main part of these pre-mission simulations are studies about the background that is expected for a certain detector. For X-ray missions, this background contains on the one hand photons from the *cosmic X-ray background* (CXB), on the other hand soft protons coming from strong solar winds, cosmic rays, stray light or solar wind charge exchange.
The CXB was already detected in 1962 during the first rocket-aided X-ray mission by Giacconi et al. (1968). For a long time it was assumed to be a kind of hot gas, maybe even generated shortly after the Big Bang like the cosmic microwave background (CMB). Today it is believed that the CXB consists of the radiation from many unresolved X-ray sources, mainly AGNs for the background in the energy range between 3-300 keV, supernovae type Ia for the energy range between 300 keV and 30 MeV as well as blazars for even higher energies (Gruber et al., 1999).
The background depends strongly on the orbit of the mission's satellite. Key factors are the distance from the Sun for the strength and amount of the soft protons as well as the proximity to the Earth for shielding effects by Earth's atmosphere and magnetosphere. The inclination of the orbit to the rotation axes of the Earth is also important. The *South Atlantic Anomaly* (SAA) 200 km above the surface of the Earth and near Brazil in terms of degree of longitude and latitude origin from the tilt of the magnetic to the rotation axis. High energetic solar

wind particles are trapped within and cause an additional background for spacecrafts crossing the region.
A sample spectrum for soft protons and the CXB calculated for the planned orbit of the IXO[4] mission that was scheduled for 2020 is given in Chapter 7.

This background can induce additional intrinsic background inside a detector geometry in addition to the electronic noise. Minimum ionising particles depose high amounts of energy inside the detector. Those events can be excluded easily by setting a certain high energy threshold that is significantly exceeded by the deposition.
One way to reduce this background is by excluding the pixels that exceed the energy threshold as well as all neighbouring pixels. The method is called *MIP rejection*.

Other charged particles with energies which are within the correct energy range cannot always be distinguished from real events. However, especially high energetic particles who deposit energy in one pixel of a detector deposit further energy in neighbouring pixel creating a path through the detector. By pattern analysis only those events can be counted in which only certain valid pattern of pixel are hit by a photon.

A dominating background source inside a detector are fluorescence effects induced by cosmic rays. If those highly energetic particles collide with the outer materials of the detector like shieldings or blinds, they can raise electrons to higher energy levels. When these electrons fall back to their basic state, they emit photons in the X-ray energy band. Those emissions are mostly K-shell de-excitations producing characteristic lines inside the background spectrum. This effect can be reduced by installing a *graded Z shield*. Several layers of materials with different atomic number Z are set around the detector leaving only the entrance window open for incident radiation. It is important that the atomic number increases the further away the layer is from the detector itself. Cosmic rays then depose energy in the layer furthest from the detector which generates high energetic fluorescence photons. Those photos are absorbed in the next layer producing again fluorescence photons, but with lower energy than before until in the lowest layer the energy is low enough to fall below the low energy threshold of the detector. Thus, for the lowest layer mostly materials like boron or carbon compounds are used because their K-shell de-excitations are at very low energies (Katayama et al., 2004).

Another limiting effect for the operation of a detector was observed quite recently, during the XMM-Newton mission. In one orbit 35 pixels showed a sudden unexpected increased count rate that was later assumed to be caused by micrometeroids. Those compact grain or dust particles can enter the Wolter optics where they are scattered and disintegrate in the process. The damage induced by those secondary particles is not negligible.
At the *Max-Planck Institut für Kernphysik* in Heidelberg, Germany many properties of impacting grain and dust particles can be analysed such as the intensity and the traces of the impact left on the CCD surface as well as the effects done to an operating CCD. For the measurements a particle accelerator is used. Studies done by Pfeffermann et al. (2004) match the effects found during the XMM-Newton measurement. To reduce the danger of damage by micrometeroids an appropriate shielding is necessary.

In this work computer-based Monte-Carlo simulations of particle background and detector functionalities are performed for several astrophysical X-ray space mission geometries. Important properties like quantum efficiency or shielding capacities are analysed. The effects of micrometeroids are not further investigated because it cannot be simulated by the simulation toolkit used for this work.

[4]IXO: International X-ray Observatory

In Chapter 2, the idea behind the Monte-Carlo method will be presented shortly together with the description of the Geant4 software that is used for the implementation.
Because there are several versions of the Geant4 code, that are used during this work, in Chapter 3 the comparability of those version is tested in a simple simulation environment. The energy loss processes of electrons in matter are therefore simulated with four different Geant4 versions.
The following chapters approach the actual simulation projects. The projects are not only related to different space missions but also cover simulations in various energy ranges. In Chapter 4 a low keV range was treated for a quantum efficiency measurement for eROSITA. This simulation was performed in order to compare simulated data to a laboratory measurement done by Ebermayer et al. (2010).
The study of a Compton telescope setup for a high keV range is reported in Chapter 5. An analysis tool is provided to reconstruct X-ray images observed with a Compton telescope. Beside a simple two layer setup, the effects of a three layer setup are studied.
In Chapter 6, the results found in the previous chapter are used for the simulation of the CANDELA stacked detector setup by Maier (2014) used for the work on SIMBOL-X detectors that can also be used as a Compton telescope. The main focus is on the analysis of the fluorescence background.
In Chapter 7, shielding configurations for a graded-Z shielding are simulated for the recently selected Athena mission. The effects of the CXB as well as the effect of protons on the detector geometry are analysed.

The individual chapters for the projects are roughly divided into four parts each: a theoretical part including all the physics needed for the understanding of the used processes, a description of the simulated setup as well as a part about the evaluation of the received data followed by a discussion of the results.

In Chapter 8, a short summary of the results can be found as well as an outlook will be presented about what other measurements or simulations could be run in order to continue the work conducted in this thesis.

In the appendix, which contains additional material, more detailed derivations of parameters or data tables are provided. Manuals for Geant4 and the self-written software are also attached.

2 The Geant4 tooklit

The simulations presented in this work were performed with the help of the simulation toolkit Geant4. The toolkit uses Monte-Carlo methods in order to simulate interactions between particles and matter in a given detector geometry. In the beginning of this chapter the Monte-Carlo method will be introduced focusing on the historical development as well as on the basic ideas of the theory behind the method. In a second part, the simulation tool Geant4 itself will be presented, also outlining the historical progress, the general handling and the structure of the tool.
Because Geant4 is an open source project, in the Appendix 1 a manual is provided about the installation of the source code of version Geant4.9.6 that was mainly used during this work. An introduction on how to execute simple simulation examples is also given there.

2.1 Introduction to the Monte-Carlo method

Monte Carlo is a numerical method that uses probabilities to establish statements about the behaviour of a system. In this way, through frequent iterations of solving a problem in a random configuration by calculating mean values, the global observables of the system can be obtained. The method was already used in the 18th century under the name of *statistical sampling* but became popular when the first electronic computers were introduced because of the huge number of calculations which have to be done in order to reach the desired accuracy. The Buffon Needle Problem from 1733 was one of the first Monte Carlo simulations done long before the time of electronic computers. George-Louis Leclerc, Compte de Buffon (Figure 2.1(a)), calculated the value of π by measuring the probability of dropped needles to cut the lines between the boards on the floor. With this approach by dropping only 10 needles already values for π of about 3 can be obtained (Dunn and Shultis, 2011).
The idea behind this measurement is the following: the floor with the boards represents a plane with parallel lines in a certain distance D to each other. This distance should be larger than the length of the needles. Then, the probability of a needle that dropped on the plane under an angle of ϑ to cut such a parallel line is

$$P_{\text{cut}}(\vartheta) = \frac{L \sin(\vartheta)}{D} \tag{2.1}$$

which is the parallel projection of the needles length divided through the distance between the lines. Figure 2.1(b) shows a geometrical display of the problem.
Furthermore, the possibility to find the needle under an angle ϑ is

$$P(\vartheta) = \frac{1}{\pi} \tag{2.2}$$

for symmetry reasons. As a result, the total probability of a needle to cut a line is

$$P_{\text{cut}} = \int_0^{\pi} \frac{L \sin \vartheta}{D\pi} \mathrm{d}\vartheta = \frac{2L}{D\pi}. \tag{2.3}$$

This probability can be obtained by performing the drop many times and thereby the value π is obtained. The larger the number N of dropped needles the higher the accuracy of π.

In 1945 the United States started a secret project at the Los Alamos Scientific Laboratory to study the movements of neutrons for the development of the first hydrogen bomb. For this task, the Electronic Numerical Integrator And Computer (ENIAC, see Figure 2.2(a)) was used, which was the first fully electronic computer. Leading scientists of this project were Nicolas Metropolis, Stanislav Ulam and John v. Neumann who gave the statistical sampling method the code name *Monte-Carlo* because the seemingly gambling nature of the method reminded them of an uncle of Ulam who was known to "borrow money from relatives because he just had to go to Monte Carlo" (Metropolis, 1987). While the code was written to implement the method for the ENIAC and the ENIAC itself was moved to the Ballistics Research Laboratory in Maryland, Enrico Fermi, also interested in the diffusion processes of neutrons, constructed an analogue mechanical device, the FERMIAC (Figure 2.2(b)), in order to do the same calculations as done in Los Alamos.

The Monte Carlo method works for all physical systems that can be described by their probability density. To solve the problem, for the included variables, a set of values is chosen depending on the probability density and the system is solved in this configuration. This process is repeated several times for randomly chosen sets of values. If N, the number of iterations, is large enough, from constructing mean values, statements regarding the general behaviour of the whole system can be derived.
As an example the numerical solution of a one-dimensional integral can be calculated. The mean value of a system depending on one variable x can be written as an integral over the whole function folded with the probability density of the variables.

$$< z >= \int_a^b z(x) f(x)\,\mathrm{d}x \tag{2.4}$$

Here, $z(x)$ is the function describing the system and $f(x)\,\mathrm{d}x$ is the probability density of the values x. Even if the function is assumed to be already too complicated to be solved analytically, the Monte Carlo method can be applied. On that account, N values of x are chosen randomly depending only on their probability density. The function is then evaluated at this N so called nodes x_i and the integral is solved as a Riemann sum.

$$\bar{z} = \frac{1}{N} \sum_1^N z(x_i) \tag{2.5}$$

The error of this method goes with $N^{-1/2}$ even in higher dimensional problems. This way, with a large enough sample size N, very high accuracies can be obtained (Dunn and Shultis, 2011).
For the physical processes later treated for particle interactions, the probability densities are the corresponding cross section.

In some cases it is not even necessary to formulate the problem which should be solved in a mathematical way. Dunn and Shultis (2011) allege an example in which the area of a continent drawn on a map should be figured out. For this purpose, points on the map are randomly chosen. By counting the number of chosen points found inside the continent and the number of those outside, the percentage of the continent area on the whole map area is obtained. No mathematical description is needed, so the result is independent of a specific model.

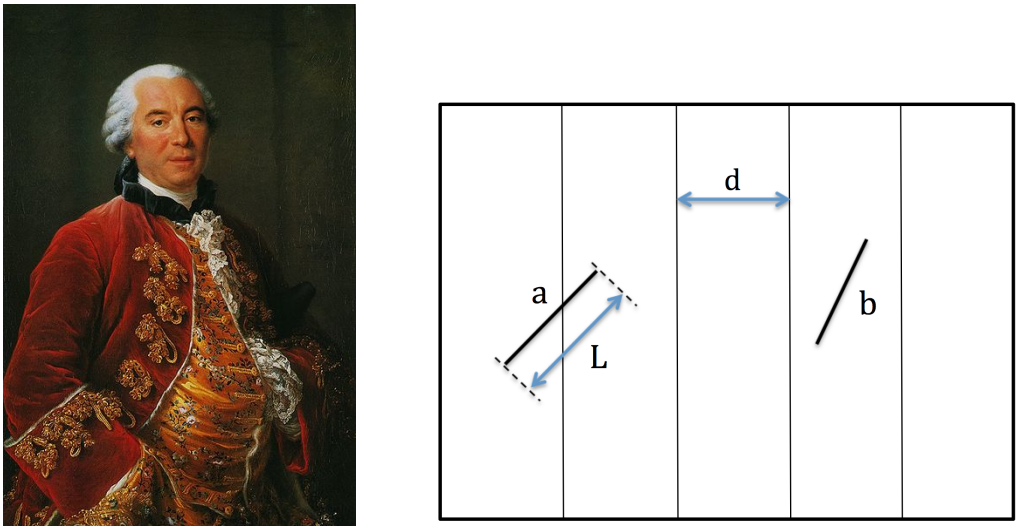

(a) (b)

Figure 2.1 George-Louis Leclerc, Comte de Buffon (a) calculated the value of π with the Monte Carlo method (Portrait by François-Hubert Drouais (1753)). From Figure (b) the probability of a needle with the lenght L dropped under a certain angle to cut one of the parallel lines in a distance d can be calculated (Image taken from from `http://andreiformiga.com`)

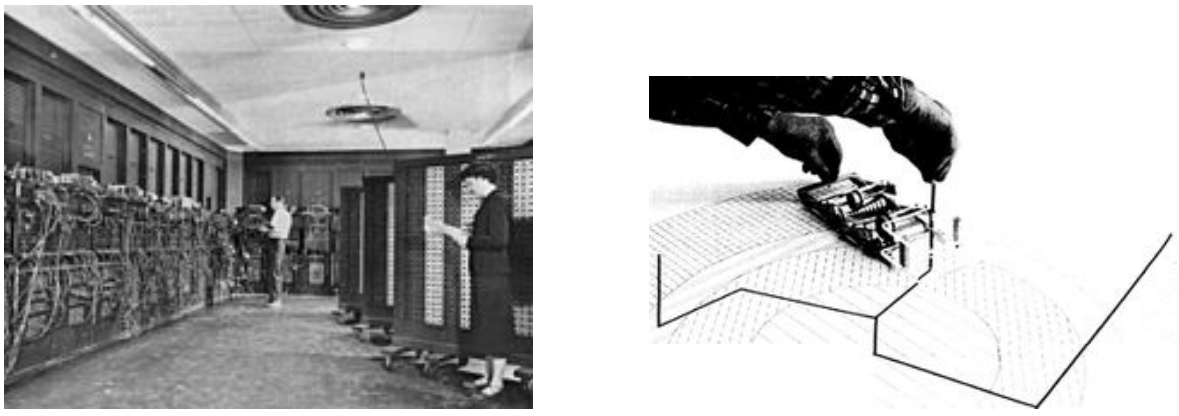

(a) ENIAC (b) Fermiac

Figure 2.2 Devices for performing Monte Carlo calculations. (a) shows the electronic devices used at the research laboratory in Los Alamos (US Army Photo). The two women in the picture are Betty Snyder (front) and Glen Beck (background), two female programmers at Los Alamos. (b) shows the mechanical device built by E. Fermi doing the same calculations (Image taken from Metropolis (1987)).

2.2 Introduction to Geant4

Geant4 is a tool-kit to simulate interactions between particles and matter from the generation of a particle in a source until all its energy is used up on the way through a given geometry or until it has left the described geometry (Agostinelliae et al., 2003). At the beginning Geant was an acronym for Generating and Tracking. Later as geometries got more and more important it became an acronym for Geometry and Tracking. It is nowadays used in almost all areas of physics like space science, nuclear medicine or accelerator projects like CERN[1].
The code itself is based on a former project, Geant3, written by Rene Brun in the 1970s in the computer language Fortran. In 1993 two groups, one at CERN and one at the Japanese accelerator project KEK[2], decided to refine the code to match the growing complexity of the project. It was therefore rewritten in C++ and is thus object-oriented which leads to a higher flexibility of the code. One year later the two groups joined forces under the lead of the CERN group as a research and development project called RD44. The first production release was in 1998. At the beginning of the year 1999 the GEANT4 collaboration was founded in order to coordinate further development, implementation of new physical processes and user support under the demand of openness, modularity, transparency and flexibility (Geant4 collaboration, 2013). Today projects like ATLAS[3] (CERN), XMM-Newton (ESA) or the Fermi Gamma-ray space telescope (FGST) use Geant4 simulations to compare the results to their experimental data or to do material and geometry tests before building new components (ESA, 2014).

2.2.1 Structure of the Geant4 simulation tool

The Geant4 code is object oriented which means it is based on interfaces and classes for every component of the simulation (geometry, particles, events etc.). This provides a high level of flexibility. Each physical process is implemented as an interface containing the corresponding cross-sections for each particle from calculations as well as from experimental data as far as they can be obtained. The user can select only those processes that are of interest. Also, for new theories, interfaces can be written with the cross-sections from theoretical calculations or measurements to test them against each other.
In Figure 2.3 the class diagram of the Geant4 source code is shown to give an overview over the main structure of a Geant4 simulation. Following a hierarchical concept, classes beneath are required by the classes above. From bottom to top, the lowest unit is the **global** class. It contains all kinds of mathematical basics needed to do the Monte Carlo calculations. The most important ones are the physical and mathematical constants, a system of units and methods to generate random numbers.
The next unit is the class for **material** definitions. In order to calculate the proper interactions between the particles and the detector geometry, the material of each detector part has to be specified. Those materials can be chosen predefined for example from the NIST[4] database or can be constructed by the user himself. Hereby, physical properties like atomic numbers, density, aggregation state or temperature of the materials can be used for the description.
In the next step **particles** can be chosen. There is one class for every kind of particle, so that the user can select single particles or whole particle families like fermions, bosons or

[1] CERN: Centre Européenne pour la Recherche Nucléaire
[2] KEK: kō-enerugī kasokuki kenkyū kikū: High energy accelerator research facility
[3] ATLAS: A Toroidal LHC ApparatuS
[4] NIST: National Institute for Standards and Technology

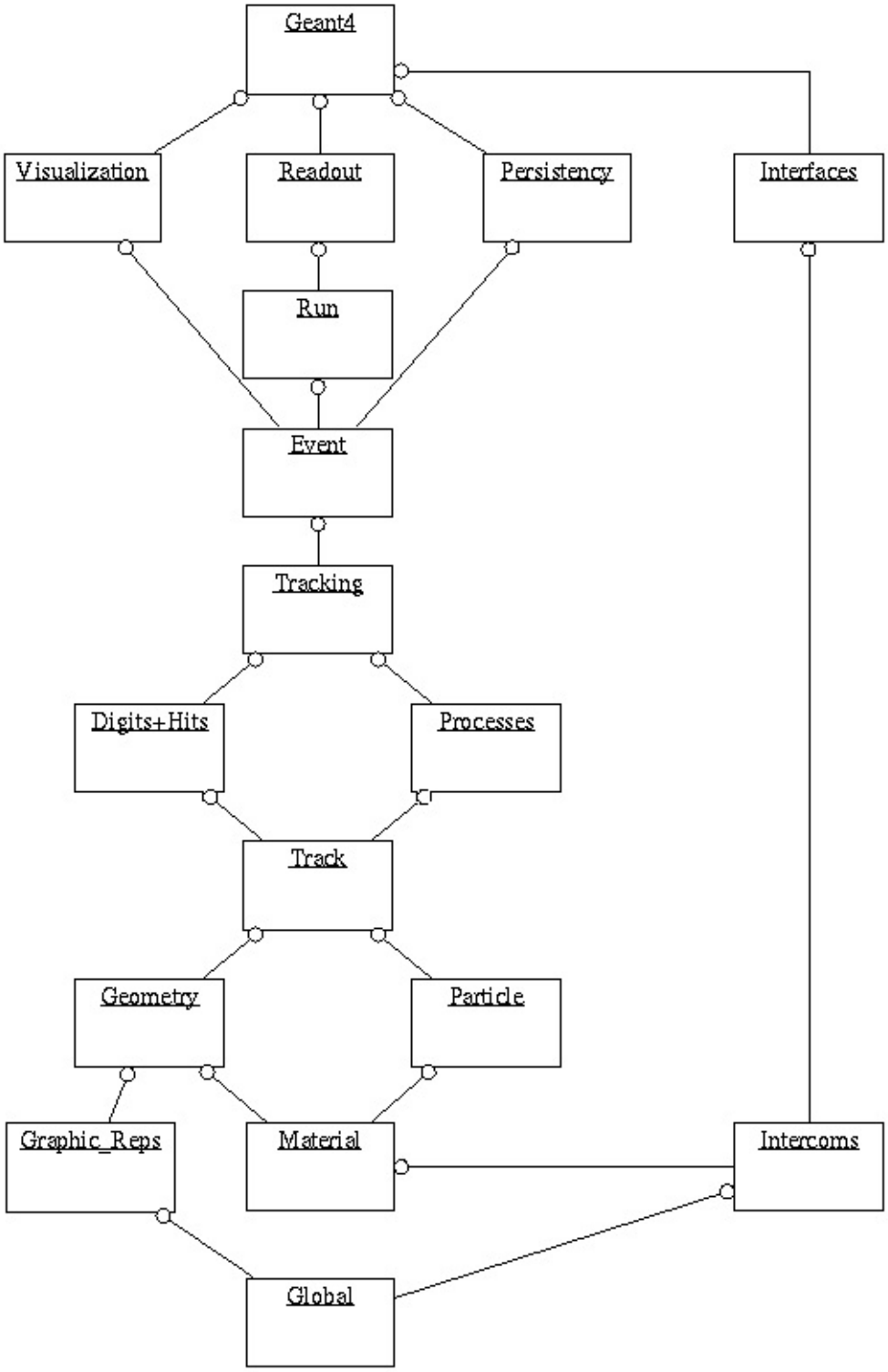

Figure 2.3 Class diagram for the basic structure of the Geant4 code (Geant4 collaboration, 2013). Here, the lines between the classes can be understood as arrows indicating the hierarchy. Regarding two classes, the one at the head of the arrow (white circle) needs the other one in order to work.

quarks. It is important to note that not only the primary particles have to be selected but also all particles that could be produced as secondary particles during an included process. However, the more particle types are accounted for, the longer the simulation time.
In the **geometry** class, functions for describing the geometry of the given problem are included like simple geometrical figures as well as methods to combine them. The class is connected to the material class in order to give specific material characterization to the different parts of the setup.

All the classes described so far are needed to set the environment in which the simulation takes place. The next step is then to calculate the path of the particle through the geometry. For that task, the simulation is divided in three units. The smallest of those units is a *step* which describes the movement of a particle from one randomly chosen process to the next. It is coordinated by the **track** class.
The length of the step depends on the chosen process that is taken from the **processes** class which contains all the cross sections of the processes. For every particle chosen for the simulation, the requested processes have to be registered. A new process is chosen after a particle has travelled a certain step length that depends on the process or when it would cross a material border of the geometry.
The class **tracking** is overseeing the tracks of the particle in the steps and coordinates the **hits** class by checking if the particle for instance loses energy in a sensitive part of a detector. Then the track is classified as a hit.
All these activities are sampled in the next higher unit of the simulation after the *step* which is an **event**. An event contains all information about the path of one primary particle from its generation to its vanishing either due to the total loss of kinetic energy or to leaving the considered setup including all movements of secondary particles generated during the lifetime of the particle. Here, *total loss of kinetic energy* means that the kinetic energy of a particle falls below a certain threshold defined by the user.
The highest unit of the simulation is the **run**, which contains the events for all particles in one simulation. Classes above are for visualisation and other kinds of data readout.

The user can use all these classes in order to get the requested information from the simulation. For this purpose, these classes can be combined into so-called *user classes* with different complexity depending on the given problem. Every simulation requires at least three user written classes: The detector geometry class, the physics list class and the primary generator action class. These three classes as well as some minor ones for data handling are described in the following paragraphs in more details.

2.2.2 Using the Geant4 code

2.2.2.1 Detector geometry

The most important part of a Geant4 simulation is the definition of the detector geometry. It consists of at least two parts: the detector itself and the surrounding world volume as the environment in which the experiment is supposed to take place and which determines the borders for the propagating particles. Every component of the detector geometry is then again constructed from three kinds of volumes: a solid volume (for physical dimensions), a logical volume (for material characterizations) and a physical volume (for the position inside the world volume).
In the **Solid Volume** the detector components are constructed from basic solid figures like boxes, tubes or spheres (see Figure 2.4). The most common ones are predefined and the user

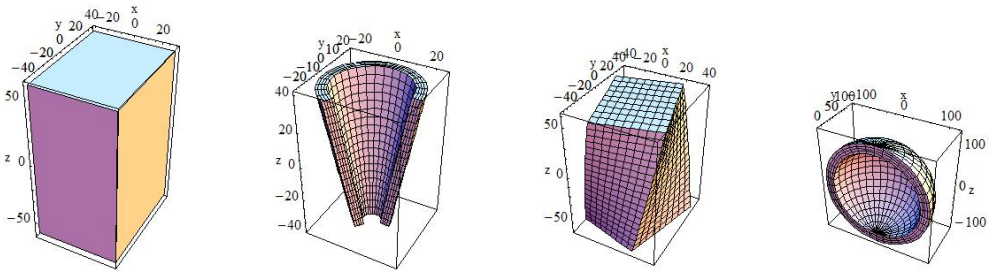

Figure 2.4 The solid volumes in the detector geometry can be build up by using simple geometrical volumes like boxes, cones or spheres. Also some more complex volumes are predefined in Geant4 (Geant4 collaboration, 2013).

has only to specify the size of the object. These solids can then also be combined to more complex structures by simple boolean commands like subtracting, unifying or intersecting the volumes.

Further possibilities are the definition of the volumes by their boundaries (BREP[5]) or the implementation of CAD[6] constructed geometries. Nevertheless, CAD geometries do not always work well in the current state of Geant4. A range of other functions from which the detector can be built up can be found in a detailed description in Chapter 4 of the Geant4 documentation (Geant4 collaboration, 2013).

The **Logical Volume** adds material attributes to the simple geometrical structure of the Solid Volume. Therefore, materials can be taken from predefined data bases or specified by the user himself. Thus, elements, isotopes or complex compositions of materials like stainless steel can be generated. In order to do this, properties like atomic numbers, mass fractions or densities are used. For the material characterisation it is important that the previously described solids are constructed in a way that they can be separated in parts with an unique material definition. They can not overlap in order to avoid boundary conflicts.

Finally, the **Physical Volume** describes the position of the components inside the world volume or another volume. The containing volume is called *mother volume*, the contained one *daughter volume*. The largest volume possible is the world volume that contains all other volumes of the geometry and is itself not contained by another volume.

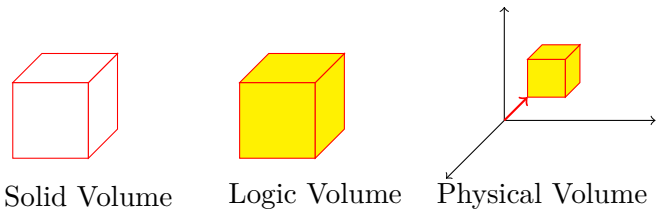

Figure 2.5 To describe the parts of a detector as well as its surroundings in Geant4 three kinds of volumes are needed: a solid volume for the dimensions of a geometry unit, a logical volume for its material characterization as well as a physical volume for the positioning of the unit inside the world volume in which the experiment takes place.

[5]BREP: Boundary Represented Solids
[6]CAD: Computer Aided Design

2.2.2.2 Physics list

Besides the detector geometry, for every simulation the kind of appearing particles and the interactions taking place must be decided on. This can be done in the **Physics List**. As said before, Geant4 uses theoretical calculations as well as provided experimental data sets to describe the physical processes. In this way, also new theories can be tested in the simulation by implementing interfaces of the new processes including the corresponding cross sections.
Every particle as well as every interaction has its own class definition. Single particles like electrons, protons or photons can be studied as well as the behaviour of whole particle families like fermions, bosons or quarks. In principle, all particles could be included at the same time, but this strongly affects the time needed to run the simulation, which will be extended if the simulation becomes more complex. It is therefore useful to decide on the particles that should actually be studied early. It is important to remember that not only initial particles have to be chosen but also secondary particles that would be generated during the simulation.
After choosing the desired particles, the processes that should be studied have to be decided on. Electromagnetic, hadronic or optical photon interactions like scintillation or Cherenkov radiation can be chosen as well as decay and simple transportation. For each particle type all desired processes that apply to it have to be registered. Depending on the process and the studied energy range it is often possible to choose from a number of different implementations. Again, it is necessary to concentrate on the processes that are important to receive the desired results in order to keep down the simulation time. Included in examples provided in the Geant4 tool, there are many complete physics lists generated for specific problems that can be used for own simulations.

2.2.2.3 Primary generator action

The origin of the particles is defined in the **Primary Generator Action** class. In general there are two possible ways of implementation. The first is the *particle gun*. It creates a beam of particles chosen by the user with a determined energy and direction from a certain point inside the world volume. The parameters and values can be fixed or generated randomly for every event. The particle gun is mainly used if the source of the particles in a simulation is not of great significance.
A more flexible way of simulating a source is the *general particle source* (GPS) module. By using this interface, the source in a simulated setup can be characterised as close to a real experiment as possible. As for the particle gun, the origin of the particle can be generated as a point source but also as a two or three-dimensional surface like a disk, a sphere or a box surrounding the detector geometry. For the angular distribution beside a directed beam, the user can choose for instance an isotropic distribution or a distribution following a mathematical function such as sine or cosine. Also, the energy distribution can be varied. The possibilities reach from a mono-energetic spectrum via linear or exponential distributions to a power law or a Gaussian distribution. Additionally, more complex distributions such as black-body, Bremsstrahlung or cosmic diffuse gamma ray distributions are predefined. For decay spectra further options to read in user-defined histograms from which the energy is chosen randomly depending on the given intensities are available.
Another advantage of the GPS is that it can be controlled interactively during the run, so the code does not need to be recompiled if for instance another kind of particle or a different energy range should be tested. As a consequence, the general particle source is very customizable and therefore a tool to handle more complex particle sources easily.

2.2.2.4 Stepping, Event and Run Action

With the classes defined up to now a simulation can be run. However, to get a handling on the data produced during the simulation there are more classes needed, which are called *action classes*.

With the **Stepping Action**, the user has direct access to all observables describing the simulated system. In every step properties such as time stamp, position, energy, process taking place etc. can be called. This way for instance energy loss can be calculated every time the position of a particle is found to be inside a sensitive detector volume depending on the process the particle follows inside.
The stored observables from the single steps can then be handed to the **Event Action** class. An event as mentioned before is all the processes appearing for a particle from its generation to its vanishing. To collect all the data corresponding to a single particle, the values for every observable can be stored in histograms or tuples that are then given to the next higher unit to be written in files.
This next higher unit is the **Run Action** class in which the user decides what has to be done before and after the actual simulation as stating the number of particles that are simulated (if its not decided interactively after compilation) as well as opening or closing files for saving the data collected during an *event*.
This way, the simulation results can reach every level of verbosity. The correlations between step, event and run are summarised again in Figure 2.6.

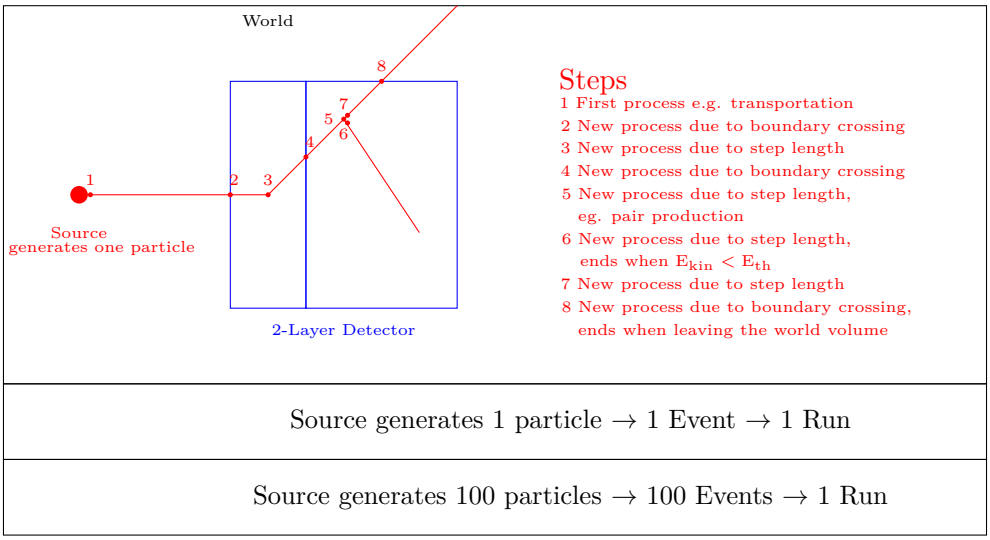

Figure 2.6 Visualisation of the difference between step, event and run. The step is the smallest unit of the simulation. For every step a new process is calculated depending on the cross sections of the appliable processes. Every process has a certain step length. If the particle has travelled this length or crosses a material boundary, a new step starts. All steps for one particle are collected in one event. An event is terminated when the particle leaves the world volume or when its kinetic energy falls below a certain energy threshold E_{th}. Every new primary particle generates its own event. Then all events of the particles generated by the source are summarised in one run.

3 Geant4 version comparability

In the frame of this thesis various versions of the Geant4 code are used. Besides Geant4 10.0.2, the newest version at that time, simulations are done with older versions such as Geant4 9.6.2 and Geant4 9.3.2.
The main part of the simulation is done with Geant4 9.6.2 as it was the actual version at the beginning of this work. Still, in Chapter 7 a project that was implemented for version Geant4 9.3.2 is re-evaluated. As some of the packages containing the physical processes were upgraded since the time of implementation, those packages are not supported any more in newer versions. When the newest version Geant4 10.0.2 was released, it was decided to perform only a simple simulation in each version in order to ensure comparability of the required data. The result of the test is described in this chapter.

3.1 Energy loss of electrons in matter

Electrons suffer an energy loss during the interaction with the atoms and bound electrons of a solid material. The main effects are ionisation and Bremsstrahlung. For relativistic, undistinguishable particles with a mass $\mathrm{m_e}$, especially electrons, the mean energy loss per track length due to ionisation or excitation can be calculated via the relativistic Bethe formula for electrons (Leo, 1994).

$$-\left\langle \frac{\mathrm{d}E}{\mathrm{d}x} \right\rangle = \frac{1}{2}\mathrm{K_{Ion}}\frac{Z}{A}\rho\frac{1}{\beta^2}\left[\ln\left(\frac{\tau^2(\tau+2)}{2(\frac{I}{\mathrm{m_e c^2}})^2}\right) + F(\tau,\beta) - \delta - 2\frac{C(\eta)}{Z}\right]. \tag{3.1}$$

Here, $\mathrm{K_{Ion}} = 4\pi \mathrm{N_A} \mathrm{r_e^2} \mathrm{m_e c^2} = 0.307\,\mathrm{MeV\,cm^2\,mole^{-1}}$ is a constant depending on the Avogadro constant $\mathrm{N_A}$, the classical electron radius $\mathrm{r_e}$ and the rest mass of the electron $\mathrm{m_e c^2}$. The relativistic velocity is introduced as $\beta = \frac{v}{\mathrm{c}}$. The material the electron passes through is characterised by the charge number Z, the element density A, the material density ρ and the mean excitation potential I of the medium in eV. With $\tau = \frac{E}{\mathrm{m_e c^2}}$, the numerical function $F(\tau,\beta)$ is described via

$$F(\tau,\beta) = 1 - \beta^2 + \frac{\frac{\tau^2}{8} - (2\tau+1)\ln(2)}{(\tau+1)^2}. \tag{3.2}$$

The density correction δ is defined as

$$\delta = \begin{cases} 0 & \text{for } X < \mathrm{X_0} \\ 4.6052X + \mathrm{C_0} + \mathrm{a}(\mathrm{X_1} - X)^{\mathrm{m}} = & \text{for } \mathrm{X_0} < X < \mathrm{X_1} \\ 4.6052X + \mathrm{C_0} & \text{for} X > X_1 \end{cases} \tag{3.3}$$

where $\mathrm{X_0}$, $\mathrm{X_1}$, $\mathrm{C_0}$, a and m are material depending constants given for silicon in Table 3.1.

The parameter X is equal to $\log_{10}\beta\gamma$ with the Lorentz factor $\gamma = (1-\beta^2)^{-\frac{1}{2}}$. Finally, the shell correction factor C can be written as

$$C(\eta) = (0.422377\eta^{-2} + 0.0304043\eta^{-4} - 0.00038106\eta^{-6}) \cdot 10^{-6} I^2[\mathrm{eV}] \tag{3.4}$$

$$+ (3.850190\eta^{-2} - 0.1667989\eta^{-4} + 0.00157955\eta^{-6}) \cdot 10^{-9} I^3[\mathrm{eV}], \tag{3.5}$$

with $\eta = \beta\gamma$.

Table 3.1 Numerical constants for the calculation of ionisation effects in silicon. Taken from Leo (1994).

Material	I[eV]	C_0	a	m	X_1	X_0
Silicon	173.5	-4.44	0.1492	3.25	2.87	0.2014

Another effect of energy loss for high energetic electrons is Bremsstrahlung. The energy loss due to Bremsstrahlung for a medium consisting of elements between $Z > 4$ and $Z < 92$ is given via

$$-\frac{\mathrm{d}E}{\mathrm{d}x} \approx \frac{E_0}{X_0} = \mathrm{K_{Brems}} \left\{ Z^2 \left[\ln \frac{184.15}{Z^{\frac{1}{3}}} - f(Z) \right] + Z \ln \frac{1194}{Z^{\frac{2}{3}}} \right\} \tag{3.6}$$

In a first approximation, the energy emission is distributed homogeneously over the radiation length X_0. Here, $\mathrm{K_{Brems}} = 4\alpha \mathrm{r_e} \mathrm{N_A} = (716.408\,\mathrm{gcm}^{-2})^{-1}$ is a constant depending among others on the fine-structure constant α whereas $f(Z)$ is a numerical function with

$$f(Z) = a^2[(1+a^2)^{-1} + 0.20206 - 0.0369a^2 + 0.0083a^4 - 0.002a^6 \tag{3.7}$$

$$a = \alpha Z. \tag{3.8}$$

The energy loss due to Bremsstrahlung as well as the energy loss due to ionisation depends on the initial energy E_0 of the electron. While the ionisation term decreases for higher energies, the term for Bremsstrahlung increases linear with the energy. There is a critical energy where the energy loss is equal for both processes. For most elements this energy lies at some tens of MeV. The mean energy loss for both effects as well as the total energy loss for an electron passing through a medium made of silicon is shown in Figure 3.1. The critical energy is at about 45 MeV. In the simulation performed for the comparability test, electrons with initial energies of 458 MeV will be studied, so the energy is much higher than the critical energy. A dominance of the Bremsstrahlung over the ionisation process is expected.

3.2 Simulation setup of the comparability test

For the comparability test 1,000,000 electrons with an initial energy of 458 MeV interacting with 216 µm silicon plate are studied. The values are taken from Aitken et al. (1969). The origin of the electron is a point source emitting a particle beam perpendicular to the plate surface. The simulated setup is shown in Figure 3.2. For the image only 5000 electrons are used.

For all versions of Geant4 the same simulation code is used. The only differences appear in the construction of the *Physics List*. Because of modifications in the Geant4 code, some newer packages containing physical models are not supported by the older Geant4 version Geant4 9.3.2. Details specifying the packages used for each version are given in Table 3.2 and 3.3. The packages mostly have the same names regardless of their version except for the package for multiple scattering. Whereas in version 9.3.2 the same package is applied to

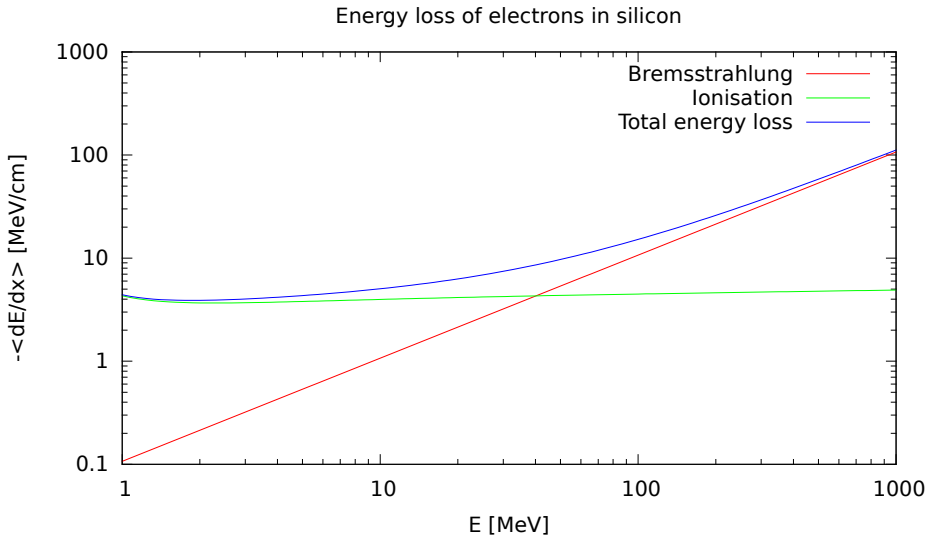

Figure 3.1 Mean energy loss for an electron due to Bremsstrahlung and ionisation in silicon. The radiation length was calculated to $X_0 = 9.34\,\text{cm}$ and the critical energy can be found at 40.21 MeV.

electrons, muons and hadrons, for newer versions one scattering model is used for each class of particles.
Still, the models underlying the packages are highly different. The energy range considered to be well described by each model is noticeable. For the oldest version used, especially the low energy range contains a lot of uncertainties. Some of the models are parametrisations of experimental data instead of full theoretical descriptions. In Geant4 9.6.2 and Geant4 10.0.2, the models and theories applied are specified in details in the documentation whereas it is difficult to find out which models are used for the older version. The simulation with the newer versions are expected to be much more accurate because of a better matching of models and energy range.

As a structural detail, for the newer versions protons and pions are listed separately whereas they are generalised as ions for the old version. This should not have any effect on the outcome of the simulation because pair production and Bremsstrahlung for protons and pions will not appear in this energy range.

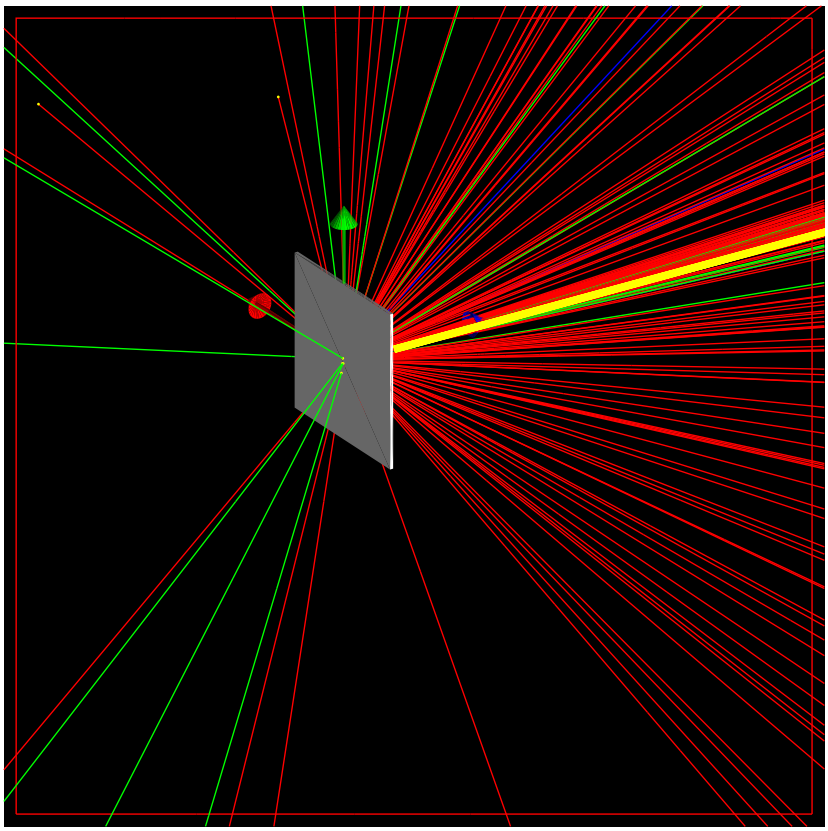

Figure 3.2 Simulated setup for the comparability test of various Geant4 versions. The electrons (red) incide as one beam of particles (yellow) and are scattered or stopped at the silicon plate (grey) mostly due to Bremsstrahlung in the field of the positive ions contained in the plate. The green lines indicates photons that are generated in the Bremsstrahlung process. There is also one blue line indicating the track of a positron originating from a pair production process of a photon created by Bremsstrahlung.

Table 3.2 Geant4 packages used for the Physics List of the version Geant4 9.3.2 The presented energy range is defined as *range of good description* in the Geant4 documentation. It is γ = photon, e^- = electron, e^+ = positron and μ = muon.

Particle	Package	Energy Range	Model
γ	G4PhotoElectricEffect	0 eV-10 TeV	Sandia parametrisation
	G4ComptonScattering	10 keV-100 GeV	Klein-Nishina model
	G4GammaConversion	1.5 MeV-100 GeV	Bethe-Heitler model
e^-/e^+	G4MultipleScattering	100 eV-100 TeV	UrbanMsc92: semi-empirical model based on Lewis theory
	G4eIonisation	1 keV-100 GeV	Moller-Bhaba
	G4eBremsstrahlung	1 keV-10 GeV	Standard model for Bremsstrahlung for e^-/e^+
		10 GeV - 10 TeV	Improved model including LPM[1] effect
e^+	G4eplusAnnihilation	100 eV-100 TeV	eplus2gg model: model for conversion of one e^+ in two γ
μ^-/μ^+	G4MultipleScattering	100 eV-100 TeV	UrbanMsc92: semi-empirical model based on Lewis theory
	G4MuIonisation	0 eV-200 keV	Bragg model
		200 keV-1 GeV	Bethe-Bloch model
		1 GeV-10 TeV	Bethe-Bloch model for muons
	G4MuBremsstrahlung	0 eV-10 TeV	Parametrised model for Bremsstrahlung
	G4MuPairProduction	100 eV-100 TeV	Parametrised model for pair production
Ions	G4MultipleScattering	100 eV-100 TeV	UrbanMsc92: semi-empirical model based on Lewis theory
	G4ionIonisation	100 eV-2 MeV	Bragg model
		2 MeV-100 TeV	Bethe-Bloch model

[1] LPM: Landau-Pomeranchuk-Migdal effect

Table 3.3 Geant4 packages used in the Physics List for the versions Geant4 9.6.2 and Geant4 10.0.2. It is γ = photon, e^- = electron, e^+ = positron, μ = muon and π = pion.

Particle	Package	Energy Range	Model
γ	G4PhotoElectricEffect	0 eV-10 TeV	Gavrila-Sauter model
	G4ComptonScattering	0 eV-10 TeV	Klein-Nishina model
	G4GammaConversion	0 eV-80 GeV	Bethe-Heitler model
		80 GeV-10 TeV	Bethe-Heitler with LPM effect
e^-/e^+	G4eMultipleScattering	0 eV-10 TeV	UrbanMsc95: semi-empirical model based on Lewis theory
	G4eIonisation	0 eV-10 TeV	MollerBhaba: Moller-Bhabha model
	G4eBremsstrahlung	0 eV-1 GeV	Seltzer-Berger model
		1 GeV-10 TeV	Bremsstrahlung with LPM effect
e^+	G4eplusAnnihilation	0 eV-10 TeV	eplus2gg: Annihilation of an electron-positron pair into two gammas
μ^-/μ^+	G4MuMultipleScattering	0 eV-10 TeV	UrbanMsc95: semi-empirical model based on Lewis theory
	G4MuIonisation	0 eV-200 keV	Bragg model
		200 keV-2 MeV	Bethe-Bloch model
		2 MeV-10 TeV	Bethe-Bloch model for muons
	G4MuBremsstrahlung	0 eV-10 TeV	Bremsstrahlung model for muons
	G4MuPairProduction	0 eV-10 TeV	Pair production model for muons
Proton/π^-/π^+	G4hMultipleScattering	0 eV-10 TeV	UrbanMsc95: semi-empirical model based on Lewis theory
	G4hIonisation	0 eV-2 MeV	Bragg / ICRU73Q0: model for the ionisation due to anti-hadrons by the International Commission on Radiological Protection
		2 MeV-10 TeV	Bethe-Bloch
	G4hBremsstrahlung	0 eV-10 TeV	Bremsstrahlung model for hadrons
	G4hPairProduction	0 eV-10 TeV	Pair production model for hadrons
Ions	G4hMultipleScattering	0 eV-10 TeV	UrbanMsc95: semi-empirical model based on Lewis theory
	G4ionIonisation	0 eV-2 MeV	Bragg / ICRU73Q0: model for the ionisation due to anti-hadrons by the International Commission on Radiological Protection
		2 MeV-10 TeV	Bethe-Bloch

3.3 Output and evaluation of the data

During the simulation, the stepping action is used to collect all energy deposited inside the silicon plate and to pass it to the event action where it is written in tables.
In this simulation the table consists of two columns, one contains the total energy deposited in the plate during one event, the second one contains the original input energy for the primary electron of the same event.
The output files of the Geant4 simulations are created in the csv[2]-format for the two newer versions and in the dat-format for the older one. Geant4 also supports other file formats such as root or xml[3]. The collected data are evaluated with the Python based computer program *histo_main.py* written for this project. It provides several tools for the handling of data and is specialised in generating histograms. A manual for histo_main is given in the Appendix 3.1. During the evaluation for each simulation a histogram is produced showing the deposited energies normalised on the bin width in keV.

To take a closer look on the processes that appear during the simulation an additional file is produced, tabulating the sequential number of the actual event, the position and the name of the particle, the volume in which the previous process took place, the name of the process taking place as well as the deposited energy. These data are stored in the dat-format.

3.4 Results of the comparability test

The processes taken in every step inside the volume of the plate are summarised in Table 3.4. Also the behaviour of gammas produced during the interaction is listed. The energy loss due to transportation includes ionisation and collision losses that produce secondary particles whose travelling distance is smaller than 0.1 mm. This is the so called *cut range*[4] that has to be defined in the Physics List of every simulation. Still, in all three simulations, the energy loss due to the ionisation process is strongly outweighed by the loss due to Bremsstrahlung with a factor of about three even when adding the transportation loss to the ionisation loss. Because the incident energy of the electrons at 458 MeV is far from the critical energy, this behaviour was expected by theory. Finally, the multiple scattering process is more numerous than ionisation and Bremsstrahlung, still the energy loss during those processes is small by comparison. It amounts only about one third of the mean Bremsstrahlung loss.

The produced gammas are–apart from simple transportation–predominately absorbed due to the photoelectric effect. The energy of those absorbed photons can be detected inside the silicon plate. All other photons can leave the sensitive volume by Compton scattering or by simply passing through the material without interaction. Some high energetic photons are able to undergo pair production, but the mean rate of this process is 0.48 %.

The resulting energy losses are summarised in Figure 3.3. It can be seen that the curve produced by Geant4 9.6.2 matches the one by Geant4 10.0.2 over the whole energy range. For the Geant4 9.3.2 the rising edge at low energies has a small offset as well as a slightly flatter slope. The peak energy is at about 695 keV for all three curves even if the count rate for the Geant4 9.3.2 curve is about 9 % lower than for the other curves. For energies larger than

[2] csv: comma separated values
[3] xml: EXtensible Markup Language
[4] cut range: The cut range defines a length or an energy threshold. If the considered particle not able to travel this length of if its energy falls under this threshold, it will not be further calculated. This effect suppress the generation of secondary particles in some cases.

Table 3.4 Analysis of the rate and energy loss of the processes appearing inside the silicon plate volume. To obtain high statistics, for each simulation 10^5 events were iterated. One process is chosen in every single step. A step is counted for this table when the particle was inside the silicon plate volume during this step. Hereby, MSC stands for multiple scattering processes. For every process, the number N of occurrences, the total energy loss E_{tot} due to this process as well as the mean energy $\bar{E}$ loss for one step is shown.

Electron							
		Transportation			Ionisation		
Version	N_{Step}	N	E_{tot} [MeV]	$\bar{E}$ [keV]	N	E_{tot} [MeV]	$\bar{E}$ [keV]
Geant4 9.3.2	305,148	105,286	54,425.20	516.93	63,582	46,393.76	729.67
Geant4 9.4.3	305,422	105,298	54,435.36	516.96	63,458	44,449.53	700.46
Geant4 9.6.2	200,305	103,616	31,211.71	301.22	29,841	21,512.58	720.91
Geant4 10.0.2	200,836	103,556	31,216.25	301.44	30,128	20,602.56	683.83

Electron							
		MSC			Bremsstrahlung		
Version	N_{Step}	N	E_{tot} [MeV]	$\bar{E}$ [keV]	N	E_{tot} [MeV]	$\bar{E}$ [keV]
Geant4 9.3.2	305,148	105,589	3,842.84	36.39	30,737	968,264.94	31,501.61
Geant4 9.4.3	305,422	105,579	3,824.39	36.22	31,087	977,797.86	31,453.59
Geant4 9.6.2	200,305	51,737	1,560.51	30.16	15,111	508,332.68	33,639.91
Geant4 10.0.2	200,836	52,211	1,527.32	29.25	14,941	498,205.05	33,344.83

Gamma							
		Transportation			Compton		
Version	N_{Step}	N	E_{tot} [MeV]	$\bar{E}$ [keV]	N	E_{tot} [MeV]	$\bar{E}$ [keV]
Geant4 9.3.2	34,553	28,492	0.0	0.0	499	401.09	803.79
Geant4 9.4.3	30,932	28,872	0.0	0.0	504	593.99	1,178.55
Geant4 9.6.2	15,140	14,295	0.0	0.0	116	263.35	2,270.26
Geant4 10.0.2	14,985	14,121	0.0	0.0	130	55.87	429.77

Gamma							
		Photoelectric effect			Pair production		
Version	N_{Step}	N	E_{tot} [MeV]	$\bar{E}$ [keV]	N	E_{tot} [MeV]	$\bar{E}$ [keV]
Geant4 9.3.2	34,553	2,129	36.23	17.01	57	6,651.77	116,697.72
Geant4 9.4.3	30,932	2,112	33.67	15.94	44	5,231.16	118,890.00
Geant4 9.6.2	15,140	712	10.68	15.0	17	1554.28	91,428.25
Geant4 10.0.2	14,985	725	10.63	14.66	9	564.92	62,768.89

1,700 keV, the curves separate again when they decrease more rapid for the former version than for the newer ones. However, statistics in this range are low with a maximum count rate of 10 counts/keV.
These differences are thought to appear due to the discrepancy in the models applied which are corrected with respect to the very low and the very high energy behaviour since version Geant4 9.3.2. Still, between about 750 keV and 1,700 keV the versions are assumed to be comparable.
For this work it is concluded to that the newer Geant4 versions are implemented more reliable. That is why for the most simulations of this thesis the version Geant4 9.6.2 is used because there is more experience with this version than with the actual version Geant4 10.0.2. For the re-evaluation of the code written in Geant4 9.3.2 in Chapter 7 additional packages will be included to correct the differences at very low and high energy ranges.

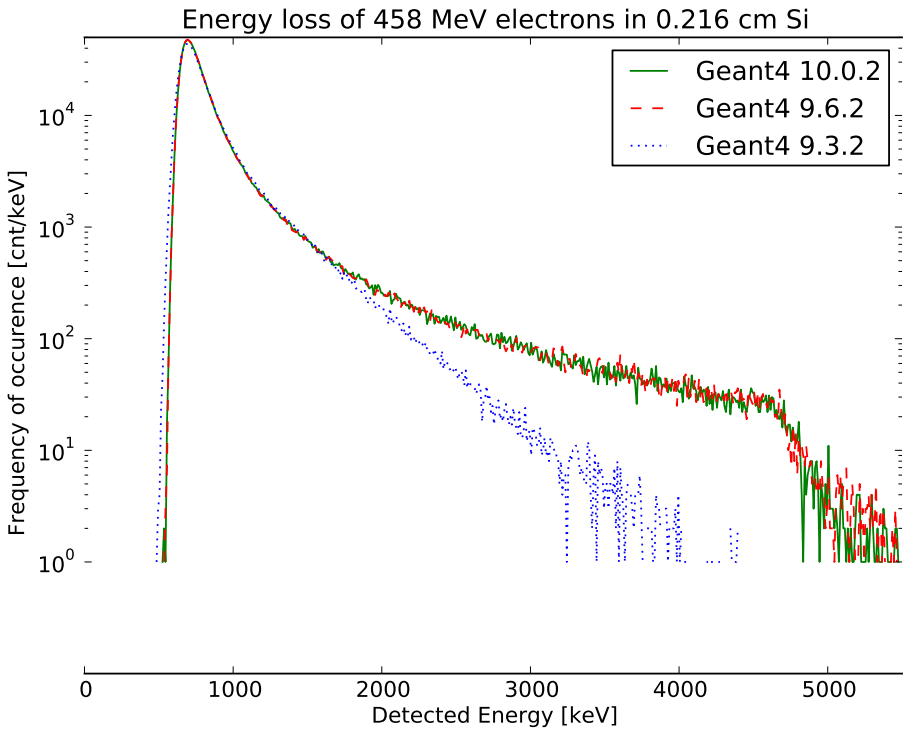

(a) Whole simulated energy spectrum

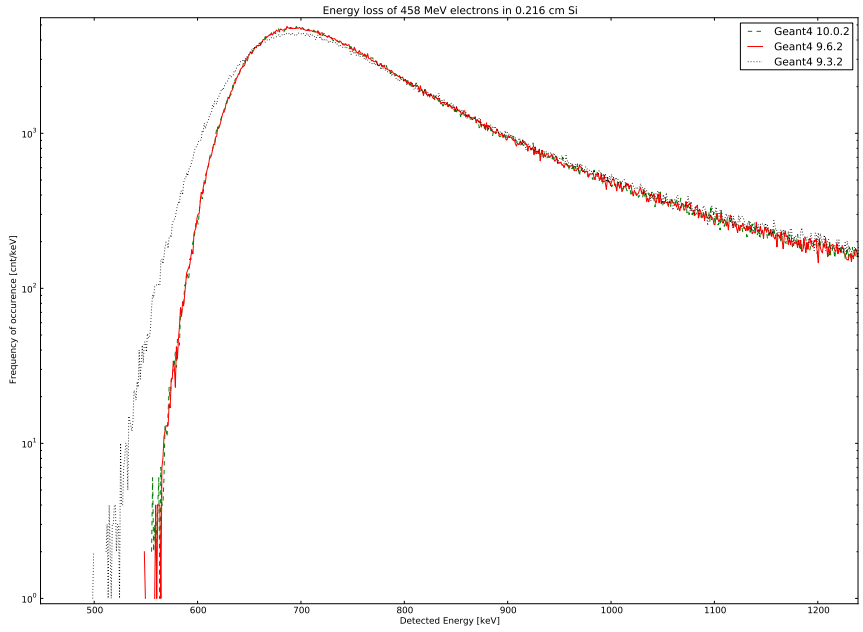

(b) Low energy range of the energy spectrum

Figure 3.3 Results of the electron energy loss simulation for the comparability test of various Geant4 versions. The differences in the very low and very high energy range is visible. Between about 600 keV and 1,700 keV the simulation results are in good agreement.

4 eROSITA: Quantum efficiency simulation

The ***e**xtended **RO**entgen **S**urvey with an **I**maging **T**elescope **A**rray* (eROSITA) is an X-ray telescope designed to conduct a sky survey in the X-ray band up to 10 keV. The goal of the mission is to study the structure of the universe especially of the hot intergalactic medium in and around galaxy clusters, active galactic nuclei and other X-ray sources in our galaxy (Predehl, 2014). A CAD model is shown in Figure 4.1.

Figure 4.1 The eROSITA telescope will survey sources in and beyond our galaxy in the X-ray spectrum. CAD model from Predehl (2010).

eROSITA is a project of the MPE[1], in cooperation with several international research institutes, including the IAAT[2]. The eROSITA instrument will be launched in 2016 on-board the German/ Russian satellite *Spektrum-Röntgen-Gamma* (SRG).

In this chapter a simulation done for the eROSITA mission is presented. The goal of the simulation was to reproduce the measured values by Ebermayer et al. (2010) about the quantum efficiency of an eROSITA detector. The test is also used to check the correct implementation of the simulation code regarding the event detection and the evaluation of deposited energy. In a first section the concept of quantum efficiency is explained, followed by a section about the construction and functionality of the simulated setup. At the end of the chapter the results found during the simulation are discussed.

4.1 Quantum efficiency

For photon detection different detection techniques are used for different energy bands to collect the relevant photons and suppress with energies higher or lower than the required energy range. The absorption capacity of the utilized materials is a key factor for the quality

[1]MPE: Max-Planck-Institute for extraterrestrial physics in Garching, Germany
[2]Institut für Astronomie und Astrophysik Tübingen

of a detector. A quantity identifying the ability of an instrument in handling incident photons, is the quantum efficiency. In the context of this study it is defined as the amount of the incident photons that can be detected with their initial energy by an instrument. In this work the quantum efficiency was tested for a sensitive detector part without additional shieldings, optics or electronics.

When the photon is not reflected at the surface of the detector, the main effect causing a photon to be not fully detected, is absorption in upper layers of the detector (oxide layers), so that the photon cannot reach the sensitive part of the detector. On the contrary high energy photons can leave the detector without any interaction or via scattering processes and are consequently not detected or detected with a fraction of their energy. If a photon is absorbed or not, depends on the absorption length $\lambda_{abs} = (\mu\rho)^{-1}$, where μ is the absorption coefficient and ρ the density of the medium. The absorption process is described by the Bouger-Lambert-Beer's law.

$$I(d) = I_0 \exp(-\frac{d}{\lambda_{abs}}) \tag{4.1}$$

For a thickness d of a layer, a photon will be generally absorbed for $\lambda_{abs} \ll d$ and passes through without interaction for $\lambda_{abs} \gg d$.

Other smaller effects mentioned by Ebermayer et al. (2010) are the production of photoelectrons in the oxide layer, energy loss at the boundaries between the layers as well as a escaping fluorescence emission.
Photoelectrons are generated when photons are absorbed in the oxide layers. The electrons lose energy on their way through the layers due to the effects that were discussed in Chapter 3. The energy reaching the sensitive volume of detector is therefore lower than the initial one of the photon. This effect is especially large when the energy of the incident photon is equal to the binding energy of shell electrons from the material atoms. This produces edges in the quantum efficiency spectrum. In the considered energy range of up to 11 keV and with the applied materials only K 1s shell absorption can be found in the spectrum.
The same can be assumed for photons scattered at the boundary regions of the layers. They can also lose energy in the collision process and can even be scattered out of the detector volume and get lost for the measurement.
Furthermore, photons entering the detector can excite K-shell electrons from the detector material producing fluorescence photons that escape from the detector. The remaining energy that is measured in the detector corresponds to the difference between the initial photon energy E_0 and the K-shell transition energy that is 1.74 keV in the case of silicon.

Only photons that were stopped in the sensitive detector layer by depositing their entire energy inside this layer were valid for the quantum efficiency. Those photons can be used for spectroscopic measurements. Therefore, the knowledge of the quantum efficiency of a detector is of crucial relevance for the success of a measurement.

4.2 Simulation setup of the eROSITA comparison

The detector construction in this simulation corresponds to the setup of the originally utilized pnCCDs[3] as far as they were mentioned in the research paper. For the detection of the X-ray

[3] CCD: see Section 1.4.2.3

photons, a CCD made of silicon with a thickness of 450 µm is used. The doping needed to ensure the functionality of the CCD is one doping element to 10^6 silicon atoms and can be neglected in the simulation. On top of the sensitive part of the detector two oxide layers are located. The first layer with a thickness of 30 nm is made of silicon dioxide (SiO_2) whereas the second layer has a thickness of 40 nm and is made of silicon nitride (Si_3N_4).
Another layer made of 200 nm pure aluminium serves as a filter for optical photons that would generate a background interfering with the X-ray signal. The layers are quadratic and have an edge length of 10 cm. The layer thicknesses are taken from Granato (2012).

As in the laboratory experiment an energy range from 200 eV to 11 keV in steps of 1 keV was considered. For each energy 1,000 photons were simulated. The origin of the photon beam was positioned in a distance of 100 cm perpendicular to the centre of the detector plane.
A snap shot taken during a simulated measurement is shown in Figure 4.2. Of the several layers only the silicon layer is made visible.

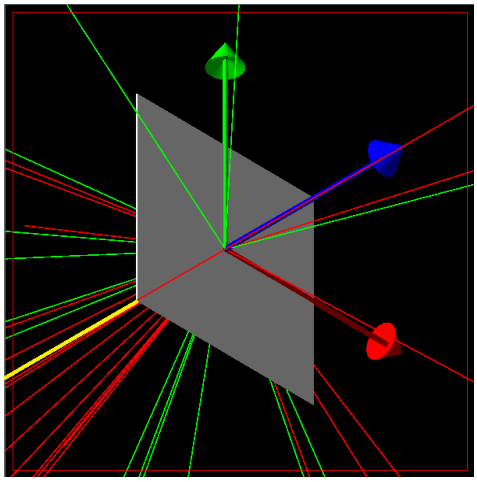

Figure 4.2 Simulated setup of a quantum efficiency measurement. The photons (green) arrive as one beam (yellow) and are absorbed by the detector (grey). Others are scattered or reflected at the detector surface. Additionally, it is possible that the photons exceed the binding energy of electrons (red) that are then free to leave the detector material. Only photons where the initial energy was detected completely are counted for the quantum efficiency.

The simulation was run with Geant4 9.6.2 and the same Physics List was used as for the comparability test in the previous section.

4.3 Output and evaluation of the data

In contrast to a real laboratory experiment, in the simulation it is possible to distinguish between fully and partly absorbed photons in an easy way. The output file of the simulation this time contains a table with three columns. In the first one the energy deposited in the detector is stated only if it is equal to the input energy else it is set to zero. For normalisation and monitoring in the second and third column the generated input energy and the deposited energy for each event are stored.
For the evaluation a histogram is produced of the first column neglecting the zero-valued rows. The histogram is then normalised to the number of incident photons for every energy. For this purpose a second histogram was generated for the input energies and the count values of the quantum efficiency histogram were divided by those of the input histogram.

Table 4.1 Example of an output table generated during the eROSITA simulation. The first column is set to a non-zero value whenever the detected energy is equal to the input energy. Then the value in the fist column is set to this energy. For the evaluation, a histogram is produced for the first column. Zero-valued columns are neglected. In the displayed table, a histogram would be produced with two counts for the value 480 keV and one count for 481 keV.

Output [keV]	Input energy [keV]	Detected energy [keV]
0	480	0
480	480	480
480	480	480
0	480	470
0	480	479
481	481	481
⋮	⋮	⋮

4.4 Results of the quantum efficiency simulation

A plot with the results of the simulation and the measured data by Ebermayer et al. (2010) can be found in Figure 4.3. The tabulated data are provided in the Appendix 4.1. It can be seen that the values from the laboratory measurement match the simulated curve of the quantum efficiency. The small incisions on the rising edge of the curve are absorption edges from the oxide layers, the large one corresponds to the aluminium filter. If the energy increases, the ionisation of K-shell electrons becomes more probable. The ionisation cross section is increased and consequently the absorption probability in the oxide layers rises which leads to a reduction in the quantum efficiency.
The absorption edges of the laboratory measurement seem to be slightly deeper than the ones from the simulation. They are shown in more detail in Figure 4.4 and their position is compared with theoretical values in Table 4.2. The values for the position found in the simulation match the theoretical expectations.

Table 4.2 Comparison between the binding energy of the detector material and the energy position of the absorption edges. In the second column the binding energy of K 1s shell electrons is given in eV (Center for X-Ray Optics Advanced Light Source, 2001) while the third column lists the positions of the absorption edges measured during the simulation. Within the given accuracy the values for the positions match the theoretical expectations.

Element	K 1s shell [eV]	Absorption in simulation [eV]
7 N	409.9	415±15
8 O	543.1	540± 10
13 Al	1,559.6	1,560±20
14 Si	1,839	1,850±20

The simulation reproduces well the general behaviour of the quantum efficiency. The absorption edges are found at the expected positions which also match the measured data. However, the depth of the measured data are deeper than the ones found in the simulation. This could be due to differences in the thicknesses of the oxide layers.

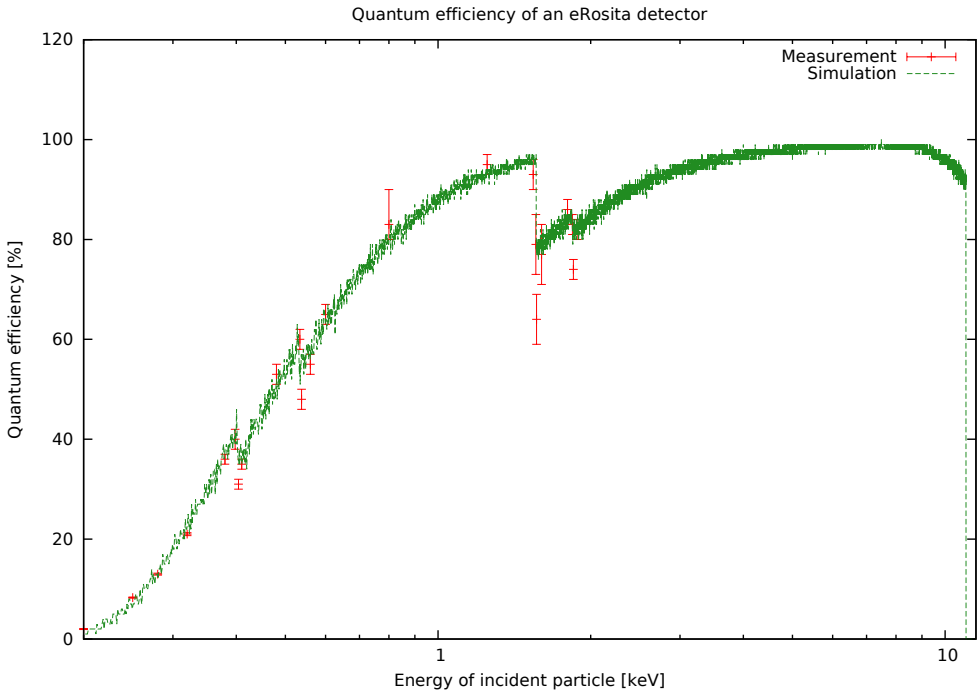

Figure 4.3 Comparison of the simulated data with the data found by Ebermayer et al. (2010). The edges correspond to absorption due to K shell absorption of the incident photons. The bin width of the histogram for the simulation is 2 eV.

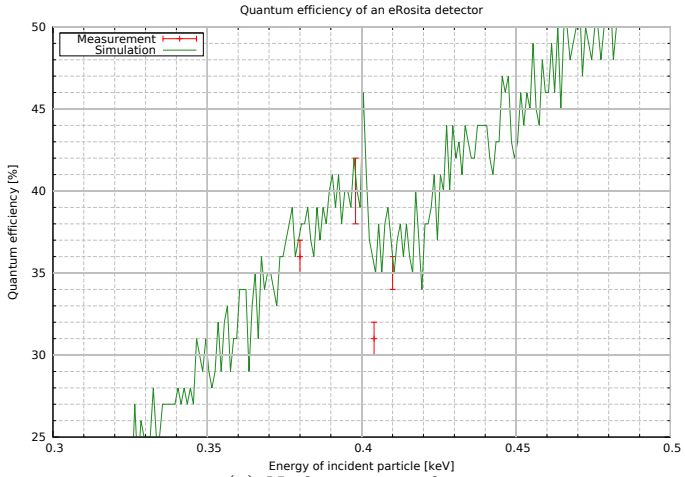

(a) N absorption edge

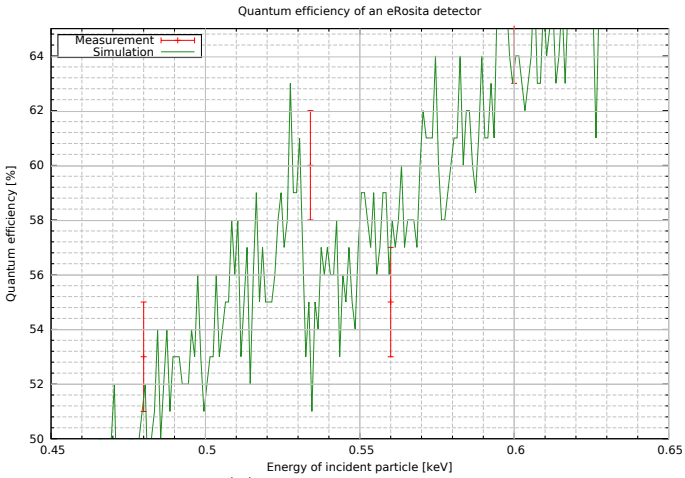

(b) O absorption edge

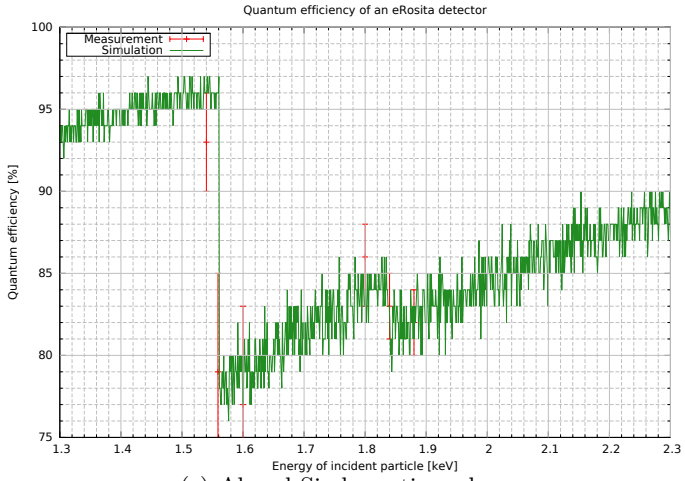

(c) Al and Si absorption edges

Figure 4.4 Detailed view of the absorption edges found in the quantum efficiency spectrum for the eROSITA detector. The absorption edges for all included elements could be found near the expected energy.

5 Compton camera

This chapter is intended to provide information about a reconstruction algorithm used in the following chapter. All simulations performed are exemplary to test the functionality of the algorithm and the dependencies of the setup.

A Compton telescope is an instrument which can be used to determine the position of X-ray and Gamma-ray sources by reconstructing the Compton scattering process of multiple photons originating from these sources. One of the most successful Compton telescopes was the COMPTEL[1] instrument on-board the satellite CGRO[2]. COMPTEL had a field-of-view of about 1 steradian and could locate gamma-ray bursts with an accuracy better than 1°.

CGRO was a NASA observatory launched in 1991 and did the first sky-survey in the energy range above 100 MeV. The Compton telescope itself was developed by the MPE, SRONU[3], UNH[4] and the Research and Scientific Support Department (RSSD) of ESA/ESTEC in Noordwijk, the Netherlands.

The structure and the reconstruction technique of the Compton telescope simulated in this chapter will be different to those used for the observatory described above. A reconstruction algorithm will be developed valid for sources close to the detector with a known distance. Therefore it is called *Compton camera*. The differences to an astronomical telescope are discussed at the end of the chapter.

5.1 The Compton effect

The Compton effect describes the scattering process of photons on free electrons. Photons have an energy $E = \mathrm{h}\nu$ and a momentum $p = \hbar k$ where $k = \frac{2\pi}{\lambda}$ is the absolute value of the wave vector in dependency on the wavelength λ and $\hbar = \frac{\mathrm{h}}{2\pi}$ with h the Planck constant. Before the scattering, the electron has only rest energy $E_\mathrm{e} = m_\mathrm{e}\mathrm{c}^2$ with m_e the rest mass and c the speed of light. The process of the Compton scattering is shown in Figure 5.1. Because of the conservation of energy and momentum it is possible to obtain the Compton wavelength which is a characteristic quantity for every particle.

$$\mathrm{h}\nu + m\mathrm{c}^2 = \mathrm{h}\nu' + \sqrt{m^2\mathrm{c}^4 + p_\mathrm{e}'^2 c^2} \tag{5.1}$$

$$\vec{p_\gamma} = \vec{p'}_\mathrm{e} + \vec{p'}_\gamma \tag{5.2}$$

$$\mathrm{h}\nu + m\mathrm{c}^2 = \mathrm{h}\nu' + \sqrt{m^2\mathrm{c}^4 + \left[\left(\frac{\mathrm{h}\nu}{\mathrm{c}}\right)^2 + \left(\frac{\mathrm{h}\nu'}{\mathrm{c}}\right)^2 - 2\frac{\mathrm{h}^2\nu\nu'}{c^2}\cos(\alpha)\right]\mathrm{c}^2}, \tag{5.3}$$

whereby the absolute value of the photon's momentum p_γ is written as the quotient of its energy $\mathrm{h}\nu$ and the speed of light. The angle α indicates the angle between the photon

[1] COMPTEL: COMPton TELescope
[2] CGRO: Compton Gamma Ray Observatory
[3] SRONU: Space Research Organization of the Netherlands in Utrecht, the Netherlands
[4] UNH: University of New Hampshire, USA

momenta before and after the scattering. This leads to

$$\frac{\nu - \nu'}{\nu\nu'} = \frac{\mathrm{h}}{mc^2}(1 - \cos(\alpha)). \tag{5.4}$$

By using the basic equation of physical optics, $\mathrm{c} = \lambda\nu$, the modification of the wavelength can be calculated to

$$\Delta\lambda = \lambda' - \lambda = \frac{\mathrm{h}}{mc}(1 - \cos(\alpha)). \tag{5.5}$$

$\frac{\mathrm{h}}{mc}$ is called the *Compton wavelength* and depends only on the rest mass of the considered particle.
Measuring the direction and the wavelength shift of Compton scattered photons allows to conclude on the scattering angle α and the direction of the incident photons. This is the basic idea behind a Compton camera assuming that by analysing the path of many photons, their source can be found.

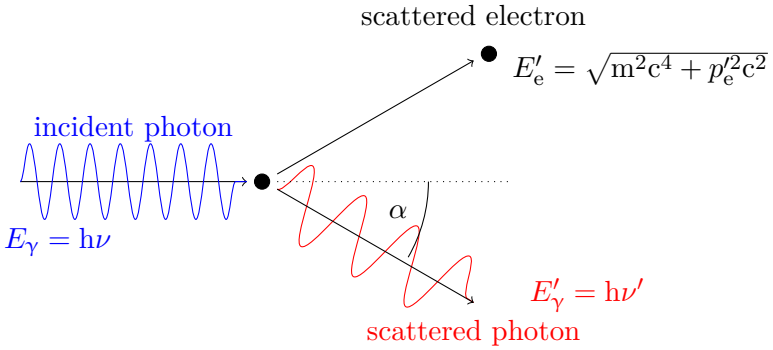

Figure 5.1 Schematic procedure of a Compton scattering process. The incident photon is scattered on an electron at rest. Due to the energy transfer, the wavelength of the scattered photon is increased. Here, α is the scattering angle.

5.2 Simulation setup of a Compton camera for a near source

As mentioned before, the algorithm developed in the process of this work for the reconstruction of the source position of the incident photons is focused on sources that are close to the detector and whose distance is known. For astronomical source positions assumed to be infinity another algorithm would be needed because in this case the source emits parallel light. The algorithm for this case is described at the end of this chapter.

The simplest version of a Compton camera consists of two detectors that are positioned in a certain distance from each other. The setup should be located in vacuum to suppress interactions with extrinsic particles. In the following simulation a cylindric form is chosen for the detectors with a radius of 4 cm and a distance of 1 cm from each other. During the simulation various thicknesses were tested for the detectors. In the following the detector which is closer to the source position is called the *first detector* while the other one is referred to as the *second detector*.

Exemplary, as a source, a beam of photons with an energy of 100 keV is generated. For higher energies additional detector layer can be useful to improve the quantum efficiency of the camera. This technique is treated in an additional section later in this chapter.

The point source is simulated at a distance of 100 cm from the detectors emitting a laser-like beam directed to the centre of the detector. Depending on the measurement, the source is translated in the x- or y-direction to simulate sources at different positions. The angular position varies between 0° and 17.6° for the different measurements. An image of the simulated detector geometry can be found in Figure 5.2.

The simulation was performed with Geant4 9.6.2 and the Physics List from the previous simulation was reused.

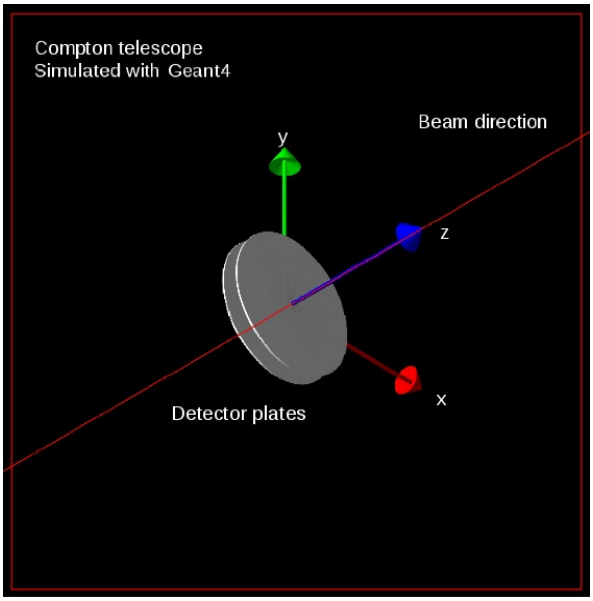

Figure 5.2 Geometry of the simulated Compton camera. The photons travel in the direction of the positive z-axis.

If a photon passes through the geometry, it can trigger events in both detector plates. With the help of the two interaction positions and the deposited energy of multiple photons, the source position can be reconstructed. For this purpose, the so-called *Compton cone* has to be calculated for the photons, describing all positions from which the photons can originate to be scattered in the measured way. The line connecting the two interaction points is the axis of symmetry of the cone while the opening angle α results from the energy loss during the scattering (see Figure 5.3).

By intersecting the calculated Compton cones with a plane parallel to the detector area in the known distance of the source the so called *event circle* (Schönfelder, 1981) can be generated (see Figure 5.4). Provided that the incident photons are completely absorbed in the lower detector with full energy deposition, the event circles of a large number of photons should intersect in a single point which indicates the position of the source.

However, these circles are only approximations because the further the cones are tilted with respect to the z-axis the more elliptic are the resulting intersection lines. Thus, in this work, event ellipses are used in order to get a higher accuracy of the reconstruction. The calculations needed for the reconstruction are described in detail in the next section.

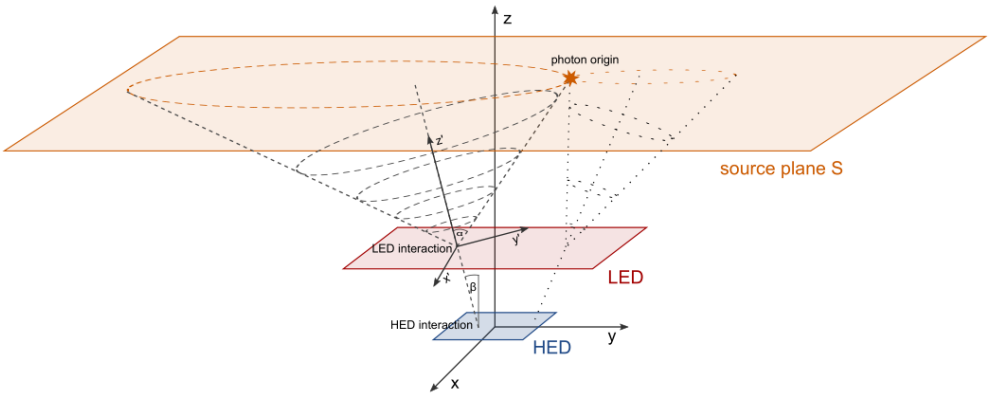

Figure 5.3 Geometrical consideration of the processes in the Compton camera. Compton cones for two individual photons are shown. At the source plane S, the cones intersect in one point, which indicates the origin of the photons. For the reconstruction, for every cone an individual coordinate system is used as it is shown here. The interaction points of the upper detector (here called LED) and the lower detector (here called HED) are further indicated as $\vec{x}_1$ and $\vec{x}_2$. Image taken from (Maier et al., 2014).

5.3 Output and evaluation of the data

The evaluation is done with the Python program **compton_main.py**. It allows the reconstruction of the source position via the calculations that are described in the following.
During the simulation every time a photon enters the sensitive volume of one of the detectors, the time stamp and the position of the interaction is stored as well as the energy deposited in the detector. Also events without energy deposition are stored. They are separated in a later step. Furthermore, the input energy of the photon when leaving the source is saved. The latter is not used for the reconstruction of the source position but for a statistical analysis of the processes. An event is called valid, if energy is deposited in both detectors and if the time of interaction in both detectors differs by no more than a nanosecond.

Before the actual reconstruction process begins, the valid events have to be classified, because still not all of them are usable for the calculations: in a laboratory experiment there is no easy way to discriminate between partial and complete absorption of the photon on its way through the detector geometry. The simulation could perform the differentiation but will not for reasons of comparability. Only events with full energy absorption are classified as *true* events (Figure 5.5(a)).
If the photon is not completely absorbed in the second detector, the calculation of the opening angle is erroneous and the calculated Compton cone does not necessarily contain the true source position. The probability of this happening depends on the quantum efficiency of the detectors. For small photon energies, photoelectric absorption dominates over Compton scattering, so that only few photons leave the camera unabsorbed by passing through the first and the second detector. The higher the energy, the higher is the number of only partly absorbed photons. Still, those photons are used for the reconstruction and classified as *partial* events (Figure 5.5(b)).

Apart from complete and partial absorption, there are other effects that lead to an error in the position reconstruction. For instance, there is the possibility of Compton scattering at the second detector (Figure 5.5(c)). The backscattered photon deposits energy in the first detector again which leads to the assumption that the energy transferred during the scattering

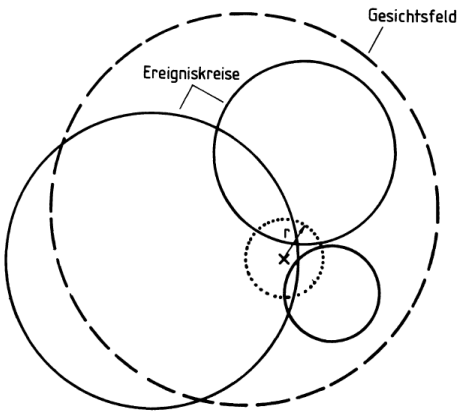

Figure 5.4 Intersections of the Compton cones with a plane in a certain distance. For events with full energy deposition in the detectors all circles should intersect in one point which corresponds to the direction of the source if given in angular units. Here, the three circles drawn with solid lines are the event circles (*Ereigniskreise*) whereas the the circle with the dashed line is the field of view (*Gesichtsfeld*) of the detector. The small circle with radius r drawn with a dotted line is an approximation circle for the source position to take into account the uncertainties of the measurement (Schönfelder, 1981).

is larger than it is in truth and thus to the reconstruction of an inaccurate scattering angle. Those events are classified as *false* events.
Also, there is a chance that the photon transfers energy to an electron and be backscattered (Figure 5.5(d)) or absorbed in that process. If the energy is high enough, the electron can emerge from one of the detectors and can trigger an event in the other detector. This can happen due to the photoelectric (Figure 5.5(f)) or the Compton effect (Figure 5.5(e)). The latter case is also classified as *false* event because the amount of energy deposited in the first detector is too high. In the case of electron emission due to the photoelectric effect just before leaving the first detector, only a part of the energy is deposited in the detector. These events are recognised as *partial* events by the reconstruction algorithm and lead to an error in the reconstruction.

Most of these false background events can be suppressed by the calculation of the largest possible scattering angle and the corresponding limit for the energy deposited in the first detector. If the photon hits the first detector from a direction perpendicular to the detector area exactly in the centre, the scattering angle has to be smaller than

$$\vartheta = \arctan\left(\frac{r_{\mathrm{Detlow}}}{\mathrm{Gap}}\right) \tag{5.6}$$

in order to be able to reach the second detector at all (see Figure 5.6). Here r_{Detlow} is the radius of the lower detector whereas Gap is the distance between the two detectors. For the case of a non perpendicular direction of arrival, the tilting angle must be added to ϑ. For this tilting angle the half opening angle of the field-of-view of the camera can be used.

From Subsection 5.1 the formula for the Compton effect is known. Using Formula **??** for the Compton scattering and solving it for E' with the above computed angles, the maximal energy that can be deposited in the upper detector is

$$E' = \frac{1}{(m_{\mathrm{e}}\mathrm{c}^2)^{-1}(1-\cos\vartheta_{\mathrm{max}}) + \frac{1}{E}} \tag{5.7}$$

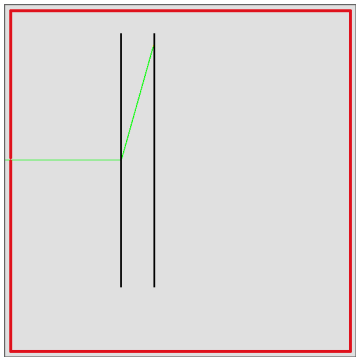

(a) True event: the photon triggers an event in the first detector and is thereafter stopped in the second one.

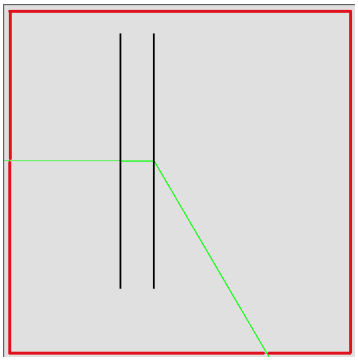

(b) Partial event: the photon triggers events in both detectors but is scattered in the second detector without deposing its full energy.

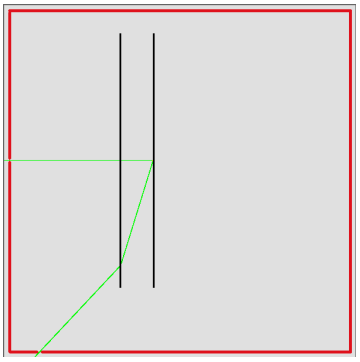

(c) False event: the photon triggers events in both detectors but is then backscattered into the first detector.

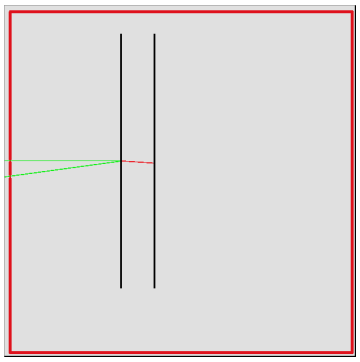

(d) False event: the photon is backscattered in the first detector by producing an electron which triggers an event in the second detector.

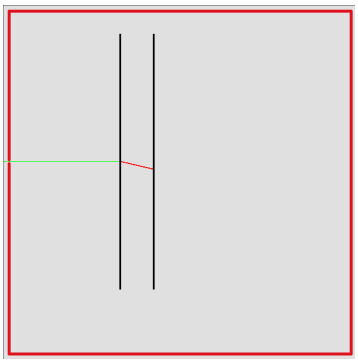

(e) False event: the photon is stopped in the first detector by producing an electron due to the energy transfer of the Compton effect. This secondary particle triggers an event in the second detector.

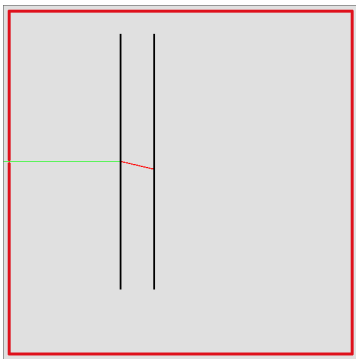

(f) True/partial event: the photon is stopped in the first detector by producing an electron due to the photoelectric effect. This secondary particle triggers an event in the second detector. If the photoelectric effect is processed just before the photon would leave the upper detector, the energy deposition is too low to be recognized as a false event.

Figure 5.5 Events in the Compton camera classified as true, partial or false events. Hereby, green lines correspond to photon tracks, red lines to electron tracks. The incident photons enter from the left side of the image.

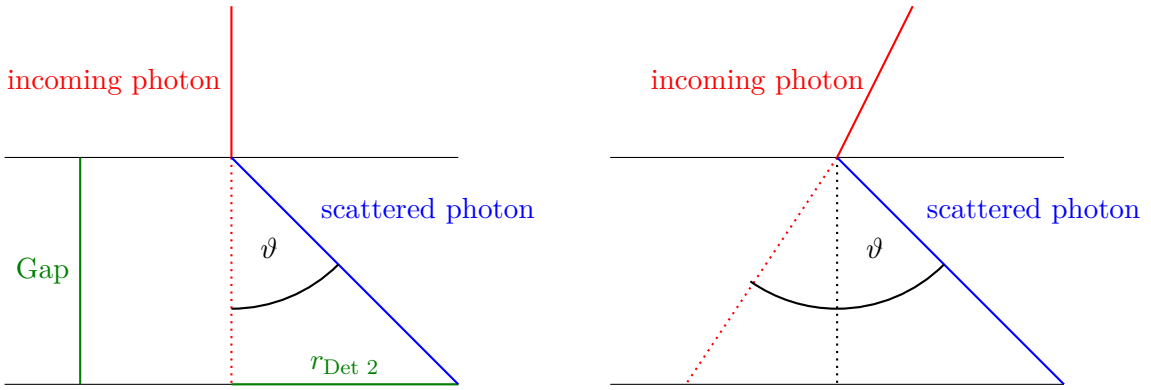

(a) Photon coming from a direction perpendicular to the plane

(b) Photon coming from a direction tilted to the axis perpendicular to the detector plane

Figure 5.6 Visualisation of the maximal scattering angle which can appear during a scattering in the first detector so that the second detector is still reached by the photon. For a non-perpendicular incidence the maximal scattering angle is larger by the incidence angle.

Thereby, E' is the photon energy after the Compton scattering which corresponds to the energy deposited in the second detector and E is the total energy before the scattering which is the sum of the energies deposited in both detectors assuming that the photon was completely absorbed in the second detector. The false events described above often deposit larger amounts of energy in the first detector leading to a large photon scattering angles. So the method of the maximal scattering angle is an effective background rejection.

For all events that are classified as true or partial events, Compton cones can be calculated. From geometrical calculations the outlines and positions of the event ellipses can be calculated. The detailed calculations are given in Appendix 2.1.
For the calculation of the event ellipses the coordinate system is transformed into a new system which has a z-axis in the direction of the axis of symmetry of the Compton cone. For this purpose, in a first step the coordinate system is translated from the origin to the interaction point in the first detector and then rotated around an axis. This axis is normal to the plane that contains the connection vector of the two interaction points and the original z-axis. The new coordinate system can be found via

$$\vec{r}_{\text{b}} = \begin{pmatrix} (x-x_1)[n_1^2(1-\cos(\beta))+\cos(\beta)] + (y-y_1)n_1n_2(1-\cos(\beta)) + (z-z_1)n_2\sin(\beta) \\ (x-x_1)n_2n_1(1-\cos(\beta)) + (y-y_1)[n_2^2(1-\cos(\beta))+\cos(\beta)] - (z-z_1)n_1\sin(\beta) \\ -(x-x_1)n_2\sin(\beta) + (y-y_1)n_1\sin(\beta) + (z-z_1)\cos(\beta) \end{pmatrix}, \tag{5.8}$$

where i_1 are the coordinates of the interaction point of the upper detector with i=x,y,z and n_i the coordinates of the rotation axis with i =1,2,3. The angles in this formula are the opening angle α of the cone and the tilting angle β with respect to the z-axis.
In this new system the intersection line of the cone with the source plane is circular. By setting z equal to the distance of the source and inserting the new coordinates in the circle formula

$$x_{\text{b}}^2 + y_{\text{b}}^2 - z_{\text{b}}^2\tan(\alpha) = 0 \tag{5.9}$$

a formula for the intersection ellipses can be obtained.

To visualise the results of the reconstruction, all event ellipses are plotted on the pixelated plane S. The accuracy of the reconstruction depends strongly on the size chosen for these pixels. For the pixelated plane, a certain field-of-view is chosen. The minimal and maximal x-position on this plane is calculated from the simple tangent relation of distance of the plane and the field-of-view angle in the negative as well as in the positive direction. The same is done for the y direction. The resulting quadratic field is then divided in a number of pixel depending on a chosen resolution which are used as pixel coordinates for the next step.

For every event the pixels crossed by the corresponding ellipse line are stored in a so called *hitlist*. For minimizing the time needed to calculate the points on the ellipses a special algorithm is used. For this, one starting point on the ellipses has to be known. To find this point, for one row of the plane, the coordinates describing each pixel are inserted in the ellipse formula 5.9. Points on the ellipse generate smaller absolute values when put into the ellipse equation than pixels containing no part of the ellipse (in an ideal case of infinitesimal pixels points on the ellipse would produce a value of zero). The pixel with the minimal result when inserted into the formula is assumed to be nearest to the real ellipse.
The same process is then repeated for the column containing the minimum pixel of the first interaction. The minimal value of this second calculation is assumed to be a point lying on the ellipse.

For the thus found starting point the four non-diagonal neighbouring pixels are analysed (see Figure 5.7). The outline of the ellipse has to cross two of these pixels, one for entering the chosen pixel and one for leaving it. Thus, the pixel with the smallest absolute value when inserted in the ellipse equation is then stored in the hit list. For this point the procedure is repeated. If the found minimal pixel is already in the hit-list, the next larger value is taken. If this value is also already in the list, the ellipse is assumed to be found as a whole.

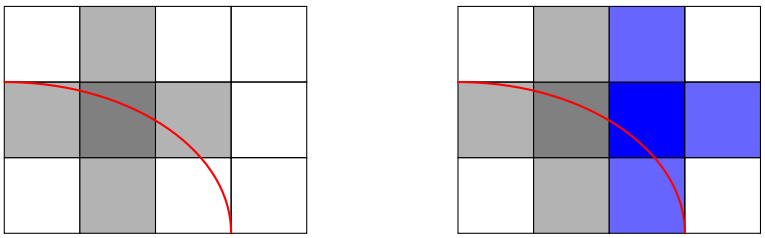

Figure 5.7 Algorithm to draw an ellipse on a pixelated plane. One the left, the dark-grey pixel is assumed to be known to contain a part of the ellipse line at the beginning of the algorithm. The four adjacent pixel are analysed next. At least two of them have to be traversed by the ellipse to enter and leave the starting pixel. One of those is chosen for the next iteration. In the figure, the pixel on the right is chosen (dark-blue on the right side). Again, the four neighbouring pixel are analysed. The dark-gray pixel on the left of the new starting pixel is already in the hit list classified as a pixel containing a part of the ellipse. It is therefore neglected. The next pixel chosen as a starting pixel would then be the light-blue pixel below the current starting pixel.

If the algorithm reaches an edge of the field of view, the procedure starts again with the first value of the hit list. Because the first minimum is already in the hit list, the algorithm follows the ellipses to the other direction till reaching an edge again. Then the algorithm is stopped. This way, all ellipses inside the plane area can be found.

The hit-list entries are then converted into angular units using the tangent. From the generated hit list a two-dimensional histogram is produced, indicating the number of event circles

passing through a certain pixel. The intersection point of all ellipses is the maximum of the histogram. By using a Gaussian approximation, the row and column containing the maximum value are fitted to determine the mean value and the standard derivation of the maximum.

5.4 Results of the Compton camera simulation

The results of the Compton camera simulation encompass the calculation of the maximal scattering angle for the background reduction, an analysis of the quantum efficiency of different material configurations as well as the reconstruction of positions for several point sources. The evaluation is done for the exemplary setup described above with a monoenergetic point source emitting photons with 100 keV.

5.4.1 Maximal scattering angle for background suppression

For the detector geometry simulated exemplary in this section, the maximal scattering angle is $\vartheta = 75.96°$ for a perpendicular beam. The limitation of the field-of-view for the detector of 17.6°is chosen which corresponds to a shift of the source in the x- and y-direction of 30 cm leading to a maximum scattering angle of $\vartheta = 92.66°$.
For the setup considered in this work, an input energy of E =100 keV is used. According to Equation 5.7, the maximal energy that can be deposited by the photons in the first detector is

$$E^{\max}_{\text{Det,up}} = E - E' = \begin{cases} 11.00[\text{keV}] & \text{for } \vartheta = 75.96 \\ 14.76[\text{keV}] & \text{for } \vartheta = 92.66. \end{cases} \tag{5.10}$$

Thus, the energy deposited in the first detector has to be smaller than $E^{\max}_{\text{Det,low}}$ for the scattered photon to reach the second detector. For further calculations the smaller value for ϑ was used. By doing this, few valid events with large scattering angles were rejected but more of non-valid events can be suppressed.

5.4.2 Quantum efficiency of certain material configurations

Depending on the material and the thickness of the detectors as well as on the considered energy range, the quantum efficiency of the Compton camera configuration varies. The quantum efficiency of a Compton camera in this work is considered as the number of events that trigger events in both detectors to the number of incident photons. It is not further subdivided into true, part and false events. In Table 5.1 the efficiencies of several configurations of materials are given for an input energy of 100 keV.
Because the quantum efficiency of material configurations including silicon in this energy range with the considered thickness are very low in comparison to the other configurations they are not further considered. The results for the quantum efficiency are also shown graphically in the Figures 5.8(a) and 5.8(b). It can be seen that the yield of detected events increases up to a thickness of 3 mm for the first detector and decreases for greater thicknesses. In contrast the thickness of the second detector does not have much influence as long as it is greater than 1 cm. The variances are thought to be statistical fluctuations.
Even if the number of true events increases with increasing layer thickness, the best yield of detected events is found with a combination of two detectors made of germanium with a thickness of 3 mm and 2.5 cm respectively. As a result, this combination was used for the following evaluation.

Table 5.1 Quantum efficiency at 100 keV of the Compton camera for various configurations of material. The thicknesses stated in square brackets behind the detector materials are given in mm. The table shows the mean value of 11 measurements between 0° and 6° of photon incidence angle. Hereby detected events are events with deposited energy in both detectors and are given in percent of the generated photons. True events are the part of detected events with full energy absorption whereas for partial events the detected energy is smaller than the generated input energy. False events are backscatter or electron production events which are not used for further calculations. For each measurement 100,000 photons are simulated.

Detector 1	Detector 2	detected [10^{-3}%]	true [%]	partial [%]	false [%]
Si[0.450]	Si [0.450]	59.55	10.68	9.15	80.15
Si[0.450]	Ge [10.00]	859.73	79.82	1.89	18.28
Si [1.00]	Ge [10.00]	1767.91	81.79	1.79	16.41
Ge [1.00]	Ge [10.00]	3155.00	63.24	0.72	36.04
Ge [2.00]	Ge [10.00]	4044.82	69.01	0.35	30.63
Ge [3.00]	Ge [10.00]	4065.91	72.49	0.23	27.28
Ge [4.00]	Ge [10.00]	3799.18	74.78	0.17	25.04
Ge [5.00]	Ge [10.00]	3325.27	77.10	0.15	22.75
Ge [6.00]	Ge [10.00]	2866.55	78.41	0.10	21.48
Ge [7.00]	Ge [10.00]	2402.00	79.67	0.12	20.21
Ge [8.00]	Ge [10.00]	1986.64	81.43	0.06	18.48
Ge [9.00]	Ge [10.00]	1622.82	82.13	0.12	17.75
Ge [10.00]	Ge [10.00]	1333.82	82.59	0.10	17.31
Ge [3.00]	Ge[10.00]	4065.91	72.49	0.23	27.28
Ge [3.00]	Ge[15.00]	4148.64	73.27	0.22	26.51
Ge [3.00]	Ge[20.00]	4162.09	73.37	0.22	26.42
Ge [3.00]	Ge[25.00]	4164.09	73.37	0.21	26.41
Ge [3.00]	Ge[30.00]	4160.55	73.39	0.21	26.40

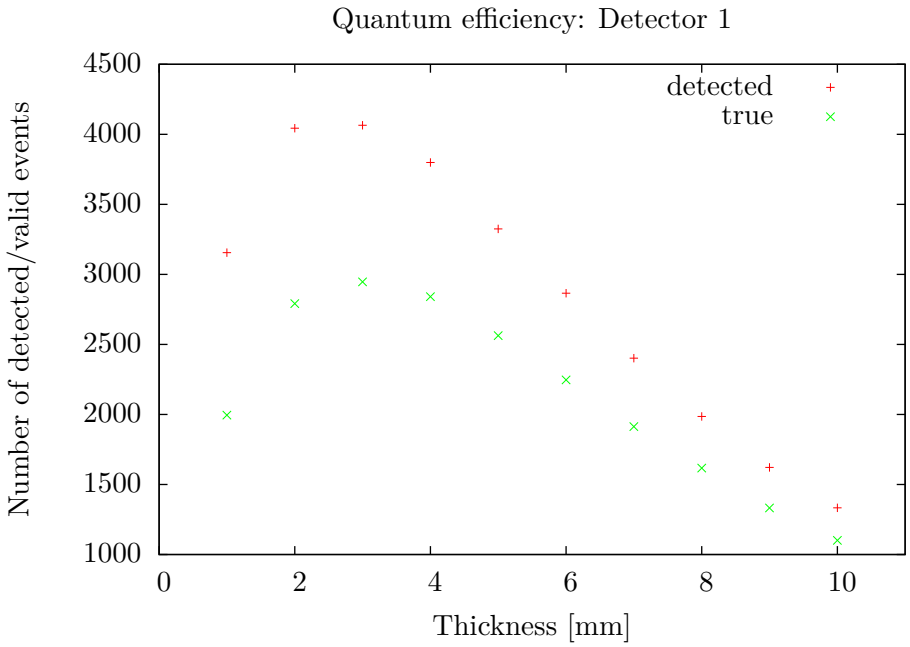

(a) Yield of valid events as function of the thickness of the first detector. The second detector has a thickness of 1 cm.

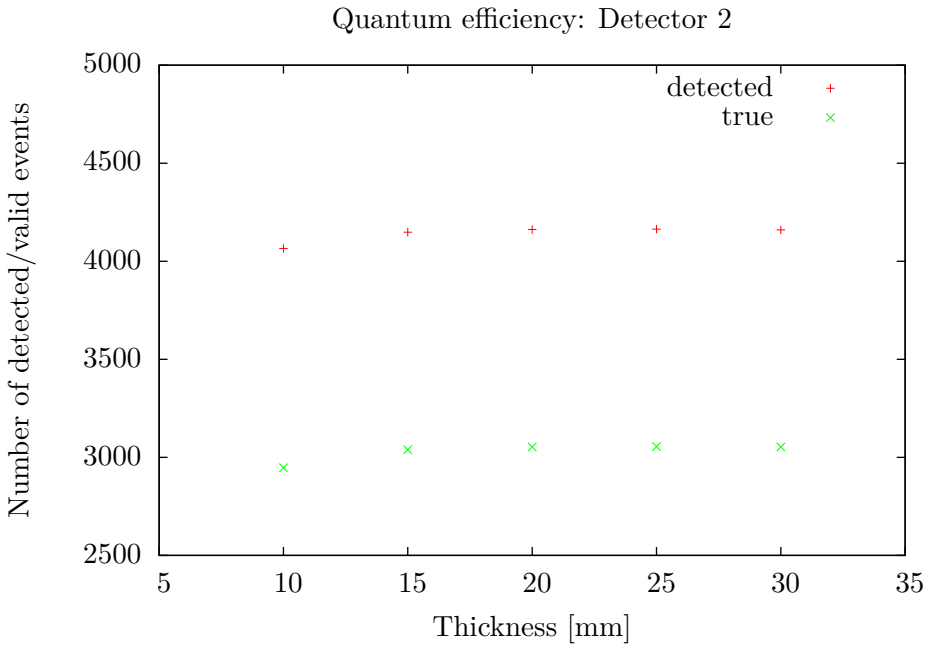

(b) Yield of valid events as a function of the thickness of the second detector. The first detector has a thickness of 3 mm.

Figure 5.8 Analysis of the amount of events as a function of the thickness of the two germanium detectors. Here, the red dots correspond to detected events which means events with energy deposition in both detectors. The green dots are events that were classified as true events which is the part of detected events in which the photon triggers an event in the first detector and is thereafter stopped completely in the second one.

5.4.3 Reconstruction of the source position

In Figure 5.10 two examples of a histogram together with the corresponding curve fits in x and y direction are displayed. A field-of-view of $\frac{\vartheta}{2} = 80°$ is chosen together with a resolution of 10 mm corresponding to an angular resolution of about 0.3°. A finer binning would need a much longer evaluation time because of the algorithm time that is still high.

The deviation of the reconstructed to the true positions of the simulation are shown in Figure 5.9. It can be seen that the reconstructed positions coincide with the true positions in accordance with the accuracy of the reconstruction method. Still, there seems to be a systematic error because the deviations increase for increasing y-position. This can be fitted with a linear fit described by

$$y(x) = 0.0342963 \cdot x + 0.0859156. \tag{5.11}$$

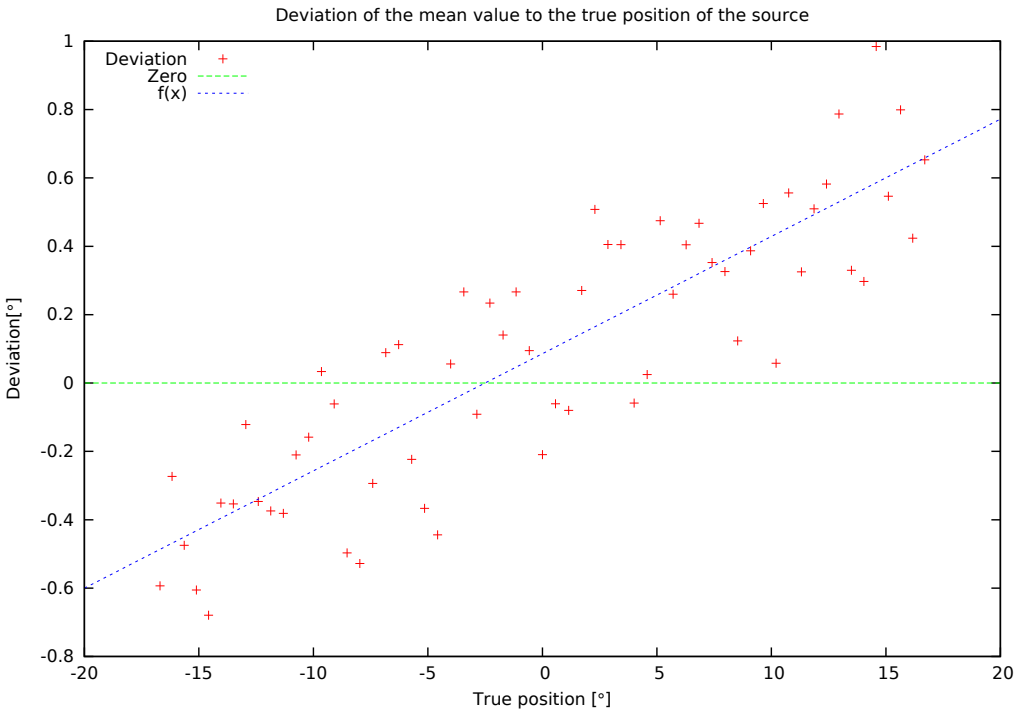

Figure 5.9 The reconstructed source position for simulated positions between −17° and 17° in y direction. The red crosses show the difference between the true position and the reconstructed position while the green line is the zero position. The increasing of the deviations at increasing y position can be fitted with a linear fit (blue).

The linearity of the deviation suggests an error in the reconstruction process that is not statistical. Some mayor effect seems to be missing in the description. An influence of the chosen binning is assumed but could not be tested in the in the time available.
The Appendix 2 lists the true and reconstructed positions together with the standard deviations.

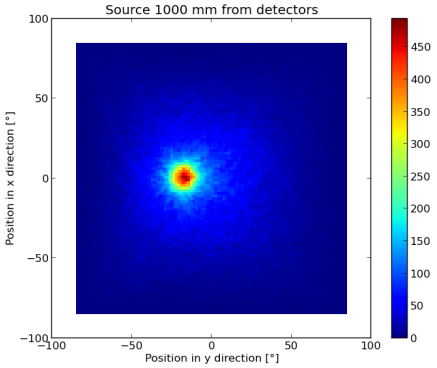

(a) Histogram for a simulated source with the true position (0°,−17°)

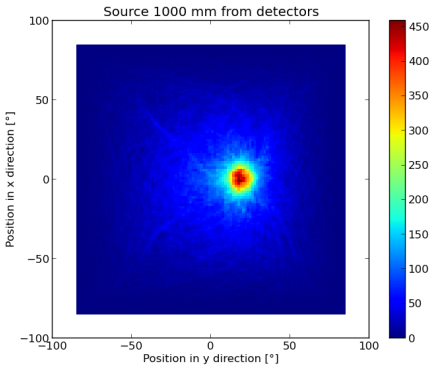

(b) Histogram for a simulated source with the true position (0°,+17°)

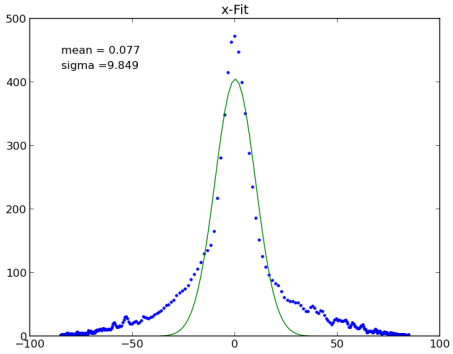

(c) Fit for the column including the maximum

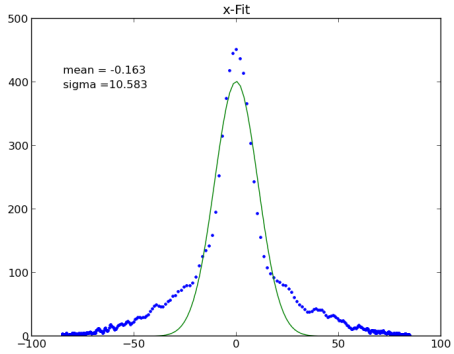

(d) Fit for the column including the maximum

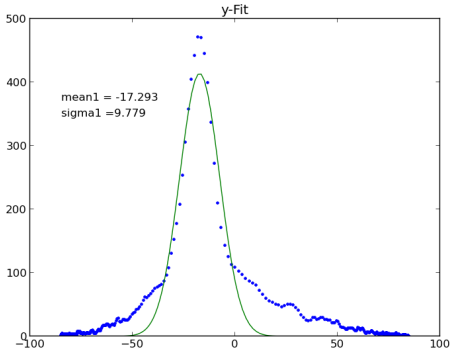

(e) Fit for the row including the maximum

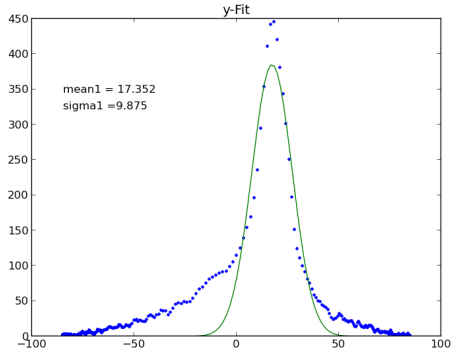

(f) Fit for the row including the maximum

Figure 5.10 Reconstruction of the source position with a true position at (0°, ±17°). Both are in units of degree. In the figures (c) to (f) a moving average of three neighbouring values is used for the measured date (blue). Mean value and standard deviation (sigma) for the fitted curves (green) were named.

5.5 Simulation of a 3-Layer setup

As it was shown before, the quantum efficiency depends strongly on the considered photon energy. In the detector setup used in the previous section, at 100 keV only 0.21 % are partial events, at 250 keV there are already 9.94 % (the maximal energy for the upper detector here is 75.54 keV calculated via Equation 5.7). Those partial events lead to an error in the calculation of the opening angle and therefore to an error in the position reconstruction. To get a better resolution for higher energies, it is therefore useful to include additional detector layers to the geometry in order to improve the possibility of absorption and therefore the accuracy of the position reconstruction. A further exemplary simulation is performed in this section to show the differences in the reconstruction process for additional detector layers.

To analyse the behaviour of this setup, a simulation was run, including the detectors described above together with an additional germanium detector in between. The distance between each detector is again 10 mm. Several thicknesses of the new detector are tested. The results of a quantum efficiency measurement are provided in Table 5.2.

Table 5.2 Statistical analysis for the Compton camera with three detector layers. In the presented analysis, detected events are events with deposited energy in the highest detector and at least in one of the other two detectors. It is given in percent of the generated photons. True events are the part of detected events with full energy absorption whereas for partial events the detected energy is smaller than the generated input energy. False events are backscatter or electron production events which were not used for further calculations. Again, for the measurement 100,000 photons with an input energy of 250 keV are simulated for each configuration.

thickness d_2 [mm]	detected [10^{-3}%]	full [%]	partial [%]	false [%]
00	5740	41.39	9.94	48.66
01	4057	81.41	2.26	16.32
02	4152	76.76	2.82	20.42
03	4354	71.06	4.02	24.92
04	4444	68.34	4.05	27.61
05	4539	64.77	4.98	30.25
06	4776	62.31	5.59	32.10
07	4912	59.89	5.44	34.67
08	5013	57.39	5.98	36.62
09	4979	55.29	6.32	38.38
10	5109	52.91	7.12	39.97
25	5740	41.39	9.94	48.66

By adding another detector layer with a thickness of 1 mm the amount of partly absorbed photons is reduced. However, with increasing layer thickness also the amount of partly and false events increases again. Even if the percentage of detected events rises, the higher probability of fully detected events with an additional layer of only 1 mm is favoured for an input energy of 250 keV.

A new algorithm for the source position reconstruction differs from the previous one only in the definition of the value E' of the photon after the scattering which is described as the sum of the energies deposited in the second and the third detector.

The additional interaction point in the second detector can be used for the verification that the photon was truly scattered due to the Compton effect. Both the deposited energy as well as the source position for this second scattering are known. This is done for instance for further false event reduction by S. Tashenov (2010).

5.6 Astronomical Compton telescope

An astronomical source emits photons that enter the Compton telescope in parallel beams. That means that photons hitting the first detector at different positions but under the same angle originate still from the same source (see Figure 5.11). Furthermore, the reconstruction of the source position should not depend on the knowledge of the source distance. Therefore an adapted reconstruction algorithm is needed.

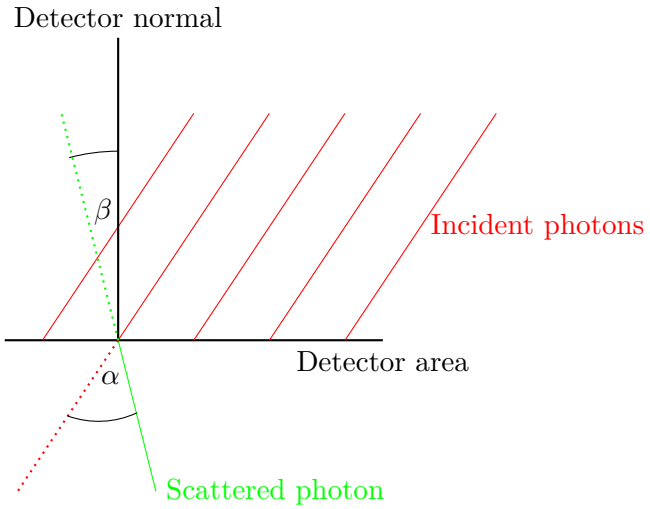

Figure 5.11 Incident photons in an astronomical Compton telescope. In the astronomical case the photon incident in parallel beams. The scattering angle which is equal to the opening angle of the corresponding Compton cone is α while β describes the tilting of the cone.

For the astronomical case, the reconstruction process is indeed simpler than the reconstruction of near source positions in the sense that no elliptic approach is needed. From the algorithm used in the previous sections, the calculation of the opening angle α of the Compton cone as well as the one for the tilting angle β are known. In the new process, instead of the source position, the direction to the source is determined. On a pixelated plane in angular units, circles can be drawn with the tilting angle β as central position and the opening angle α as radius. For this purpose the angle β has to be decomposed in an angle in x-direction and an angle in y-direction. An algorithm is needed to test pixel on a plane to solve the circle equation for the found radius and central position. For many photons those circles should then again intersect in one point, stating the direction to the astronomical source. The drawing algorithm corresponds to the one from the previous sections.

6 CANDELA: Compton telescope simulation

The techniques found in the previous chapter are now applied in an actual experimental setup. Therefore, the data from the stacked detector setup CANDELA[1] are taken. This setup consists of a low energy detector made of 450 µm silicon and a high energy detector made of 1.0 mm cadmium telluride. CANDELA was originally used for the testing and calibration of SIMBOL-X detectors, but is now utilised as a Compton polarimeter (Maier, 2014).

The SIMBOL-X mission was a collaboration between French, Italian and German institutes. The instrument was planned to operate in an energy range from 0.5 keV to 80 keV. In this energy range, focusing is difficult and large focal lengths are needed. Since the length of a spacecraft is limited, the SIMBOL-X collaboration proposed a combination of two spacecrafts, one carrying the mirrors, the other one carrying the collimator and the detector itself. This way, a focal length of about 20 m could be reached which enables a focusing hard X-ray optics with an angular resolution of 20 ". The mission was planned to be launched in 2014 but was cancelled in 2009 because of financial problems (Gouiffès et al., 2008; CNES, 2011).

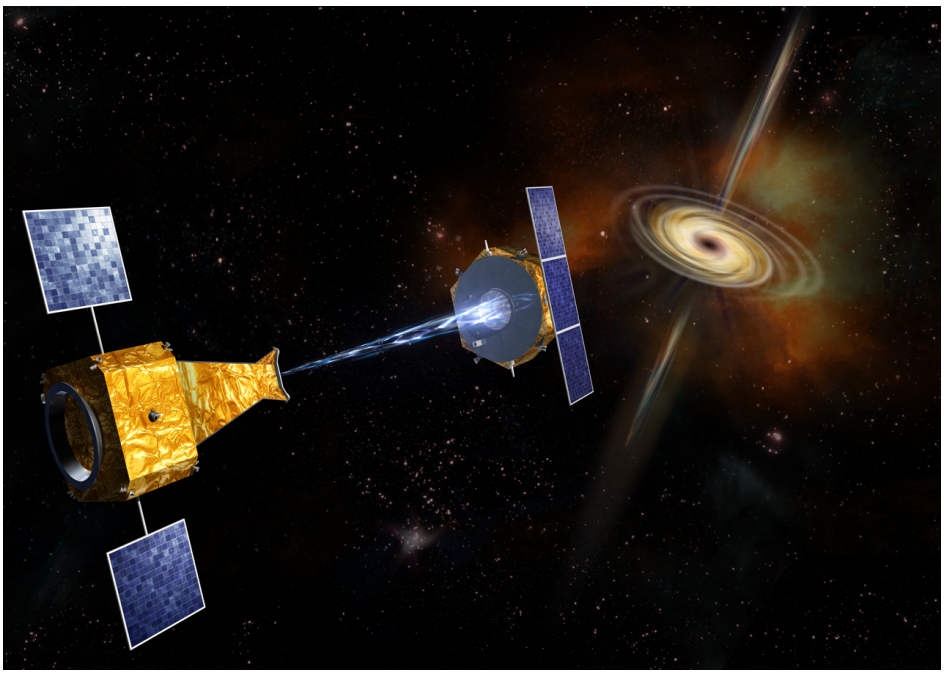

Figure 6.1 Image of the SIMBOL-X telescope from CNES (Oliver Sattler)

[1]CANDELA: Cadmium And silicoN DEtector LAborarory

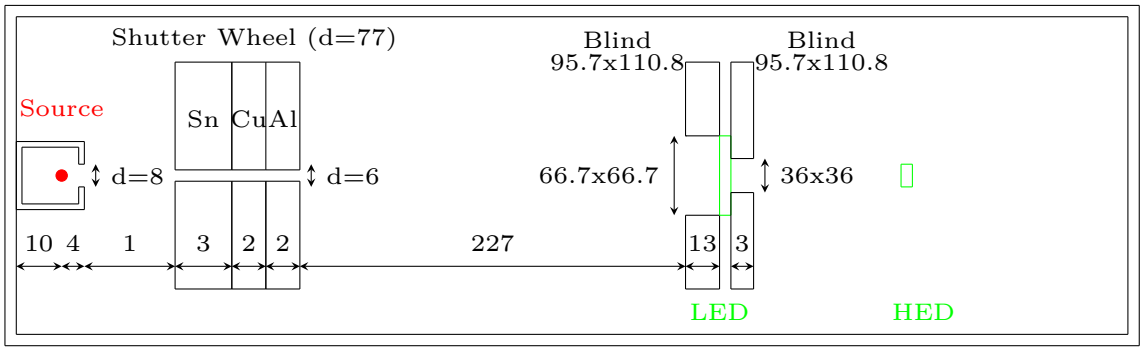

Figure 6.2 Schematic drawing of the CANDELA setup. All values are in units of mm. The detectors have a size of 32x32x0.450 mm^3 (LED) and 10x10x1 mm^3 (HED). The shielding around the source is made of tin, the blinds are made of copper. The setup is positioned inside a tube with a total length of 388 mm and a diameter of 290 mm made of stainless steel V2A. The drawing is not to scale.

6.1 Simulation of the CANDELA setup

The stacked detectors of CANDELA can be operated as a Compton telescope. The geometry is placed inside an evacuated tube made of stainless steel. At one side of the tube, the source is positioned inside an aluminium shielding box which the photons can only leave through an entrance window. In front of this entrance window is a shutter wheel made of one layer of tin, one of copper and one of aluminium. In the CANDELA setup it is possible to choose between an Am-241 or an Fe-55 source by rotating the filter wheel or to close the entrance window when doing dark measurements for background calibration. In the simulation the wheel is in an open position for the americium source.

Two detectors are positioned at the far side of the tube, one made of silicon (LED[2]), the other one made of cadmium telluride (HED[3]). The LED is closer to the source and shielded with a copper cover at the front and a copper blind at the backside both leaving an entrance window for the incoming photons. Both detectors are quadratic with an edge length of 3.2 cm and a thickness of 450 µm for the LED and an edge length of 1.0 cm and a thickness of 1.0 mm for the HED, respectively. The distance between the two detectors amounts to 1.0 cm.
The setup geometry used for this simulation with sizes for the additional shieldings and blinds can be found in Figure 6.2.

In this setup, a source of the radioactive material ^{241}Americium is used. The emission lines of Am-241 that are used in the simulation are listed with their energies and their intensities in Table 6.1.

The source has a total intensity of 81,4 µCu. This correspond to a rate of $3.01 \cdot 10^6$ decays per second. The source is simulated as a *General Particle Source* (see Section 2.2.2.3). For every energy line a point source with the intensity stated in Table 6.1 is generated from which photons are randomly chosen in each event. This produces the lines spectrum given in Figure 6.3.

In order to produce detector spectra comparable to the CANDELA experiment, a 60 minutes measurement is simulated. Because Geant4 simulates only one photon per event, an isotropic

[2]LED: Low Energy Detector
[3]HED: High Energy Detector

Table 6.1 Energy lines of the input spectrum produced by the americium source taken from (Firestone and Ekström, 2008)

Energy [keV]	Intensity [%]	Origin
11.87	0.66	Np-L_l
13.76	1.07	Np-$L_{\alpha 2}$
13.95	9.60	Np-$L_{\alpha 1}$
15.86	0.15	Np-L_{η}
16.11	0.18	Np-$L_{\beta 6}$
16.82	2.50	Np-$L_{\beta 2}$
17.06	1.50	Np-$L_{\beta 4}$
17.51	0.65	Np-$L_{\beta 5}$
17.75	5.70	Np-$L_{\beta 1}$
17.99	1.37	Np-$L_{\beta 3}$
20.78	1.39	Np-$L_{\gamma 1}$
21.10	0.65	Np-$L_{\gamma 2}$
21.34	0.59	Np-$L_{\gamma 3}$
21.49	0.29	Np-$L_{\gamma 6}$
26.35	2.40	Am-241
33.20	0.13	Am-241
59.54	35.9	Am-241

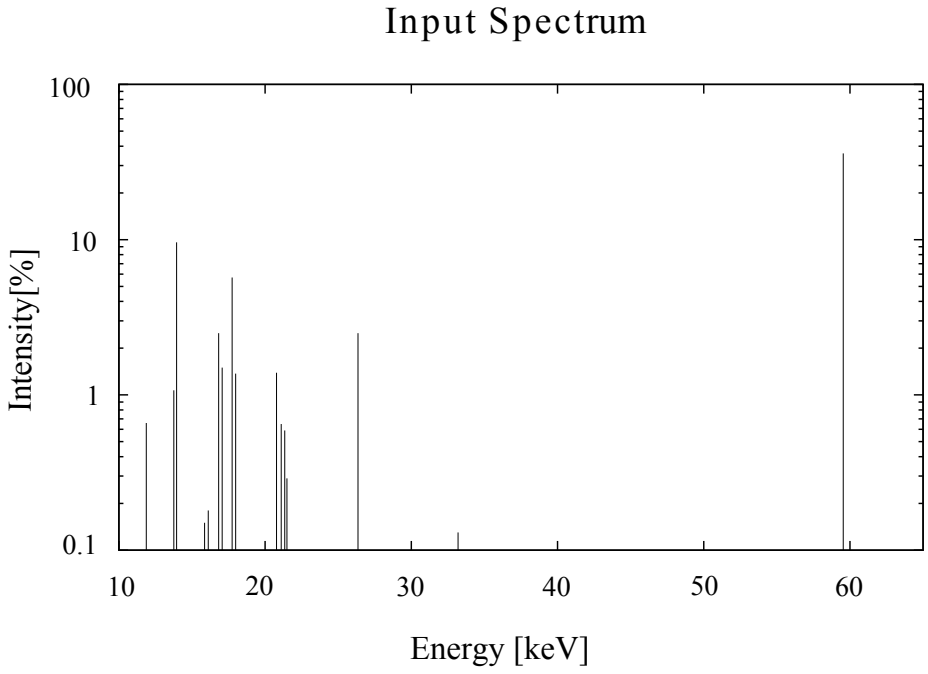

Figure 6.3 Input spectrum for the CANDELA simulation

radiating source would produce $10.836 \cdot 10^9$ events during this simulation. To reduce the simulation time, instead of such an isotropic angular distribution, an emission cone with an opening angle of $\vartheta = 100°$ is chosen. This opening angle guarantees an emission cone just large enough to enable the photons to leave the shielding around the source through the entrance window.
To calculate the number of events needed in this configuration, for an unlimited isotropic emission a sphere around the source with a radius r is assumed (see Figure 6.4).

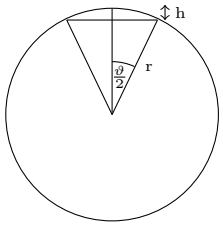

Figure 6.4 Two dimensional description of a sphere with radius r and a segment of the sphere with an opening angle ϑ and a height difference h.

The volume of this sphere is given via

$$V_{\text{Sphere}} = \frac{4}{3}\pi r^3. \tag{6.1}$$

The limited emission is defined as a segment of a sphere with the same radius r and a height difference h between the radius and the cone height. It can be calculated with the formula

$$V_{\text{Segment}} = \frac{2}{3}\pi r^2 h. \tag{6.2}$$

The ratio of the two volumes corresponds to the ratio of the limited to the unlimited photon emission. Therefore the number of simulated photons is

$$N_{\text{limited}} = \frac{V_{\text{Segment}}}{V_{\text{Sphere}}} N_{\text{unlimited}} = \frac{h}{2r} N_{\text{unlimited}}. \tag{6.3}$$

Furthermore it is

$$\cos\left(\frac{\vartheta}{2}\right) = \frac{r-h}{r} \tag{6.4}$$

$$\Rightarrow \frac{h}{r} = 1 - \cos\left(\frac{\vartheta}{2}\right). \tag{6.5}$$

The number of particles that should be simulated is

$$N_{\text{limited}} = \frac{1}{2}\left(1 - \cos\left(\frac{\vartheta}{2}\right)\right) N_{\text{unlimited}} \tag{6.6}$$

$$N_{\text{limited}} = 0.15 \cdot N_{\text{unlimited}} = 15.86 \cdot 10^8. \tag{6.7}$$

For the simulation $16 \cdot 10^8$ photons are generated which corresponds to a simulated time of 3543.74 s. It should be noted that the number of events in one run is limited by the size of a signed 32-bit integer which is 2,147,483,647. For a larger number of events a second run has to be performed and the resulting data should be assembled at the end. It is important to change the seed for the generation of random numbers in every run to avoid the reproduction of the same dataset.

The simulation is performed with Geant4 9.6.2. For the study of the fluorescence background a slightly different Physics List is used. In particular, the PIXE[4] Livermore model is applied that simulates interactions with electrons of the inner shells of atoms. Those interactions lead to the creation of the fluorescence photons that will be studied in the next section. Also, for the photoelectric effect, fluorescence is activated.

6.2 Output and evaluation of the data

In a laboratory experiment, the line energies of the source measured by the detector would be Gaussian shaped due to finite energy resolution of the detectors. Because the simulation is an idealised calculation, the energy deposited in the detectors would generate a spectrum with lines whose linewidth depends only on the bin size of the spectrum. For the comparison with the CANDELA measurement, the effect of a certain line broadening has to be taken into account.

A normal Gaussian distribution around an energy value x can be generated via

$$g(x) = \frac{1}{\sqrt{2\pi\sigma^2}} \mathrm{e}^{-\frac{x^2}{2\sigma^2}} \tag{6.8}$$

where σ^2 is the variance of the distribution.
To assign this distribution for every energy detected in the LED and the HED, every energy has to be weighted depending on this distribution. This weight is calculated by the inverse cumulative distribution function (CDF) of the Gaussian distribution. The CDF gives the probability for a certain value to be smaller than the argument of the CDF. It is calculated as the integral over the distribution from $-\infty$ to the argument x.

$$\begin{aligned} G(x) &= \int_{-\infty}^{x} \mathrm{g}(x')\mathrm{d}x' && (6.9)\\ &= \int_{-\infty}^{0} \mathrm{g}(x')dx' + \int_{0}^{x} \mathrm{g}(x')\mathrm{d}x' && (6.10)\\ &= \frac{1}{2} + \int_{0}^{x} \frac{1}{\sqrt{2\pi\sigma^2}} \mathrm{e}^{-\frac{x'^2}{2\sigma^2}} \mathrm{d}x' && (6.11) \end{aligned}$$

Because of the symmetry of the Gaussian distribution and its normalisation, the first integral can be evaluated to $\frac{1}{2}$. For solving the second integral a substitution is needed. Hereby, it is assumed that

$$t^2 = \frac{x'^2}{2\sigma^2} \rightarrow \mathrm{d}x' = \sqrt{2\sigma^2}\mathrm{d}t. \tag{6.12}$$

With this substitution the CDF can be solved in the following way.

$$\begin{aligned} G(x) &= \frac{1}{2} + \int_{0}^{\frac{x}{\sqrt{2\sigma^2}}} \frac{1}{\sqrt{2\pi\sigma^2}} \mathrm{e}^{-\frac{x'^2}{2\sigma^2}} \sqrt{2\sigma^2}\mathrm{d}t && (6.13)\\ &= \frac{1}{2} + \frac{1}{\sqrt{\pi}} \int_{0}^{\frac{x}{\sqrt{2\sigma^2}}} e^{-t^2}\mathrm{d}t && (6.14) \end{aligned}$$

The remaining integral can be substituted with the *error function*.

$$\mathrm{erf}(x) = \int_{0}^{x} \frac{2}{\sqrt{\pi}} \mathrm{e}^{-t^2}\mathrm{d}t, \tag{6.15}$$

[4]PIXE: Particle-Induced X-ray emission

so that the total CDF is found to be

$$G(x) = \frac{1}{2} + \frac{1}{2}\mathrm{erf}\left(\frac{x}{\sqrt{2\sigma^2}}\right). \tag{6.16}$$

The inverse of this CDF is

$$\mathrm{G}^{-1} = \sqrt{2}\sigma\mathrm{erf}^{-1}(2x-1) \tag{6.17}$$

with the inverse error function that can be calculated via the Maclaurin series

$$\mathrm{erf}^{-1}(x) = \sum_{k=0}^{\inf} \frac{c_k}{2k+1}\left(\frac{\sqrt{\pi}}{2}x\right) \tag{6.18}$$

with

$$c_0 = 1 \tag{6.19}$$

$$c_k = \sum_{m=0}^{k-1} \frac{c_m c_{k-1-m}}{(m+1)(2m+1)}. \tag{6.20}$$

For the distribution the values x are chosen randomly between 0 and 1. A Gaussian distribution together with the CDF and the inverse CDF are shown for a normal distribution in Figure 6.5.

The inverse CDF depends on the variance of the distribution. This variance can be calculated for every energy line via

$$\sigma^2(E) = \mathrm{F}\Delta\mathrm{E}E. \tag{6.21}$$

The factor F is called *Fano Factor* and is a correction factor for the number of electron-hole pairs produced in a material due to the Poisson distribution. It is F = 0.115 for Silicon and F = 0.15 for Cadmium.
The energy ΔE in this formula is a material dependent constant stating the average energy necessary to create an electron-hole pair. For Silicon a value of $\Delta\mathrm{E} = 3.6\,\mathrm{eV}$ is assumed, for Cadmium $\Delta\mathrm{E} = 4.43\,\mathrm{eV}$ (Spieler, 2006; Lutz, 2001; Takahashi et al., 2002).

The structure of the output files corresponds to the structures used in the previous chapter. A table with 13 columns is produced stating the two time stamps of the first interaction of a photon for both detectors, two values for the deposited energies, the two interaction positions, the number of steps processed in each detector volume as well as the generated input energy.

The data is evaluated with the two Python programs used in the previous chapters. For the reconstruction of the source position *compton_main* is used while the energy spectra are generated by *histo_main*.

6.3 Results of the CANDELA simulation

The results of the simulation are discussed in detail in this section. This includes the reconstruction of the source position as well as a study concerning the fluorescence background produced by the irradiated surrounding elements of the setup.

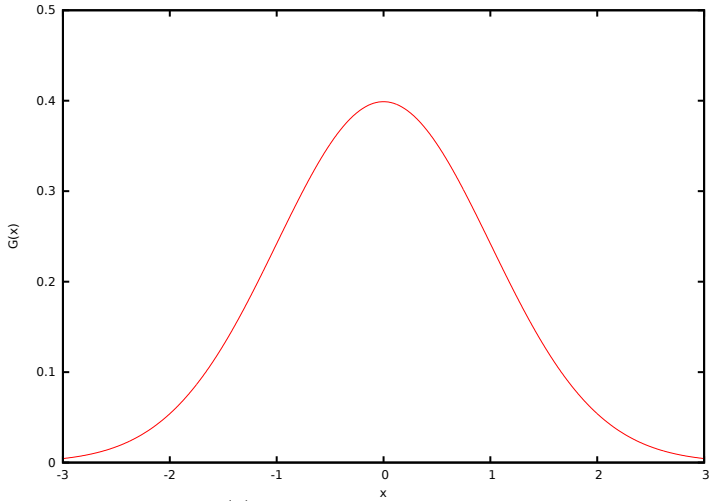

(a) Gaussian distribution

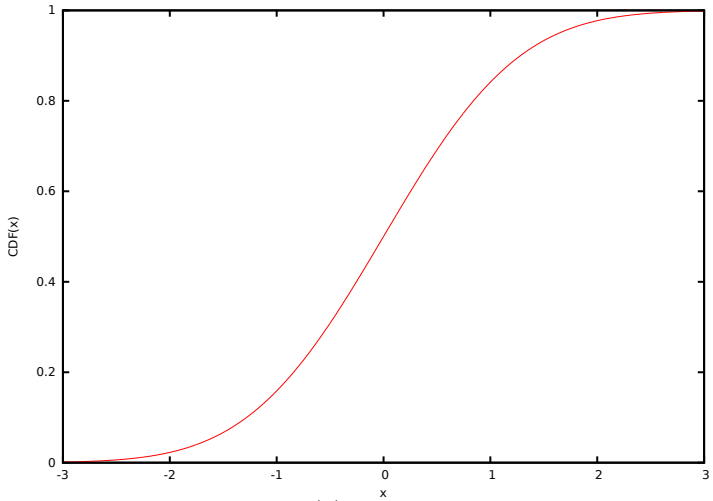

(b) CDF

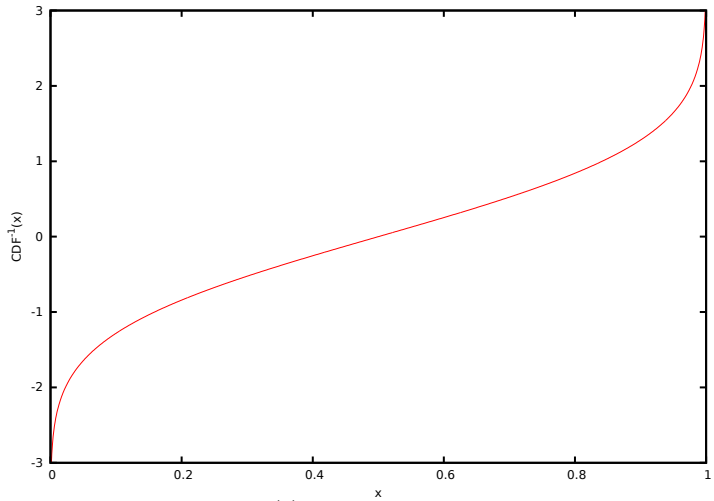

(c) Inverse CDF

Figure 6.5 Gaussian, its cumulative distribution and its inverse cumulative distribution function. The curves are shown for a normal distribution with the mean value $\mu = 0$ and the standard deviation $\sigma = 1$.

6.3.1 Reconstruction of the source position

As in the previous chapter one goal of the simulation is the determination of the source position in the setup. The maximal scattering angle for this geometry is calculated to $\vartheta = 29.52$, so the energy threshold is $E_{\max} = 0.723\,\mathrm{keV}$. This is a lower limit because due to the widening of the emission cone most photons do not enter the detector plane in a perpendicular beam. This effect is enlarged by the short distance to the source.
Table 6.2 shows the results of the statistical analysis of the measurement. For the analysis a maximum line width of $\sigma = 0.2\,\mathrm{keV}$ is assumed. Deposited energies that differ from the input energy by less than the half line width are still considered to be fully detected. From the generated photons only a fraction of $1.1 \cdot 10^{-5}$ triggers events in both detectors. From those 9.33 % are fully detected. The low amount of true events is assumed to be due to the low energy threshold by the maximal scattering angle as well as due to fluorescence effects which increase the number of partial and false events. Still there are enough events for a proper source reconstruction.

Table 6.2 Statistical analysis for the CANDELA setup. Because of shieldings and blinds, only part of the generated photons reaches one or both of the detectors. Only photons that trigger an event in both detectors can be used for the reconstruction of the source position. From these photons only those with full or at least partial energy deposition are valid. Backscattering or electron production events were neglected. The number of photons generating events in the LED and HED are given in percentage of the generated events. Full, partial and false events are given in percentage of events depositing energy in both detectors.

Events						
generated	in LED [%]	in HED [%]	in both [%]	full [%]	partial [%]	false [%]
$1.6 \cdot 10^9$	0.2	0.05	$1.1 \cdot 10^{-3}$	9.34	2.59	88.18

The results of the reconstruction are shown in Figure 6.6. It can be noted that the true source position at the centre of the setup lies well inside the σ ranges. From the standard deviation σ the full width half maximum (FWHM) can be calculated.

$$\mathrm{FWHM} = 2\sqrt{2\ln 2} \cdot \sigma \tag{6.22}$$

The FWHM for the Compton telescope application of the CANDELA setup is

$$\mathrm{FWHM} = \begin{cases} 14.51 & \text{for the x direction} \\ 15.62 & \text{for the y direction.} \end{cases} \tag{6.23}$$

Because of a higher fraction of partially absorbed photons the uncertainties of the opening angles of the Compton cone is high. This leads to the measured histogram distribution. The CANDELA setup can reduce this uncertainty because the detectors are pixelated. Backscattering events can be better suppressed if the backscattered photons deposit energy in a different pixel as during the first scattering. This way, they are not accidently counted as partial events.

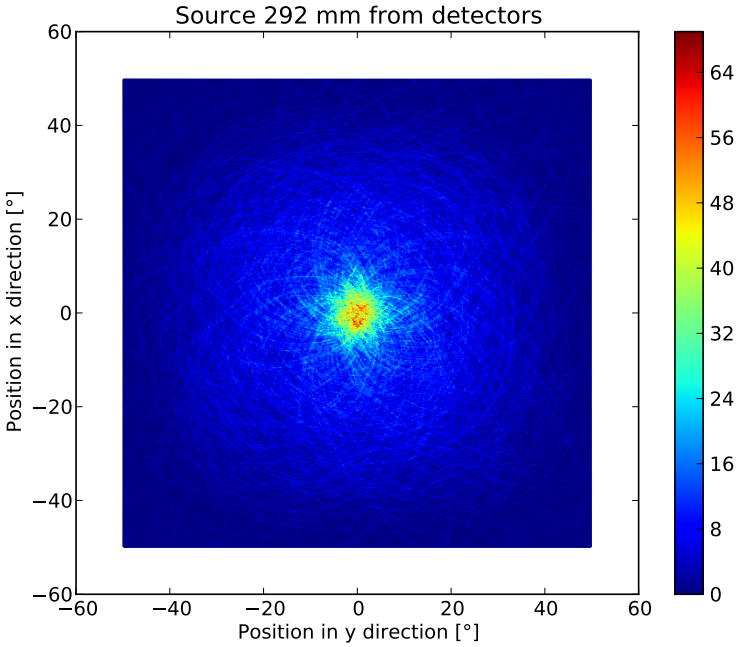

(a) Histogram for a simulated source at (0°, 0°)

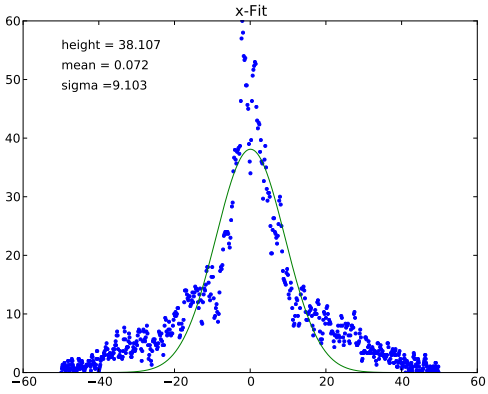

(b) Fit for the column including the maximum

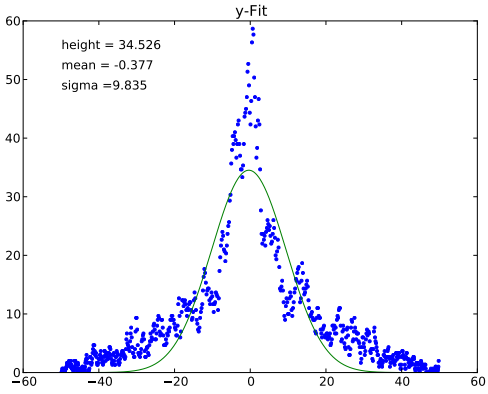

(c) Fit for the row including the maximum

Figure 6.6 Reconstruction of the source position simulated at (0°, 0°). In the histogram, the abscissa corresponds to the y direction, the ordinate to the x direction. Both are in units of degree. In the Figures (b) and (c) fits are shown for the spectra of the row and column of the histogram containing the maximum. The measured data is shown in blue. Mean value and standard deviation (sigma) for the fitted curves (green) are given. A field-of-view of 40° is chosen with a resolution of 0.1°

6.3.2 Fluorescence effects for the Am-241 source

In order to study fluorescence effects on the detector configuration, the energy spectra of the LED and HED are analysed. A histogram is generated from the energies deposited in the detectors and normalised to the measurement time, the detector size and the bin width. The resulting spectrum is then compared to the CANDELA measurement by Maier (2014). The spectra are shown in Figure 6.7.

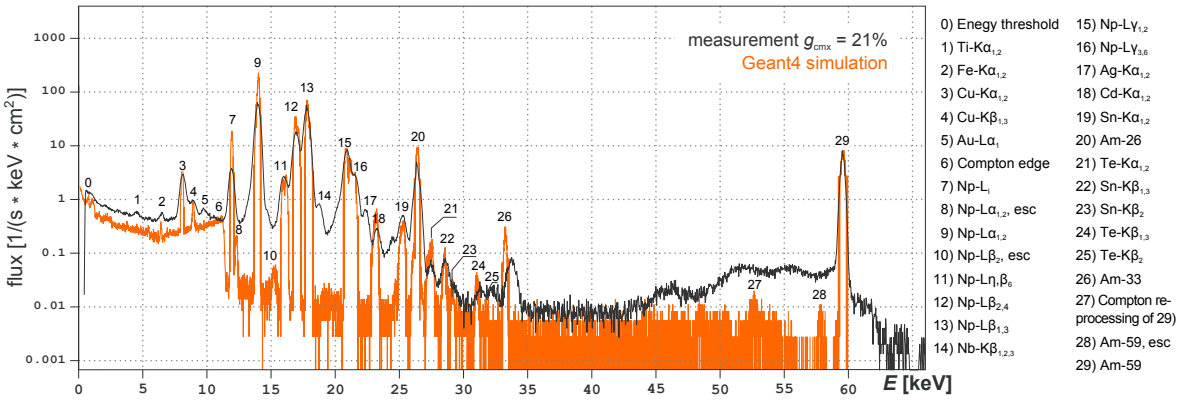

(a) LED

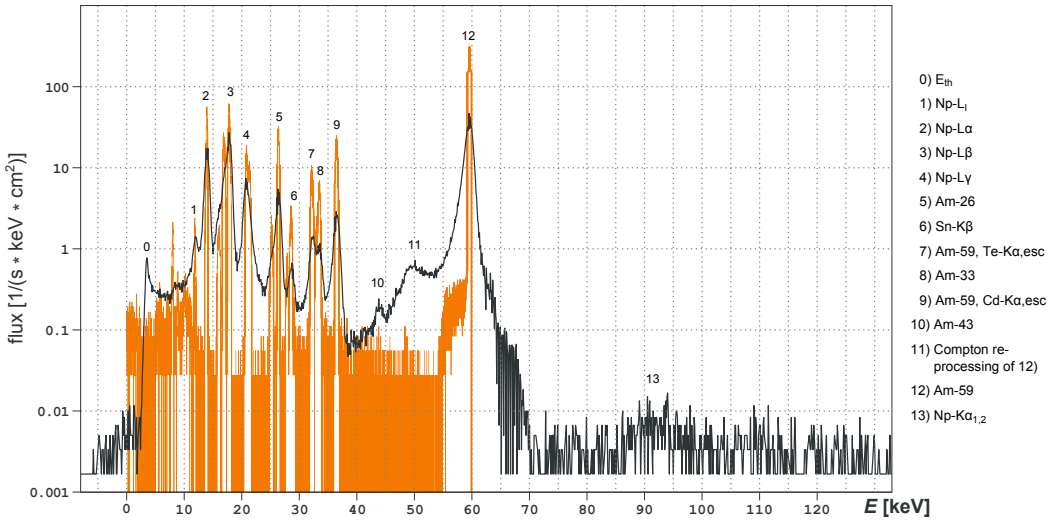

(b) HED

Figure 6.7 Spectral analysis of the deposited energy in the LED and the HED. The spectra show the comparison between the CANDELA measurement (black) and the simulation (orange). All energy and fluorescence lines as well as the silicon escape peaks of the simulation can be found in the simulated spectrum. The silicon escape peaks are not visible in the measured spectrum. Lines from the measurement that cannot be found in the simulated spectrum are generated by elements that are not implemented in the simulation. Small variations in the energy position are due to gain correction effects. The broad bulk at 53.4 keV is assumed to be due to Compton scattering effects.

It can be seen that all input energies lines are reproduced in the spectra of the LED for the simulation as well as for the measurement (lines 7, 9, 11, 12, 13, 15, 16, 20, 26 and 28). Photons producing these lines can lose energy by escaping fluorescence emission in the detectors. This generates silicon escape peaks in a distance of 1.74 keV from the input lines

(lines 8, 10 and 28). Because of the line broadening, some of them are coinciding with stronger lines.

Also the fluorescence lines produced by photons that are absorbed in parts of the detector geometry can be found. Both spectra show fluorescence lines of iron (line 2), copper (lines 3 and 4), cadmium (line 18), tin (lines 19, 22 and 23) and tellurium (line 21). In the CANDELA spectrum there are also lines from titan (line 1), gold (line 5), silver (line 17) and niobium (line 14). They originate from additional blinds, the stainless steel used for the outer shielding and electronic components that were not simulated.

At about 52 keV to 54 keV a small bulk is visible that cannot be explained by fluorescence effects. With an analysis of the simulated processes that lead to those energies in the detector it was figured out that these energy depositions are due to 59 keV photons that are Compton scattered at the copper blind or the copper shielding in front and on the back of the LED. The energy lost during this scattering cannot be deposited inside the detector. Because only photons that are scattered with an angle of almost 90° can enter the LED after the process, an energy deposition of about 53.33 keV is expected which correponds to the bulk position.

Also in the HED the input lines are well reproduced (lines 1, 2, 3, 4, 5, 8 and 12). Additionally, there is a fluorescence line of tin (line 6). The high energetic 59.54 keV photons create escape emission lines in the cadmium as well as in the telluride of the detector material (lines 7 and 9). The ameritium emission line at 43 keV was not simulated. Again, the bulk at 53 keV produced by Compton scattering at the detector shielding parts is visible. Except for the bulk, the flux for all lines is higher in the simulation than in the measurement. This corresponds to the broader energy distribution of the lines in the measured spectrum.

In comparison to the CANDELA measurement the simulation has a very high signal-to-noise-ratio. Most peaks lie well above the noise level, because the simulation does not include electronic noise. Also the Compton edge is clearly visible in the simulated spectrum. The spectrum of photons that are Compton scattered in the detector material is a continuum up to the Compton edge which corresponds to the maximal energy transfer from the photon to the electron due to Compton backscattering. It can be calculated as the energy difference between the initial photon energy and the energy loss at a scattering angle of 180°. For a 59.54 keV photon, the edge is at 11.25 keV as it is found in the simulated spectrum.

By superposition of the LED and the HED spectrum, the effect of the quantum efficiency becomes visible. Low energy photons deposit their energy mainly in the LED. They are absorbed in the process and do not reach the HED. The higher the photon energy, the higher is the probability that the photons can pass through the LED without interaction but can be detected in the HED. The effect is shown in Figure 6.8. The lower part of the figure shows the quantum efficiency of the detector setup while in the upper part the energy spectra are shown. It can be noted that the lines with lower energy are detected with a higher flux by the LED up to an energy of about 17 keV. For higher energies the flux in the HED gets larger than the flux in the LED. This corresponds to the behaviour of the quantum efficiency of the detectors.

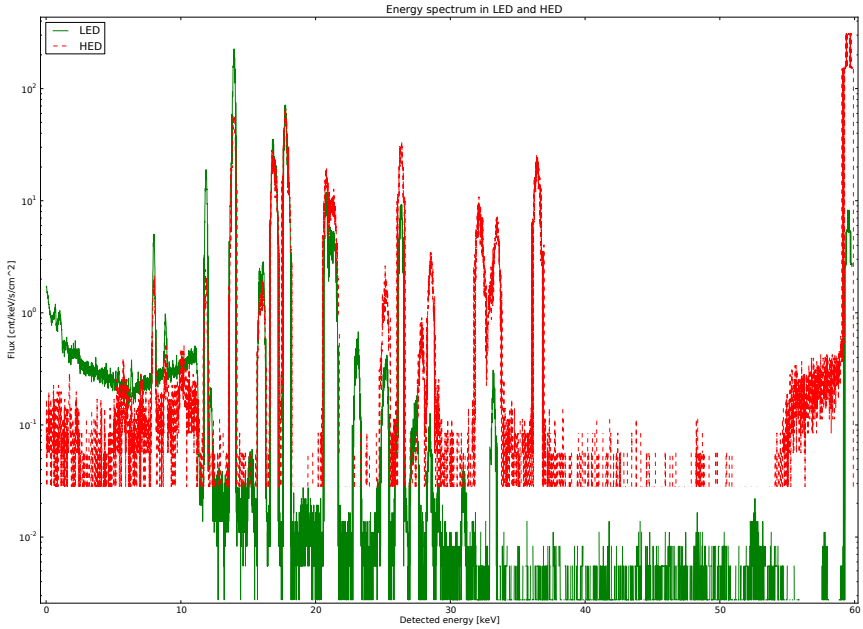

(a) Flux spectrum

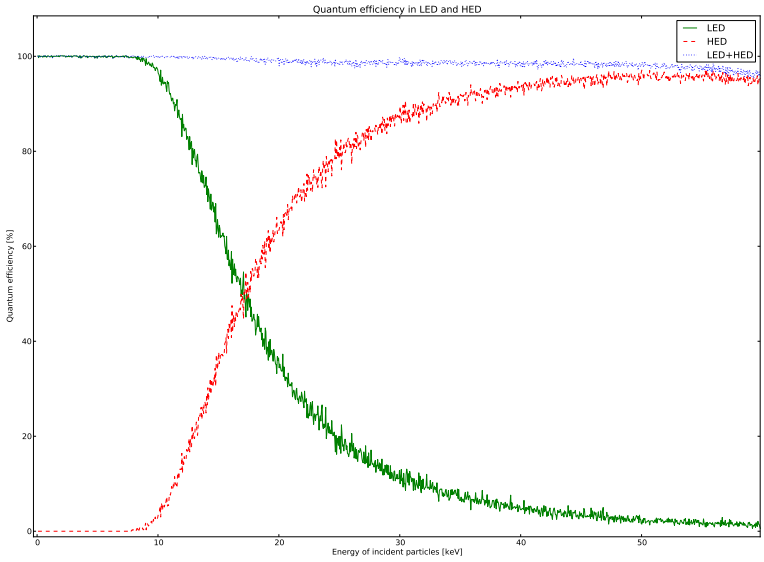

(b) Quantum efficiency

Figure 6.8 Comparision of the quantum efficiency and the energy flux in the detectors. Figure (a) shows the superposition of the energy spectra measured in the LED and the HED. The dominance of the flux in the LED at low energies and the reverse behaviour at high energies correspond to the quantum efficiency of the detectors shown in (b). The dotted blue line on top of the two quantum efficiencies is the total quantum efficiency of the instrument as the sum of the two individual efficiencies.

7 ATHENA: Graded-Z Shield simulation

The *Advanced Telescope for High ENergy Astrophysics*, ATHENA (Nandra et al., 2014), is an X-ray observatory in heritage of the *International X-ray Observatory* (IXO). It was selected by ESA in 2014 to be launched in 2028 to study the energy range from 0.2 keV to 15 keV. The focus of the observatory will be on the analysis of the formation of the largest structures in the universe and the influence of black holes on the process. An image of the ATHENA telescope can be found in Figure 7.1. ATHENA has to instruments: an X-ray Integral Field Unit (X-IFU) and a Wide Field Imager (WFI). The ATHENA instrument that is studied in this chapter is the WFI which is an active pixel sensor camera with a 40'x40' field of view that has high time resolution down to 8 µs and is able to handle a high count-rate capability of $>$ 1 Crab. It studies an energy range between 0.1 keV and 15 keV with an energy resolution of ΔE <150 eV (FWHM @ 6keV) (Rau et al., 2013).

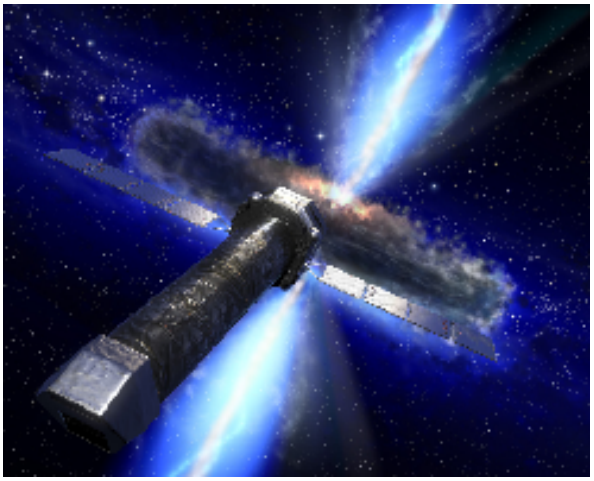

Figure 7.1 The Athena observatory. Image from the Athena collaboration

The focus of the simulation is on the radiation environment and the shielding of the detectors. For the predecessor mission IXO, a Graded-Z Shield was proposed. The functionality of this shield was studied by Hauf (2012). In this chapter those results are re-evaluated and the efficiency of another shield material configuration is tested. There is currently no ATHENA geometry availible that can be simulated because the geometry setup is still in development.

7.1 Simulation setup of the ATHENA simulation

For the re-evaluation of the results, the Geant4 simulation code is taken from Hauf (2012). This code was written for Geant4 9.1.3. Because of the changes of the packages including the physical processes, it was not possible to upgrade the simulation to the current version Geant4 10.0.2, still it was achievable to perform the simulation with Geant4 9.3.2.
The analysis of the data differs from the analysis done by Hauf (2012), because different analysis tool were available.

The detector geometry for the WFI simulation is rather complex, still the detector itself is a simple silicon wafer with a diameter of 152.4 mm and a thickness of 450 µm. It contains a rectangular pixelated area with an edge length of 102.4 mm including 1024x1024 pixels. The detector is shown in Figure 7.2(a).

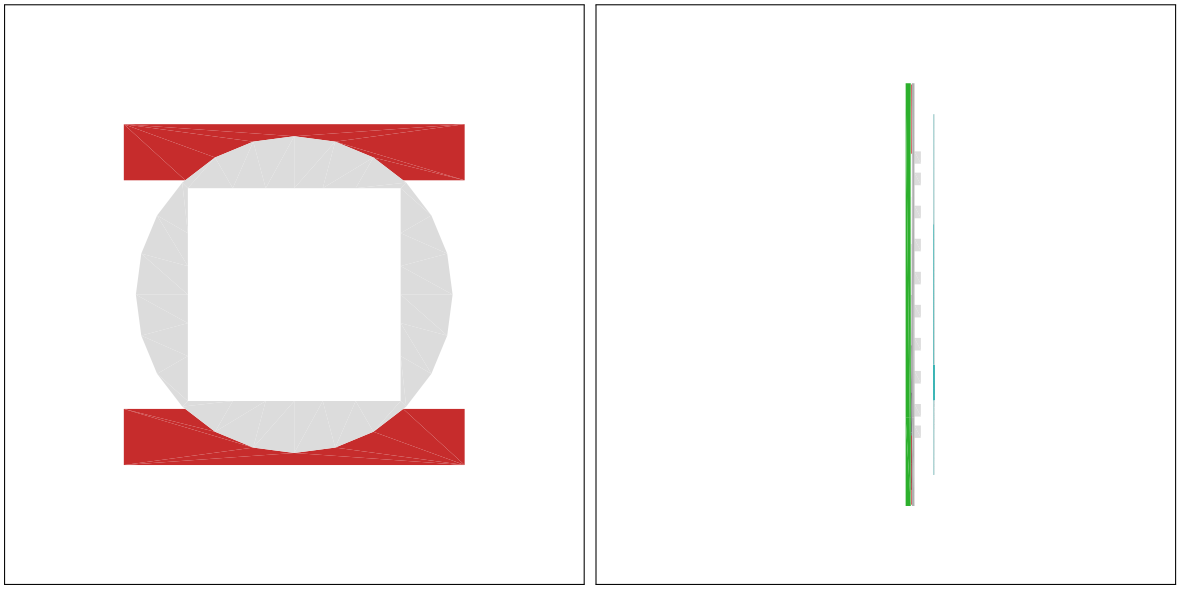

(a) Detector (b) Additional layers

Figure 7.2 Geometry of the ATHENA detector. In 7.2(a) the circular area in the centre is the silicon wafer with a rectangular pixelated area within. The red area at the top and bottom of the detector is a heat foil. This is a top view of the detector. The sideways view 7.2(b) shows the position of two filter foils made of mylar and aluminium (blue) as well as the read-out chips at the backside of the detector (small grey rectangulars). The green layer in front of the detector is the a ceramic layer. The entrance window is opened to the left side of the image.

The detector is covered by three layers: two oxidation layers of SiO and Si_3N_4 with a thickness of 35 nm each along with an aluminium layer with a thickness of 70 nm. Those layers together with the silicon wafer make up the detector region (Figure 7.2(b)).
All further parts of the geometry from the foil holder to the sunshade are summarised in Figure 7.3.
The most important part for this simulation apart from the detector is the Graded-Z Shield whose effect is studied. This kind of shield is constructed from layers of materials with decreasing atomic numbers. Layers made of higher Z elements are thereby further away from the detector than those made of lower Z elements. This way, incident high energetic particles are absorbed in higher layers by producing fluorescence photons that are reabsorbed by inner layers producing lower energetic fluorescence photons themselves. By passing through all layers the fluorescence background can be decreased to an energy lower than the low energy threshold of the detector. Two shields are studied in this work. In a first step, the shield implemented for IXO in 2010 is re-evaluated, then a slightly different configuration from 2012 is tested and compared to the results found by Hauf (2012) in the original simulation. The materials and thicknesses of the shielding layers are given in Table 7.1.
The main difference of the two shield configurations are the innermost layers of the shield. While in the configuration of Hauf (2012) the innermost layer is made of beryllium, for the older configuration graphite is used. Both materials have very low energetic K_α-emission lines

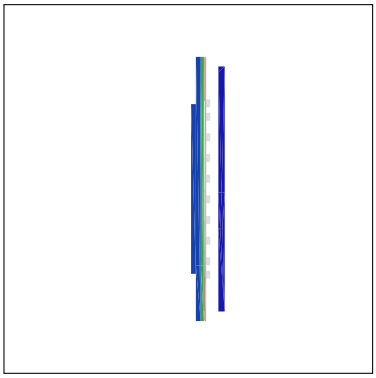

(a) Foil frame (blue, backside) and pressure plate (blue-grey, front)

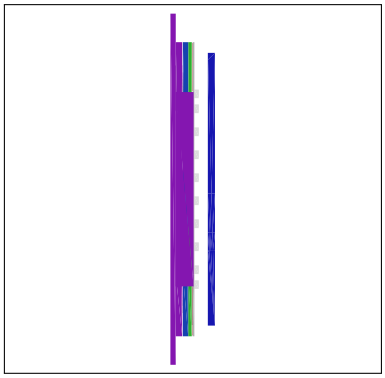

(b) Spring plate (violet) hold by eight springs (not visible)

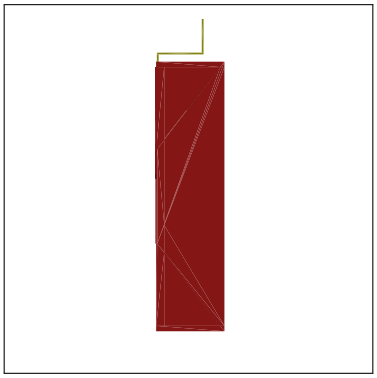

(c) Geometry covered by base plate (brown) with thermal strap (yellow)

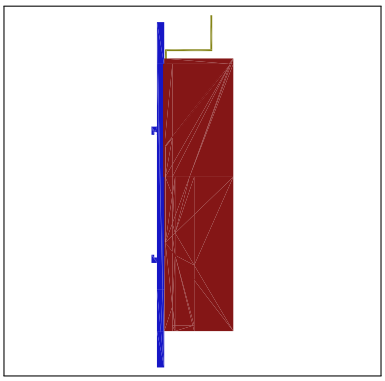

(d) Mounting Plate (blue)

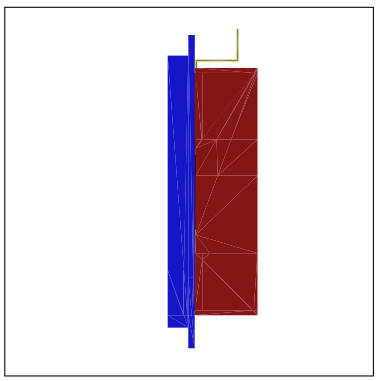

(e) Filter cover (blue) containing filter sled (not visible)

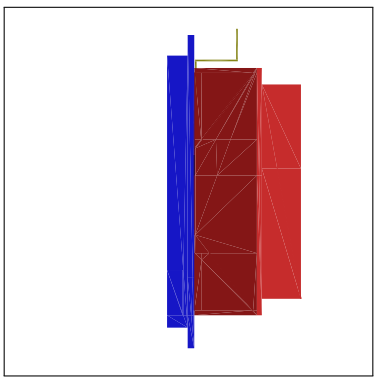

(f) Hard X-ray Imager (light brown, backside)

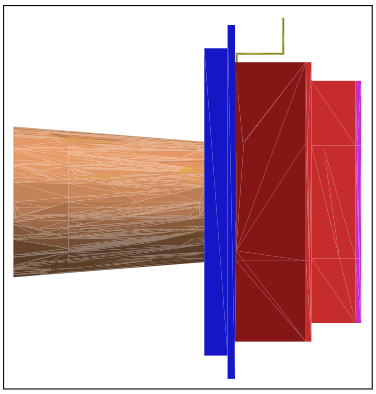

(g) HXI cover plate (violet, backside) and buffle (brown)

Figure 7.3 Full simulated ATHENA setup. The whole setup excluding the baffle is covered by the graded-Z shield. The shield is not shown because the structure is too complex for the visualisation program used.

at 108.5 eV and 277 eV, respectively. However, beryllium is highly toxic and more complicated to handle. Therefore graphite is tested again as an alternative layer material.

Table 7.1 Layers of the graded-Z shields. Two configurations are tested. The second column contains the layer thicknesses for the simulation by Hauf (2012), the third column a slightly different configuration. Higher Z elements are placed further away from the detector.

Material		Thickness [mm]	Thickness [mm]
73	Ta	1.5	1.5
50	Sn	2.2	2.2
29	Cu	1.2	0.5
13	Al	0.3	0.3
4	Be	0.1	-
6	C	-	0.1

For the physical processes, four kinds of Physics Lists are included: the Low-Energy-Electromagnetic-Physics List, the Standard-Electromagnetic-Physics List, the Hadron-Physics List and the General Physics List. The Low-Energy-Electromagnetic Physics List is introduced to avoid the differences found in the low energy range for the version Geant4 9.3.2 while the Hadron-Physics List solves the differences at high energies by using different implemented models. The General Physics List adds decay processes to the process list. All processes with their models are summarised in Table 7.2

Table 7.2 Geant4 packages used for the Athena simulation. It is γ = photon, e^- = electron, e^+ = positron, μ = muon, π = pion, h = hadrons, p = proton and n = neutron. Additional or alternative hadron packages used for protons, neutrons and pions are stated below. The underlying model is the Quark-Gluon-String Precompound model with binary cascades and hadron impact ionisation *QGSP_BIC_HP model* (including PIXE emission)

Particle	Package	Energy Range	Model
γ	G4LowEnergyRayleigh	>250 eV	Livermore
	G4LowEnergyPhotoElectric	>250 eV	Livermore
	G4LowEnergyCompton	>250 eV	Livermore
	G5LowEnergyGammaConversion	>250 eV	Livermore
	G4PhotoElectricEffect	0 eV-10 TeV	Sandia parametrisation
	G4ComptonScattering	0 eV-10 TeV	Klein-Nishina model
	G4GammaConversion	0 eV-10 TeV	Bethe-Heitler model
e^-/e^+	G4eMultipleScattering	0 eV-10 TeV	UrbanMsc92: semi-empirical model based on Lewis theory
	G4LowEnergyIonisation	250 eV-100 GeV	EEDL database table
	G4LowEnergyBremsstrahlung	250 eV-100 GeV	EEDL database table
	G4eIonisation	0 eV-10 TeV	MollerBhaba: Moller-Bhabha model
	G4eBremsstrahlung	0 eV-1 GeV	Standard model for Bremsstrahlung for e^-/e^+
		1 GeV-10 TeV	Improved model including LPM

e^+	G4eplusAnnihilation	0 eV-10 TeV	eplus2gg: Annihilation of an electron-positron pair into two gammas
μ^-/μ^+	G4MuMultipleScattering	0 eV-10 TeV	UrbanMsc92: semi-empirical model based on Lewis theory
	G4MuIonisation	0 eV-200 keV	Bragg model
		200 keV-1 MeV	Bethe-Bloch model
		1 MeV-10 TeV	Bethe-Bloch model for muons
	G4MuBremsstrahlung	0 eV-10 TeV	Bremsstrahlung model for muons
	G4MuPairProduction	0 eV-10 TeV	Pair production model for muons
μ^+	G4MuonMinusCaptureAtRest		
h	G4hMultipleScattering	0 eV-10 TeV	UrbanMsc95: semi-empirical model based on Lewis theory
	G4hLowEnergyIonisation	1 keV-2 MeV	ICRU_R49p[1] with Borkos effect: model for the ionisation
	G4hIonisation	0 eV-2 MeV	Bragg / ICRU73Q0: model for the ionisation due to anti-hadrons
		2 MeV-10 TeV	Bethe-Bloch
	G4LElastic	>0 GeV	Elastic scattering model
p	G4BinaryCascade	0 eV-10.5 GeV	
	G4Fission	10 GeV-100,000 GeV	
	G4AntiProtonAnnihilationAtRest		
n	G4LElastic	>0.019 GeV	
	G4NeutronHPElacstic	0 GeV-0.02 GeV	
	G4HPNeutronInelastic	0 GeV-0.02 GeV	
	G4LAntiNeutronInelastic	0 GeV-25 GeV	
	G4HEAntiNeutronInelastic	20 GeV-100,000 GeV	
	G4BinaryCascade	10 GeV-100,000 GeV	
	G4LFission	>0 GeV	
	G4LCapture	>0.019 GeV	
	G4HPNeutronCapture	0 GeV-0.02 GeV	
	G4AntiNeutronAnnihilationAtRest		
$\pi^\pm$	G4hIonisation	0 eV-297.504 MeV	Bragg / ICRU73Q0: model for the ionisation due to anti-hadrons

[1] International Commission on Radiological Protection

	297.504 MeV-10 TeV	Bethe-Bloch
G4LPionPlusInelastic	0 GeV-55 GeV	
G4Fission	10 GeV-100,000 GeV	
G4PiMinusAbsorptionAtRest		

A source is implemented as a General Particle Source. There are two kinds of background radiation that is analysed in the following. On the one side there is the *Cosmic X-ray Background* (CXB). The simulated CXB spectrum covers an energy range from 0.01 MeV to about 91.2 GeV. The spectrum used as input for the simulation by Hauf (2012) is shown in Figure 7.4. For the simulation the photons are coming from a sphere around the detector geometry with a radius $r = 50\,\mathrm{m}$. This large radius is chosen to guarantee a homogeneous photon background. They have a cosine angular distribution and a flux of 15.6232 photons $\mathrm{s}^{-1}\mathrm{cm}^{-2}\mathrm{sr}^{-1}$ (Gruber et al., 1999).

On the other hand there is a proton background induced by the solar winds as well as by high energetic cosmic rays. This background depends strongly on the orbit of an observatory and the solar activity and can be estimated by various models. For the IXO orbit it was calculated with the simulation software CREME96[2] for a launch in 2020. It is simulated with an energy range from 1 MeV to 100 GeV. The input spectrum for this background is also given in Figure 7.4. The proton origin is simulated as the same sphere as for the CXB with the same angular distribution and a flux of 4.531953 protons $\mathrm{s}^{-1}\mathrm{cm}^{-2}\mathrm{sr}^{-1}$.

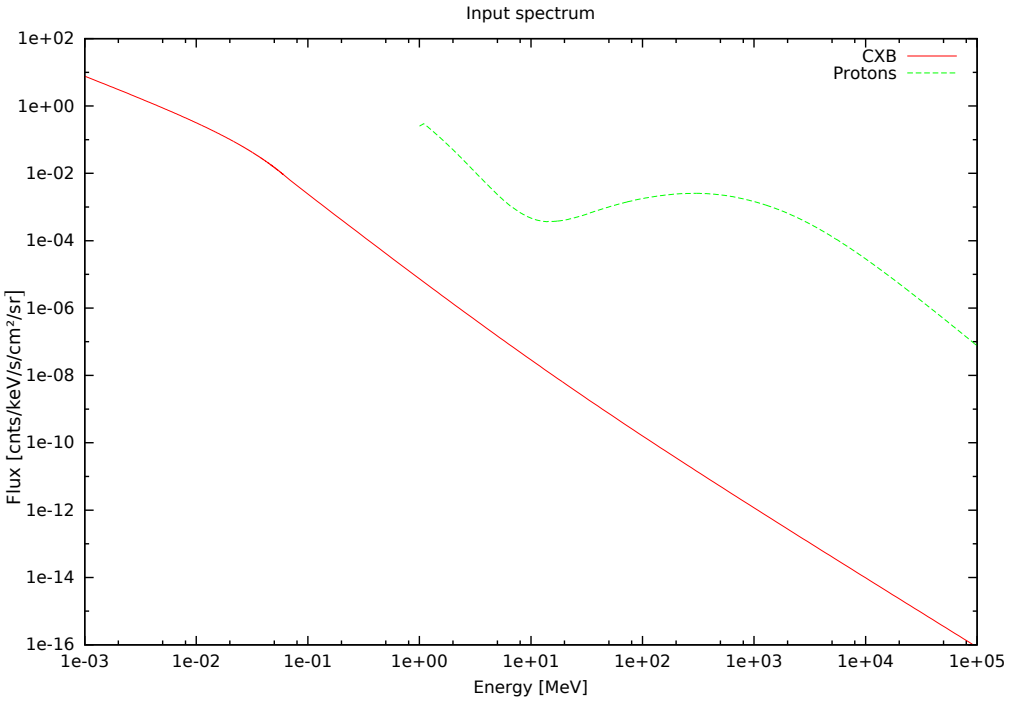

Figure 7.4 Input spectrum of the IXO simulation. The decreasing red curve shows the behaviour of the CXB while the green curve correspond the the proton background.

To calculate the simulation time, the true number of primary particles N_t has to be calculated. This can be done via

[2]CREME: Cosmic Ray Effects on MicroElectronics

$$N_\mathrm{t} = \int\int F\cos(\vartheta)\mathrm{d}\Omega\mathrm{d}A \tag{7.1}$$

$$= F4\pi^2 r^2 \tag{7.2}$$

where F is the flux, Ω the solid angle and A the surface area of the sphere. The appearance of the cosine in the formula is due to the Lambertian emission law of the cosine angular distribution. Hereby, the limits for the integration over the solid angle are chosen in a way that the particles are only radiated to the inside of the sphere. It is further reduced to an opening angle $\vartheta_\mathrm{max} = 1.15°$ in order to decrease the simulation time. This is chosen because only particles that are emitted in this direction can interact with the detector geometry anyhow.
The corresponding true measurement time is then the ratio of the number of simulated particles and the number of particles generated per second on the sphere.

$$t = \frac{N_\mathrm{s}}{N_\mathrm{r}} = \frac{N_\mathrm{s}}{F4\pi^2 r^2 \sin^2(\vartheta_\mathrm{max})} \tag{7.3}$$

The number of simulated particles together with the corresponding equivalent times in orbit are given in Table 7.3 for the CXB and cosmic rays.

Table 7.3 Calculated times for the IXO simulation. From the number of particles generated by Geant4, the corresponding measurement time in orbit can be calculated depending on the particle flux.

Particle	Flux [Particles $\mathrm{s}^{-1}\mathrm{cm}^{-2}\mathrm{sr}^{-1}$]	Simulated particles	Time [s]
CXB (γ)	15.6232	10^9	648.55
Cosmic rays (protons)	4.5319532	10^7	22.36

7.2 Output and evaluation of the data

If a particle or a photon deposits energy in the detector volume, the corresponding step is classified as a hit. For every hit the deposited energy, the position of the interaction, the global time, the particle name, the name of the volumes at the beginning and the end of the step and the interaction process name are stored. The data are written to a fits-file[3]. For this simulation, each file contains a table with 18 columns: the frame number, the time of interaction, the initial energy of the primary particle, the total energy deposition of the particle in the detector, the name of the volume in which the process took place, the name of the particle and the process as well as the position given in mm and in pixel. Each value is stored for events in which particles deposit energy in the detector volume or in the ASICs[4] that were planned for IXO. Those latter events are neglected in this evaluation and will be the subject of future studies. Still, the data structure was maintained.

The fits-files can be evaluated with the fits-view software *fv* by NASA. This allows construction of histograms for all table columns. For the visualisation of the data, histograms for the energy deposition in the detector are plotted for secondary electrons, gammas and other particles. The results are presented in the next section.

[3] fits: flexible image transport system
[4] Asic: Application-Specific Integrated Circuit

7.3 Results of the ATHENA simulation

The WFI is designed for measuring energies between 0.1 keV and 15 keV. That is why for the background analysis only this energy range is considered. For the analysis, the background is divided into secondary electrons, photons and other particles. The latter part contains particles such as primary protons, positrons, pions or kaons.

Carbon shield configuration

Basing on older Geant4 code from (Hauf, 2010), a configuration with an innermost layer made of carbon is tested. The results are shown in Figure 7.5.

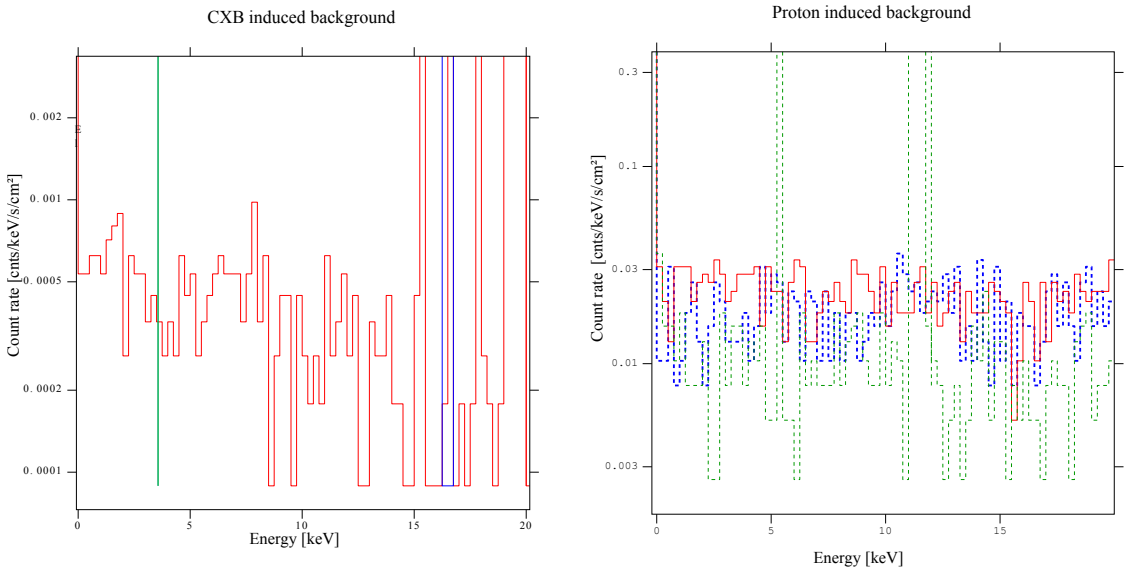

(a) CXB (b) Protons

Figure 7.5 Background spectra for the carbon graded shield configuration. (a) shows the CXB induced background while (b) indicates the proton induced background. The background is divided into secondary electrons (blue), photons (red) and other particles (green) (lines are dotted in this spectrum for clarity). No fluorescence lines are visible which is assumed to be due to the low statistics. The binning is set to 250 keV.

The background rates for the specific particles are summarised in Table 7.4.
For the protons a mean background rate for the sum of all particles of $17.42 \cdot 10^{-3}$ $\frac{\text{cnts}}{\text{keV}\cdot\text{s}\cdot\text{cm}^2}$ is found with a maximum value of $36.18 \cdot 10^{-3}$ $\frac{\text{cnts}}{\text{keV}\cdot\text{s}\cdot\text{cm}^2}$. The CXB induces a total mean background rate of $1.39 \cdot 10^{-4}$ $\frac{\text{cnts}}{\text{keV}\cdot\text{s}\cdot\text{cm}^2}$ and a maximum count rate of $9.8 \cdot 10^{-4}$ $\frac{\text{cnts}}{\text{keV}\cdot\text{s}\cdot\text{cm}^2}$.
In the considered energy range between 0.1 keV and 15 keV no fluorescence lines are visible. However, this could be due to the low statistics because from the generated 10^9 photons that are generated for the CXB, only 939 photons are detected in the WFI together with 40 electrons and 14 positrons. For the proton induced background from the original 10^7 protons,

Table 7.4 Background rates in the carbon graded shield configuration. The values are calculated for the sensitive detector range below 15 keV. All rates are in $\frac{\text{cnts}}{\text{keV}\cdot\text{s}\cdot\text{cm}^2}$

Proton induced background			
Particle	Mean rate $[10^{-3}]$	Standard deviation $[10^{-3}]$	Maximum rate$[10^{-3}]$
Electron	18.65	7.4	36.18
Photon	23.52	6.0	33.6
Others	10.08	6.4	36.18
CXB induced background			
Particle	Mean rate $[10^{-4}]$	Standard deviation $[10^{-4}]$	Maximum rate$[10^{-4}]$
Photon	4.13	2.00	9.80
Electron	0.02	0.16	0.89
Others	0.01	0.12	0.89

12,749 secondary electrons are generated that hit the detector as well as 3,918 photons and 64,721 other particles. Most secondary particles have energies above the considered energy range.

Beryllium shield configuration

The spectra of the proton and CXB induced background in the WFI with a beryllium layer instead of a carbon layer as the innermost layer of the graded-Z shield are shown in Figure 7.6.

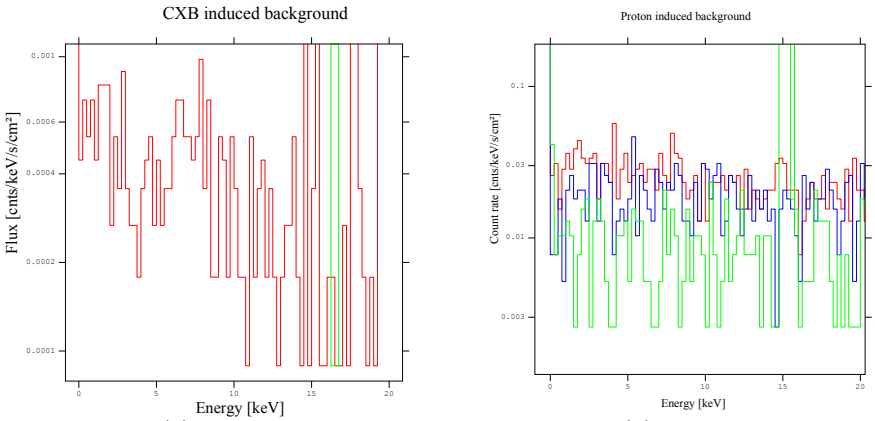

(a) CXB (b) Protons

Figure 7.6 Background spectra for the beryllium graded shield configuration. (a) shows the CXB induced background while (b) indicates the proton induced background. The background is divided into secondary electrons (blue), photons (red) and other particles (green). The binning is set to 250 keV.

The results of the rate analysis can be found in Table 7.5.
The mean background rate for the proton induced background in this configuration is $18.46 \cdot 10^{-3}\ \frac{\text{cnts}}{\text{keV}\cdot\text{s}\cdot\text{cm}^2}$. The maximum background rate is $56.85 \cdot 10^{-3}\ \frac{\text{cnts}}{\text{keV}\cdot\text{s}\cdot\text{cm}^2}$ The CXB induced spectrum includes no strong fluorescence peaks in the part of the spectrum for which the WFI is sensitive. The mean background rate for the CXB is $1.36 \cdot 10^{-4}\ \frac{\text{cnts}}{\text{keV}\cdot\text{s}\cdot\text{cm}^2}$ with a

Table 7.5 Background rates in the beryllium graded shield configuration. The values are calculated for the sensitive detector range below 15 keV. All rates are in $\frac{\text{cnts}}{\text{keV}\cdot\text{s}\cdot\text{cm}^2}$

Proton induced background			
Particle	Mean rate $[10^{-3}]$	Standard deviation $[10^{-3}]$	Maximum rate$[10^{-3}]$
Electron	19.04	8.11	46.5
Photon	26.83	8.49	56.85
Others	9.52	6.84	41.35
CXB induced background			
Particle	Mean rate $[10^{-4}]$	Standard deviation $[10^{-4}]$	Maximum rate$[10^{-4}]$
Photon	4.04	2.25	9.80
Electron	0.03	0.16	0.89
Others	0.0	0.0	0.0

maximum rate of $9.8 \cdot 10^{-4}$ $\frac{\text{cnts}}{\text{keV}\cdot\text{s}\cdot\text{cm}^2}$
Also for this simulation, statistics are low. Longer simulation times are needed in order to get more significant data. From the generated protons 12,725 secondary electrons, 4,214 photons and 64,582 other particles reach the WFI. In the CXB simulation 931 photons, 33 electrons and no other particles are detected.

The rates found for the backgrounds for both configurations are very close. Differences in the mean background rates can be explained with statistical fluctuations. A more important property for the quality of the shields would be the position of the remaining fluorescence lines of the innermost graded-Z shield layer. Those lines are not visible in the spectra. More statistics is required to make a clear statement about the shield configurations.

The spectrum of the proton induced background can be compared to the spectrum found by Hauf (2012). Both spectra are shown in Figure 7.7
As mentioned before, the mean background rate found for the beryllium shield configuration found during this work is $18.46 \cdot 10^{-3}$ $\frac{\text{cnts}}{\text{keV}\cdot\text{s}\cdot\text{cm}^2}$. The background from Hauf (2012) is in the order of $0.9 \cdot 10^{-3}$ $\frac{\text{cnts}}{\text{keV}\cdot\text{s}\cdot\text{cm}^2}$. The background found by Hauf is therefore is a factor of ten lower than it was found during this work. Also no fluorescence lines are visible in the spectrum of this work. This could be explained by the reduced statistics of the presented simulation that is a factor of ten lower.

Another reason for the lower background found by Hauf (2012) could be the pattern analysis done in that work. Hauf (2012) allocated a time information to every primary particle chosen randomly from times up to the calculated total time in orbit. Processing times of secondary particles are added to this time stamp. This way, time frames of 1 ms could be evaluated separately. Whereas low energetic particles mainly deposit energy in only one pixel of a detector, sometimes inducing energy in the adjacent pixels, minimum ionising particles (MIPs) leave a trace in the detector depositing energy in many pixels on their way. By analysing the pattern of energy deposition in every frame, those background events can be further suppressed and the count rate of the background decreases.

For ATHENA a further kind of background reduction is planned by installing a 3 cm Cu shield around the detector to block incident protons. This will reduce the count rate of proton induced background. The influence of secondary particles emitted in this process on the detector geometry, is a subject of further studies.

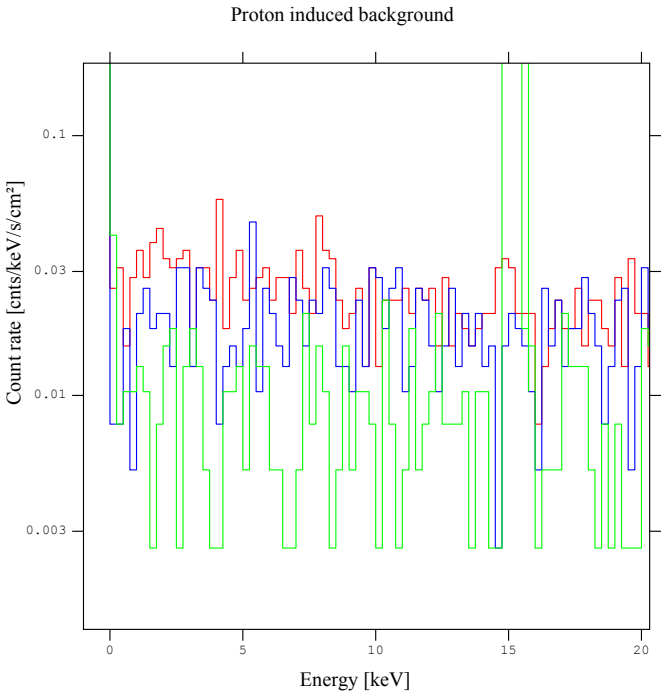

(a) WFI background simulation according to this work

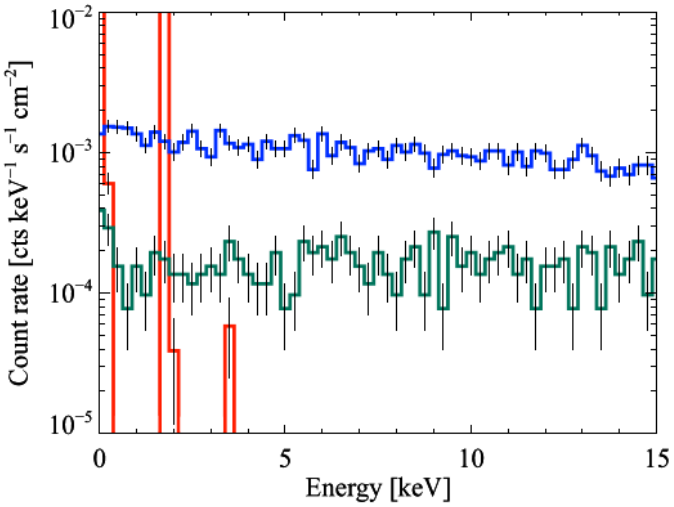

(b) WFI background simulation according to Hauf (2012)

Figure 7.7 Comparison between the simulation results by Hauf (2012) and the ones found during this work for the proton induced background of the WFI with a Be layer in the graded-Z shield. The background is divided into secondary electrons (blue), photons (red) and other particles (green). The binning is set to 250 keV.

8 Summary and Outlook

In the process of this work, four simulation projects were pursued. The comparability test between the Geant4 versions Geant4 9.3.2, 9.6.2 and 10.0.2 compared the results of an energy loss simulation for 458 MeV electrons in 216 µm silicon. The test showed small discrepancies below 600 keV and greater discrepancies above 1700 keV for Geant4 9.3.2 in comparison with the newer versions. However, the overall behaviour of the curves matched each other so that the data produced by each version is thought to be comparable in the simulated energy range.

For the eRosita simulation, the quantum efficiency measured by Ebermayer et al. (2010) in a laboratory setup could be reproduced. The absorption edges found in the spectrum were slightly deeper in the laboratory measurement than in the simulation which is assumed to be due to small differences in the layer thickness of the detector and its oxide layers.

The Compton camera simulation could well reconstruct the true source position using a realistic ellipses retrojection approach of the Compton scattering process. For the energy range up to 100 keV, the best quantum efficiency for the setup was found for a combination of two germanium detectors with a thickness of 0.3 cm for the upper detector and 2.5 cm for the lower one. For a higher energy range up to 250 keV a three layer detector setup was tested with the best yield for an additional central layer with a thickness of 0.1 cm.
The adaptation of the algorithm to the CANDELA stacked detector setup also produced good results. The fluorescence background induced by the source photons was well reproduced showing all expected input and fluorescence lines as well as the corresponding silicon escape peaks. Also, the Compton edge was clearly visible at the expected energy.

The results of the ATHENA simulation by Hauf (2012) were reproduced except for a factor of ten in the background rate and the absence of fluorescence lines due to the reduced statistics of the simulations.

However, there are still topics that could be further investigated. Those topics are shortly presented in the following.

The reconstruction algorithm for the source position developed during this work for the Compton camera could reproduce the true sources in the defined accuracy range. However, a systematic error was found that is not yet explained and which leads to a dependency of the reconstruction accuracy on the deviation of the source from the central position. There could be an influence of the binning on this error but this was not further evaluated yet.

Furthermore, the reconstruction process is dependent on the distance. For the reconstruction of the source position the exact distance between the detector and the source has to be known. If the reconstruction plane is set too far from the detector, the event ellipses would intersect in a circle instead of a point. In the contrary case, the ellipses would not intersect at all.
Retrieving this argumentation, the Compton telescope setup could be used for the determination of the source distance if only the accuracy of the reconstruction is high enough. This idea existed, but was not further persued during this work.

An algorithm for the reconstruction of the source position in Compton telescope was not achieved in the time available. In the case of very distance sources, the distance needed for the calculation is infinite. The source emits parallel beams of light. This cannot be handled by the algorithm for the Compton camera. Also, instead of a geometrical position only the direction to the source could be given. The code would have to be adjusted to fulfil this altered approach.

Further work should be applied to the ATHENA simulation. In the period of time available, only two shield configurations could be tested, which were not very different. Longer simulation times are needed in order to gain spectra with statistics and to test the comparability of the presented simulation with Hauf (2012).
Also, the upgrade of this code to the Geant4 10.0.2 version was not achieved, but would be necessary to include the most actual implementation of the physical processes. Additionally, testing a detector geometry closer to the ATHENA WFI than to the IXO setup would be interesting.

Appendix

1 Working with Geant4

Geant4 is a simulation tool using the Monte-Carlo method. In the following the installation process on a Linux based computer as well as the basic concepts for running simple examples on Geant4 will be described. There are manuals for the installation process under Windows and Mac OS on the CERN-website[1].

1.1 Required software

The installation is run on a computer using a Linux operating system more precisely Kubuntu. Geant4 can be received online via the download area of the CERN-website[2]. The version mainly used in this work is Geant4 9.6 with patch 2. For a Unix operating system the source code provided in the GNU or Linux tar format is needed. It can be stored and extracted in an arbitrary directory. Before starting the actual installation it is recommended to check if the required Linux packages are installed. A list is provided here.

- cmake
- cmake-dbg
- cmake-data
- cmake-qt-gui
- make
- freeglut
- freeglut-dev
- libgl1-mesa-dev
- libglu1-mesa
- libglu1-mesa-dev
- libx11-dev
- mesa-common-dec
- libxmu-dev
- libxmu-headers

Additionally, a text editor (for example emacs) as well as a c++-compiler (like g++) should be available.

[1] `http://geant4.web.cern.ch/geant4/`
[2] `http://geant4.web.cern.ch/geant4/support/download.shtml`

1.2 Installation process

Furthermore, the path leading to the folder in which the Geant4 version should be installed will be called `path/to/Geant4.9.6.p02`. So in the folder `path/to` a new folder has to be created in which the installation files can be stored. The terminal input is then

```
$ cd path/to
$ mkdir geant4.9.6.p02-build
```

In this new directory the CMake file from `path/to/Geant4.9.6.p02` can be run.

```
$ cd path/to/geant4.9.6.p02-build
$ cmake -DGEANT4_INSTALL_DATA=ON -DGEANT4_USE_OPENGL_X11=ON
-DCMAKE_INSTALL_PREFIX=/path/to/geant4.9.6.p02-install/
 ~/path/to/geant4.9.6.p02
```

Hereby the first argument downloads and installs automatically all missing datasets important for the application. The second one includes the OpenGl viewer which is needed for the visualisation during the simulation. Finally, the last two arguments indicate the paths to the directory the program should be installed to and the directory containing the source files. If the application should be used by several users the directory /opt/ is recommended as installation directory.

The program will be compiled. It has to be considered that the datasets included via `-DGEANT4_INSTALL_DATA` can also be included manually after the installation. Therefore, the required files can be downloaded from the Geant4 website in *Downloads* and extracted in the installation directory `path/to/geant4.9.6.p02-install/share/Geant4-9.6.2/data`. If the application is compiled successfully, the process will end with the following output.

```
-- Configuring done
   -- Generating done
   -- Build files have been written to: /path/to/geant4.9.6-build
```

Subsequently, an executable make file has to be generated from the obtained file.

```
$ make -jN
```

Here N is the number of processor cores that should be used for the task. Finally, the actual installation takes place with

```
$ make install
```

If authorisation problems appear during the installation, `sudo` has to be set in front of the `make` command to execute the installation.

Afterwards Geant4 is completely installed and can be used for simulations. Further information can be found in the manual provided by CERN (Geant4 collaboration, 2013).

1.3 Running simple examples

If Geant4 is installed, also some examples of how to use Geant4 are included in the directory. They can be found in the source directory in `/path/to/geant4.9.6.p02/Examples`. There are three different levels of difficulty: Basic, novice and advanced. For beginners they are a good medium to get to know the features of Geant4.

The compilation process of the example code is the same for every Geant4 project. For reasons of recovery the examples should be copied to a project directory, so the original source code is not changed while training on the code.

In the following it is assumed that the Geant4 files were stored in the directory `/Example` in a folder found at `path/to/projects`. The process of compilation is very similar to the steps taken to install Geant4. For the beginning a new directory, the so called build directory, has to be created, in which the compiled data should be stored.

```
$ cd path/to/projects/
$ mkdir Example-build
$ cd Example-build
$ cmake -DGeant4_DIR=/path/to/geant4.9.6.p02-install/lib/
        Geant4-9.6.2 path/to/projects/Example
```

As arguments in the last step the directory leading to the Geant4config.cmake file in the Geant4 installation folder and the one to the example directory were given. If the code compiles without errors, the output in the control panel is:

```
--Build files have been written to: /path/to/projects/Example-build
```

The generated files can be executed as explained for the installation.

```
$ make -jN
```

Again N is the number of used processor cores. The application generates an executable file, here called `exampleExample`. So the simulation can be started by

```
$ ./exampleExample
```

1.4 Functionality of the OpenGl viewer

The simulation can be visualised in a viewer after compilation of the source code. In this work, the OpenGl viewer was used. With the help of macro files it is easy to generate an optimal view. The most important commands will be explained in the following.

All parts of the detector can be made visible or invisible in the viewer.

- vis/geometry/set/visibility Part_log 0 true/false
  In a Geant4 simulation it is not always useful to see the full geometry. So, for analysing the tracks of particles inside a detector, parts like cables, heat foils or the outer construction of the satellite is not of interest. As a result, in the viewer only those parts should be visualised that are of a certain interest for the user at this moment. For all other parts the visibility can be set to false.

- vis/viewer/set/style wireframe/surface
  In some cases it is useful to visualise outer construction layers but at the same time, processes taking place in inner layers should be visible. Therefore, the user can choose between surface and wire-frame display.

In order to set the image that is generated to the desired position, there are several commands for the viewer.

- vis/viewer/set/viewpointVector x y z
  By this command the point from which the geometry is looked at can be set.

- vis/viewer/set/viewpointThetaPhi theta phi
  Instead of Cartesian coordinates the viewpoint direction can also be set by defining the two angles ϑ and Φ

- vis/viewer/panTo x y
  After setting the viewpoint, the image can be shifted in the x and y direction when focusing on certain details of the setup. This is done by invoking this command.

- vis/viewer/zoom factor
  To see more details, it is possible to zoom in and out of the visualisation by stating a zoom factor greater than one (in) or smaller than one (out).

Also small details can be added to the scene like descriptions of the different parts or a coordinate system.

- vis/scene/add/text x y z cm size offset offset text
  By this command, text can be added at a certain position (x,y,z).

- vis/set/textColour colour
  The text colour can be changed to some standard colours like red, blue or green.

- /vis/scene/add/axes
  A coordinate system can be placed at the origin.

To save an image of the visualisation the following command is used.

- vis/ogl/printEPS
  This command saves an image of the visualisation in the eps-format.

The simulation itself can be controlled with some commands.

- vis/disable
  In order to save simulation time, the visualisation can be disabled.
- vis/enalbe
  To see the processes taking place during the simulation, the visualisation must be enabled. It is enabled by default.
- run/beamOn number
  The simulation is started by this command and iterates the number of events stated by *number*.
- vis/reviewKeptEvents
  It is possible to mark certain events for a further visual analysis after the simulation. Those events can be reviewed with this command. It is important to enable the visibility in case it was disabled during the simulation.

There are far more commands for the OpenGl viewer as can be described here. Especially, the general particle source can be controlled by commands. Further description can be found in the official Geant4 manual (Geant4 collaboration, 2013).

2 Derivations

2.1 Derivation of the event ellipses for stacked detectors

From the simulation or the measurement the coordinates of the interaction points $\vec{x}_1$ and $\vec{x}_2$ in the two detectors are known (see Figure 5.3). The distance d between the origin $\vec{0}$ and the source plane S has to be chosen depending on the real distance to the source.
As another important coordinate, the intersection point $\vec{x}_\mathrm{s}$ between the elongation of the connection vector $\vec{g}$ of the two interaction points, further called centre point beam, and the plane S is computed. The normal form of the plane S and the parameter form of the line g are given via

$$\mathrm{S} : z = d \tag{1}$$

$$\vec{g}(t) = \vec{x}_1 + t \cdot (\vec{x}_2 - \vec{x}_1). \tag{2}$$

The coordinates of the intersection point can be found to be

$$\vec{x}_\mathrm{s} = \vec{x}_1 + \frac{d - z_1}{z_2 - z_1} \cdot (\vec{x}_2 - \vec{x}_1) \tag{3}$$

For further calculations, the knowledge of the tilting angle β between the centre point beam and the z-direction is crucial. It can be obtained through basic vector algebra.

$$\cos(\beta) = \frac{\vec{x}_\mathrm{a} \cdot \hat{\mathrm{e}}_\mathrm{z}}{\vec{x}_\mathrm{a}}, \tag{4}$$

where $\vec{x}_\mathrm{a}$ is the connecting vector between $\vec{x}_\mathrm{s}$ and $\vec{x}_1$.

With these parameters the coordinate system can be transformed into a new system which has a z-axis in the direction of the axis of symmetry of the Compton cone. To do so, in a first step the coordinate system is translated from the origin to the intersection point of the upper detector.

$$\vec{r}_\mathrm{a} = \vec{r}_0 - \vec{x}_1 = \begin{pmatrix} x - x_1 \\ y - y_1 \\ z - z_1 \end{pmatrix} \tag{5}$$

In the next step the system is rotated around an axis that is normal to the plane which contains the difference vector of the two interaction points and the original z-axis.

$$\vec{n} \cdot \vec{\mathrm{e}}_z = 0 \tag{6}$$

$$\vec{n} \cdot (\vec{x}_1 - \vec{x}_2) = n_1(x_1 - x_2) + n_2(y_1 - y_2) + n_3(z_1 - z_2) \tag{7}$$

The normal vector can be obtained as:

$$n_3 = 0 \tag{8}$$

$$n_1 = p \tag{9}$$

$$n_2 = -p\frac{(x_1 - x_2)}{(y_1 - y_2)} \tag{10}$$

with

$$p = \sqrt{\frac{(y_1 - y_2)^2}{(x_1 - x_2)^2 - (y_1 - y_2)^2}}. \tag{11}$$

Thus, the rotation axis is found to be

$$\vec{n} = \sqrt{(\Delta x)^2 + (\Delta y)^2} \begin{pmatrix} \Delta y \\ -\Delta x \\ 0 \end{pmatrix} \tag{12}$$

$$\Delta x = x_1 - x_2 \tag{13}$$

$$\Delta y = y_1 - y_2 \tag{14}$$

The general form for a rotation α around an arbitrary axis $\vec{n}$ is

$$R_n^\alpha = \begin{pmatrix} n_1^2(1-\cos(\alpha)) + \cos(\alpha) & n_1 n_2(1-\cos(\alpha)) + n_3\sin(\alpha) & n_1 n_3(1-\cos(\alpha)) - n_2\sin(\alpha) \\ n_2 n_1(1-\cos(\alpha)) - n_3\sin(\alpha) & n_2^2(1-\cos(\alpha)) + \cos(\alpha) & n_2 n_3(1-\cos(\alpha)) + n_1\sin(\alpha) \\ n_3 n_1(1-\cos(\alpha)) + n_2\sin(\alpha) & n_3 n_2(1-\cos(\alpha)) - n_1\sin(\alpha) & n_3^2(1-\cos(\alpha)) + \cos(\alpha) \end{pmatrix} \tag{15}$$

The new coordinate system can be found via

$$\vec{r}_\mathrm{b} = \begin{pmatrix} (x-x_1)[n_1^2(1-\cos(\beta)) + \cos(\beta)] + (y-y_1)n_1 n_2(1-\cos(\beta)) + (z-z_1)n_2\sin(\beta) \\ (x-x_1)n_2 n_1(1-\cos(\beta)) + (y-y_1)[n_2^2(1-\cos(\beta)) + \cos(\beta)] - (z-z_1)n_1\sin(\beta) \\ -(x-x_1)n_2\sin(\beta) + (y-y_1)n_1\sin(\beta) + (z-z_1)\cos(\beta) \end{pmatrix} \tag{16}$$

In this new system the intersection line of the cone with the plane is circular. By setting z equal to the distance of the source and inserting the new coordinates in the circle formula

$$x_\mathrm{b}^2 + y_\mathrm{b}^2 - z_\mathrm{b}^2\tan(\alpha) = 0 \tag{17}$$

a formula for the intersection ellipses can be obtained.

3 Description of the software used for evaluation of the simulated data

3.1 Describtion of the software for histogram evaluation

For the evaluation of the quantum efficiency measurement and the energy spectra of the CANDELA measurement the Python program **histo_main.py** is used. The handling of the provided functions will be described in this section.

- **set_style(style, title, xlimd=None, xlimu=None, xscale=None, yscale=None, ylimd=None, ylimu=None, xlabel=None, ylabel=None)**
  The program can be used for the handling of all kinds of histograms. For the evaluation of quantum efficiency data and energy spectra some plot settings are predefined. By choosing the *style* 'QE', the y range (*ylimd*, *ylimu*) is set to [0:105], the x axis is set to a logarithmic scale and the axis (*xlabel*, *ylabel*) are labeled with **Energy of the incident particles [keV]** and **Quantum efficiency [%]**. The title of the plot has to be inserted.
  The *style* 'EneSpec' has a linear x scale and a logarithmic y scale. The axes are labeled **Detected energy [keV]** and **Frequency of occurence [cnt/s/keV]**.
  All style parameters can also be changed.

- **add_events(pathname)**
  By indicating a pathname in this function a data file can be loaded. The data must be allocated in csv-format.

- **read_in(self, filehandle, div=None)**
  Also data that is not provided in the csv format can be loaded. This is done by this function. Additionally, it is possible to norm the data in the column 1 (when 0 is the first column) to a certain value. Therefore a non-None value has to be set for the parameter *div*.

- **do_histo(self, column, step, fcol=None, fval=None)**
  do_histo creates a histogram from the read in data. On that account it is necessary to set the column number corresponding to the requested data. Additionally, one has to define a step width in keV. It is also possible to filter rows after a certain value *fval* in a certain column *fcol*.

- **add_histo()**
  If existing histograms are loaded by the *read_in* function, the histogram does not have to be sorted again, so it has to be inserted with this function.

- **divide_histo(histogram)**
  Histograms can be normalised in two ways. By using **divide_histo** a created histogram can be divided by another one, for instance the corresponding input spectrum.

- **norm_histo(norm)**
  The second way of normalising is dividing by a certain value *norm*. All values of the histogram are then divided by this value.

- **offset_histo(offset)**
  An offset in the binning can be included by defining an *offset* value.

- **running_average()**
  When working with a logarithmic scale it is sometimes useful to avoid zeros between values unequal to zero. A running average can minimise this problem if not too many values are zero. Each value is summed up with its neighbouring values and divided by three. The progression of the curves are smoother and easier to fit.

- **plot_histo(name, output = None)**
  This function shows the calculated histogram and saves it under the path of the original data extended by a stated name. The resulting file is in the pdf-format. Additionally, it is possible to save the raw data of the histogram in a csv-file by setting *output* to 'y'.

- **join_histo(name_plot, name1, histo2, name2, histo3 = None, name3 = None, ..., grid=None)**
  With this function up to five histograms can be plotted together in a common image with a corresponding legend. The parameter *plot_name* works as an extension for the name the plot is saved under. If required, a grid can be added by setting *grid* to 'y'.

All functions can be combined in order to evaluate data in form of histograms.

3.2 Handling of the evaluation software for a Compton telescope measurement

The Python program **compton_main.py** was used for evaluating a Compton telescope measurement. It contains the following tools.

- **add_events(pathname)**:
  As before *add_events* loads the requested data. The input file has to contain 13 columns: point of time for the interaction in the first and second detector, one value for the detected energy, three coordinates for the position of the first interaction, number of interactions for each detector and input energy of the generated photon. The last two values are for statistical analysis. Again the file is in the csv-format.

- **do_analysis(scatangle, Fano=None)**:
  This function sorts the recorded data. Events for which the point of time of the first and second interaction differ only by one nano second and in which energy was deposited in both detectors, are classified as valid. For these events, the tool calculates the vector connecting the two points of interaction as well as the total deposited energy. Using the energy it computes the scattering angle like it is deduced in 5.3. If the argument of the cosine is found to be out of domain, the event is rejected. As mentioned above, these are cases of backscattering or electron emission which can not be used for the reconstruction of the source position. Also by stating a maximal energy for the upper detector another suppression of false events can take place.

  In the end, the coordinates of the interaction in the higher detector, the connection vector, the single deposed and the total energy, the angle α as well as a statistical value indicating the kind of event (fully absorbed, partly absorbed, false events) are saved. For the case of a realistic linewidth evaluation, the Fano width has to be taken into account. Then, energy differing by the half Fano width from the input energy is still considered as fully detected.

- **do_reconstruct(distance)**:
  This tool takes the distance of the source plane from the detector as a parameter. Using the results provided by *do_analysis*, intersection points of the symmetry axis and the plane as well as tilting angles β of the cone were calculated with the methods in 5.3.

- **parameter(bin width, field of view)**:
  In this function the parameters for the calculation of the ellipses are derived which are the used bins and the trigonometrical functions for the angles α and β.

- **find_first()**:
  With **find_first** one bin that lies on the ellipse should be found so that the algorithm in the next step can work. Therefore, the function *calc_ellipse* using formula 5.9 is evaluated for all bins in x direction with a fixed y value. From this, the minimal value of the absolute values is searched. Again *calc_ellipse* is evaluated for all bins in y direction with the value of x that corresponds to the minimal value found for the first evaluation. By again taking the minimal value, a value is found that is closest to the ellipse and should hence lie on the ellipse.

- **do_ellipse()**:
  In **do_ellipse** the algorithm from 5.3 is implemented. So the tool searches for the

neighbouring bins that lie on the ellipses. If it finds a bin on the edge of the field of view, it starts again, with the first value and follows the other direction. When finding the same value twice it concludes that the full ellipse is found and starts with the next one, till all ellipses are found. The found coordinates of the bins are saved in a so called hitlist.

- **do_histo(step width, name)**:
  From the provided hitlist a two-dimensional histogram is generated. Step width in degree and name extension for saving were given as parameters. In this step the positions in the list were recalculated from mm units in degree in dependency on the previous given distance between plane and detector. In the resulting histogram, it has to be considered that the x position is plotted upwards, the y position to the right.

- **fit_plot1D(name)**:
  To reconstruct the true position of the source, the histogram has to be fitted with **fit_plot1D**. The application searches for the maximum of the histogram and places a Gaussian curve over the data of the column respectively the row containing this maximum. Images of the fitted data, mean and standard deviation are saved in png- and csv-format. Again a name extension can be stated.

These tools permit a complete analysis of a Compton camera simulation or measurement. For visualisation of the processes during the measurement, two more applications are provided.

- **do_hitmap(energy column, x column, size x, size y, pixel, name)**:
  For the evaluation of the illumination of a detector **do_hitmap** can be used. The columns containing the deposed energy and the corresponding x coordinate of the interaction were given as parameters. Additionally, the program needs the declaration of the half size of the detector in x and y direction in mm as well as the number of pixel. With a name extension the hitmap can be assigned to one of the detectors. From the source file, the application generates a histogram stating the frequency of a hit in the detector at a certain pixel.

- **do_statistics(number of photons)**:
  For a defined number of generated photons a short summary of the statistical parameters is shown by **do_statistics**. For this purpose, it names the number of valid events with full energy deposit, partly deposition and false events like backscattering or electron production together with the total number of hits in both detectors. The results were shown in the control panel and additionally saved as a csv-file with the given name extension and the suffix 'QE'.

4 Tables

4.1 Tabulated values for the quantum efficiency measurement

Table 1 Tabulated values for the quantum efficiency measurment by Granato (2012). The table states the quantum efficiency measured at the given input energies as well as the corresponding error.

Energy [keV]	QE [%]	Error [%]
0.200	2.0	±0.1
0.250	8.3	±0.1
0.280	13	±0.2
0.320	21	±0.3
0.380	36	±1
0.398	40	±2
0.404	31	±1
0.410	35	±1
0.480	53	±2
0.534	60	±2
0.538	48	±2
0.560	55	±2
0.600	65	±2
0.800	83	-3/+7
1.250	95	±2
1.540	93	±3
1.559	79	±6
1.564	64	±5
1.600	77	±6
1.800	86	-3/+2
1.840	83	±2
1.849	74	±2
1.880	82	±2
2.500	93	±1
3.000	95	±1
4.000	97	±2
7.000	99	±2
10.000	95	±2
11.000	92	±2

4.2 Reconstructed positions of different simulated positions for a Compton telescope

Table 2 Reconstruction of the source position in a Compton telescope measurement for different true source positions between $(0°, \pm 17°)$. The first two columns contain the true source position in angular units. The *mean* columns provide the calculated mean values found in the measurement, the *sigma* columns the standard deviation. It can be observed, that the mean values are close to the true positions.

alpha y	alpha x	mean y	sigma y	mean x	sigma x
-16.699	0.000	-17.293	9.779	0.077	9.849
-16.172	0.000	-16.446	9.939	-0.144	10.213
-15.642	0.000	-16.117	10.220	-0.311	9.988
-15.110	0.000	-15.715	9.725	0.186	10.240
-14.574	0.000	-15.253	9.930	0.076	9.552
-14.036	0.000	-14.387	11.056	0.071	9.990
-13.496	0.000	-13.850	10.026	0.521	10.103
-12.953	0.000	-13.074	9.945	0.154	9.576
-12.407	0.000	-12.754	10.084	-0.143	10.393
-11.860	0.000	-12.234	9.800	-0.011	10.461
-11.310	0.000	-11.691	10.931	0.058	10.051
-10.758	0.000	-10.969	9.922	-0.312	9.559
-10.204	0.000	-10.362	10.211	0.207	10.447
-9.648	0.000	-9.615	10.452	0.179	9.822
-9.090	0.000	-9.152	9.560	0.081	9.956
-8.531	0.000	-9.028	9.672	-0.248	10.066
-7.970	0.000	-8.498	10.778	-0.037	9.608
-7.407	0.000	-7.701	10.175	0.240	10.140
-6.843	0.000	-6.754	10.178	-0.061	10.159
-6.277	0.000	-6.165	10.733	0.209	10.175
-5.711	0.000	-5.934	9.971	0.125	9.735
-5.143	0.000	-5.509	10.442	0.280	9.744
-4.004	0.000	-3.948	10.544	-0.125	9.830
-3.434	0.000	-3.167	10.187	-0.019	10.163
-2.862	0.000	-2.954	10.267	-0.310	9.788
-2.291	0.000	-2.057	10.117	0.062	9.547
-1.718	0.000	-1.578	10.752	-0.117	10.054
-1.146	0.000	-0.879	9.641	-0.246	9.798
-0.573	0.000	-0.478	10.034	-0.133	9.738
0.000	0.000	-0.210	9.870	0.104	10.828
0.573	0.000	0.512	10.055	0.029	10.245
1.146	0.000	1.066	9.832	0.042	9.797
1.718	0.000	1.989	9.812	0.278	10.186
2.291	0.000	2.799	10.481	-0.069	10.064
2.862	0.000	3.268	10.189	-0.055	10.725
3.434	0.000	3.838	9.713	0.106	9.451
4.004	0.000	3.946	9.963	-0.030	10.202

4.574	0.000	4.599	9.987	-0.032	9.751
5.143	0.000	5.618	10.083	0.060	10.528
5.711	0.000	5.970	9.963	-0.156	9.892
6.277	0.000	6.682	9.545	-0.073	9.512
6.843	0.000	7.310	9.550	-0.363	10.581
7.407	0.000	7.759	9.748	0.013	11.271
7.970	0.000	8.296	9.539	-0.289	9.535
8.531	0.000	8.654	10.313	-0.003	10.712
9.090	0.000	9.477	11.020	-0.071	11.176
9.648	0.000	10.173	9.368	0.142	10.006
10.204	0.000	10.262	10.506	-0.324	9.740
10.758	0.000	11.314	9.475	0.302	10.598
11.310	0.000	11.635	10.635	-0.077	10.274
11.860	0.000	12.369	9.978	0.067	10.571
12.407	0.000	12.990	9.378	0.214	10.726
12.953	0.000	13.740	9.560	-0.115	10.525
13.496	0.000	13.826	10.202	-0.130	11.295
14.036	0.000	14.333	10.207	0.524	11.652
14.574	0.000	15.559	9.049	0.131	10.133
15.110	0.000	15.656	10.679	0.448	10.079
15.642	0.000	16.442	9.527	-0.060	10.920
16.172	0.000	16.596	10.772	-0.183	10.692
16.699	0.000	17.352	9.875	-0.163	10.583

4.3 X-ray emission lines of the materials used in the CANDELA setup

Table 3 X-ray emission lines of the materials used in the CANDELA setup. All values are given in keV. The data is taken from the X-ray data booklet (Center for X-Ray Optics Advanced Light Source, 2001)

#	Element	$K_{\alpha 1}$	$K_{\alpha 2}$	$K_{\beta 1}$	$K_{\beta 2}$
13	Al	1.48670	1.48627	1.55745	
14	Si	1.73998	1.73938	1.83594	
24	Cr	5.41472	5.405509	5.94671	
26	Fe	6.40384	6.39084	7.05798	
28	Ni	7.47815	7.46089	8.26466	
29	Cu	8.04778	8.02783	8.90529	
48	Cd	23.1736	22,9841	26,0955	26.6438
50	Sn	25.2713	25.0440	28.4860	29.1093
52	Te	27.4723	27.2017	30.9957	31.7004

List of Figures

List of Tables

Bibliography

R. Giacconi, H. Gursky, and L. P. van Speybroeck. Observational Techniques in X-Ray Astronomy. *Annual Review of Astronomy and Astrophysics Volume 6, p. 373-416*, 1968.

H. Friedman, S. W. Lichtman, and E. T. Byram. Photon Counter Measurements of Solar X-Rays and Extreme Ultraviolet Light. *Physical Reviews 83, p. 1025*, 1951.

R. Giacconi, H. Gursky, F. R. Paolini, and B. B. Rossi. Evidence for x Rays From Sources Outside the Solar System. *Physical Review Letters 9, p. 439*, 1962.

J. Trümper, K. Dennerl, and J. Englhauser. X-Ray Transients — Results of Rosat Observations. *Highlights of Astronomy, Volume 11B*, 1999.

M. C. Weisskopf, H. Tananbaum, W. Tucker, B. Wilkes, R. Baggett, R. Brissenden, P. Edmonds, and E. Mattison. Fifteen years of Chandra operation: scientific highlights and lessons learned . *Proceedings of SPIE 9144*, 2014.

F. Jansen, D. Lumb, B. Altieri, J. Clavel, M. Ehle, C. Erd, C. Gabriel, M. Guainazzi, P. Gondoin, R. Much, R. Munoz, M. Santos, N. Schartel, D. Texier, and G. Vacanti. XMM-Newton observatory. I. The spacecraft and operations. *Astronomy and Astrophysics, v.365, p.L1-L6*, 2001.

N. Schartel. XMM-Newton highlights. *Memorie della Società Astronomica Italiana, Volume 83, p. 97*, 2012.

E. Novotny. *Introduction to stellar atmospheres and interiors*. Oxford University Press, 1973.

A. Feldmeier, R.-P. Kudritzki, R. Palsa, A.W.A. Pauldrach, and J. Puls. The X-ray emission from shock cooling zones in O star winds. *Astronomy and Astrophyics, 320, p. 899-912*, 1997.

M. Gagné, G. Fehon, M. R. Savoy, D. H. Cohen, L. K. Townsley, P. S. Broos, M. S. Povich, M. F. Corcoran, N. R. Walborn, N. R. Evans, A. F.J. Moffat, Yaël Nazé, and L. M. Oskinova. Carina OB Stars: X-ray Signatures of Wind Shocks and Magnetic Fields. *CCCP OB Signatures Paper*, 2011.

G. L. Withbroe and R. W. Noyes. Mass and energy flow in the solar chromosphere and corona. *Annual review of astronomy and astrophysics. Volume 15, p. 363-387*, 1977.

S. G. Ryan and A. J. Norton. *Stellar Evolution and Nuclearsynthesis*. Cambridge University Press, 2010.

M. Salaris. White dwarf cosmochronology: Techniques and uncertainties. *Proceedings IAU Symposium No.258*, 2008.

E. Kuulkers, A. Norton, A. Schwope, and B. Warner. X-rays from Cataclysmic Variables. *Compact stellar X-ray sources*, 2003.

C. Hellier. *Cataclysmic Variable Stars.* Springer-Praxis books in astronomy and space sciences, 2001.

A. Weigert, H.J. Wendker, and L. Wisotzki. *Astronomie und Astrophysik, 5. Auflage.* Wiley-VCH, 2010.

E. Treister P. Natarajan. Is there an upper limit to black hole masses? *Monthly Notices of the Royal Astronomical Society 393, p. 838-845*, 2009.

R. Ruffini and J. A. Wheeler. Introducing the black hole. *Physics Today 24, 1, p. 30-41*, 1971.

D. L. Meier. *Black Hole Astrophysics - The Engine Paradigm.* Springer-Verlag Berlin Heidelberg, 2012.

P. Gandhi. X-ray studies of Active Galactic Nuclei. *Asian Journal of Physics 13, 90*, 2005.

J. Vink. Supernova remnants: the X-ray perspective. *Astronomy and Astrophysics Reviews, Vol. 20, No 1*, 2012.

P. A. Charles and F. D. Seward. *Exploring the X-ray universe.* Cambridge University Press, 1995.

S. Mineo. *X-ray emission from star-forming galaxies.* PhD thesis, Ludwig–Maximilians–Universität München, 2011.

C. L. Sarazin. X-ray emission from clusters of galaxies. *Reviews of Modern Physics , Vol. 58, No. 1*, 1986.

H. Kramers. On the theory of X-ray absorption and the continuous X-ray spectrum. *Philosophical Magazine Series 6 Volume 46, Issue 275*, 1923.

W. Demtröder. *Experimentalphysik 4: Kern-, Teilchen- und Astrophysik, 3. Auflage.* Springer, 2010.

G. B. Rybicki and A. P. Lightman. *Radiative Processes in Astrophysics.* Wiley-VCH Verlag GmbH, Weinheim, 2004.

M. Planck. Ueber das Gesetz der Energieverteilung im Normalspectrum. *Annalen der Physik, Volume 309, 3*, 1901.

Particle Data Group. *Particle Physics Booklet.* Regents of the University of California, 2014.

H. Wolter. Spiegelsysteme streifenden Einfalls als abbildende Optiken für Röntgenstrahlen . *Annalen der Physik, 10, p. 94–114.*, 1952.

B. Aschenbach. Realization of X-ray telescopes—from design to performance. *Experimental Astronomy 26, p. 95–109*, 2009.

J. B. Birks. *The theory and practice of scintillation counting.* Braunschweig: Pergamon Pr., 1967.

E. Gatti and P. Rehak. Semiconductor Drift Chamber - An Application of a Novel Charge Transport Scheme. *Nuclear Instruments and Methods in Physics Research A 225, p. 608-614*, 1983.

S. Send. *Utilization of a frame store pnCCD for energy-dispersive Laue diffraction with white synchrotron radiation.* PhD thesis, Naturwissenschaftlich-Technischen Fakultät der Universität Siegen, 2013.

W. S. Boyle and G.E. Smith. Charge Coupled Semiconductor Devices. *B.S.T.J. briefs 49*, 1970.

D. E. Gruber, J. L. Matteson, L. E. Peterson, and G. V. Jung. The Spectrum of Diffuse Cosmic Hard X-Rays Measured with HEAO–1. *The Astrophysical Journal 520, 124*, 1999.

H. Katayama, I. Takahashi, Y. Ikebe, K. Matsushita, Y. Tanaka, and M. Freyberg. PROPERTIES OF THE BACKGROUND OF EPIC ONBOARD XMM-NEWTON. *Astronomy and Astrophysics 414, p. 767-776*, 2004.

E. Pfeffermann, N. Meidinger, L. Strüder, H. Bräuninger, and G. Hartner. Lessons learned from the EPIC pn-CCD camera for future missions. *Memorie della Società Astronomica Italiana 75, 555*, 2004.

S. Ebermayer, R. Andritschke, J. Elbs, N. Meidinger, L. Strüder, R. Hartmann, A. Gottwald, M. Krumrey, and F. Scholze. Quantum efficiency measurements of eROSITA pnCCDs. *Proceedings of SPIE 7742 no. 1*, 2010.

D. Maier. *Development of stacked detector system and its application as an X-ray polarimeter.* PhD thesis, Universität Tübingen, 2014.

W. L. Dunn and J. K. Shultis. *Exploring Monte Carlo Methods.* Academic Press, 2011.

N. Metropolis. The Beginning of the Monte Carlo Method. *Los Alamos Science*, page pp. 125–130 Special issue, 1987.

S. Agostinelliae, J. Allisonas, K. Amakoe, J. Apostolakisa, H. Araujoaj, P. Arcel, M. Asaig, D. Axeni, S. Banerjeebi, G. Barrandan, F. Behnerl, L. Bellagambac, J. Boudreaubd, L. Brogliaar, A. Brunengoc, H. Burkhardta, S. Chauviebj, J. Chumah, R. Chytraceka, G. Coopermanaz, G. Cosmoa, P. Degtyarenkod, A. Dell'Acquaa, G. Depaolay, D. Dietrichaf, R. Enamiab, A. Feliciellobj, C. Fergusonbh, H. Fesefeldtl, G. Folgera, F. Foppianoac, A. Fortias, S. Garelliac, S. Giania, R. Giannitrapanibo, D. Gibinm, J.J. Gómez Cadenasm, I. Gonzálezq, G. Gracia Abriln, G. Greeniausp, W. Greineraf, V. Grichinef, A. Grossheimm, S. Guatelliad, P. Gumplingerh, R. Hamatsubk, K. Hashimotoab, H. Hasuiab, A. Heikkinenah, A. Howardaj, V. Ivanchenkoa, A. Johnsong, F.W. Jonesh, J. Kallenbachaa, N. Kanayai, M. Kawabataab, Y. Kawabataab, M. Kawagutiab, S. Kelnerat, P. Kentr, A. Kimuraay, T. Kodamaaw, R. Kokoulinat, M. Kossovd, H. Kurashigeam, E. Lamannaw, T. Lampénah, V. Laraa, V. Lefeburel, F. Leibh, M. Liendll, W. Lockmanj, F. Longobm, S. Magnik, M. Maireao, E. Medernacha, K. Minamimotoaw, P. Mora de Freitasap, Y. Moritae, K. Murakamie, M. Nagamatuaw, R. Nartallob, P. Nieminenb, T. Nishimuraab, K. Ohtsuboab, M. Okamuraab, S. O'Neales, Y. Oohatabk, K. Paechaf, J. Perlg, A. Pfeiffera, M.G. Piaad, F. Ranjardn, A. Rybinak, S. Sadilova, E. Di Salvoc, G. Santinbm, T. Sasakie, N. Savvasas, Y. Sawadaab, S. Schereraf, S. Seiaw, V. Sirotenkoi, D. Smithg, N. Starkovf, H. Stoeckeraf, J. Sulkimoah, M. Takahataay, S. Tanakabg, E. Tcherniaeva, E. Safai Tehranig, M. Tropeanoae, P. Truscottbe, H. Unoaw, L. Urbanv, P. Urbanaq, M. Verderiap, A. Walkdenas, W. Wanderav, H. Weberaf, J.P. Wellischa, T. Wenausu, D.C. Williamsj, D. Wrightg, T. Yamadaaw, H. Yoshidaaw, and D. Zschiescheaf.

Geant4—a simulation toolkit. *Nuclear Instruments and Methods in Physics Research Section A: Accelerators, Spectrometers, Detectors and Associated Equipment*, 2003.

Geant4 collaboration. Geant4 User's Guide for Application Developers, Version: geant4 10.0. http://geant4.web.cern.ch/geant4/UserDocumentation/UsersGuides/ ForApplicationDeveloper/fo/BookForAppliDev.pdf, 2013. [Online; accessed 11-July-2014].

ESA. Geant4 Space Users. http://geant4.esa.int/index.php/g4-space-users.html, 2014. [Online, accessed 11-July-2014].

W. R. Leo. *Techniques for Nuclear and Particle Physics Experiments.* Springer-Verlag Berlin Heidelberg New York, 1994.

D. W. Aitken, W. L. Lakin, and H. R. Zullinger. Energy Loss and Straggling in Silicon by High-Energy Electrons, Positive Pions, and Protons. *Physical Review 179, p.178*, 1969.

P. Predehl. eROSITA – Mapping the X-ray universe. *Astronomische Nachrichten, Volume 335, No. 5, 517-522*, 2014.

P. Predehl. The Platinum Age. `http://www.uni-tuebingen.de/index.php?eID=tx_nawsecuredl&u=0&file=fileadmin/Uni_Tuebingen/Fakultaeten/MathePhysik/Institute/IAAT/AIT/Publikationen/Konferenzen/Eckhard65/Predehl_P_eROSITA_T%C3%BCbingen_2010.pdf&t=1396089958&hash=c8b972f531ee851c4d9cab8a60dbc8765dc1e807`, 2010. [Online, accessed 11-July-2014].

S. Granato. *The response of silicon PNCCD sensors with aluminum on-chip filter to visible light, UV- and X-ray radiation.* PhD thesis, Universität Siegen, 2012.

Center for X-Ray Optics Advanced Light Source. *X-Ray Data Booklet.* Lawrence Berkeley National Laboratory, 2001.

D. Maier, O. Limousin, A. Meuris, S. Pürckhauer, A. Santangelo, T. Schanz, and C. Tenzer. Development of a stacked detector system for the x-ray range and its possible applications . *Proceedings of SPIE 9154*, 2014.

V. Schönfelder. Das Compton-Teleskop. *Mitteilungen der Astronomischen Gesellschaft, Vol. 54, p.117*, 1981.

J. Gerl S. Tashenov. TANGO - New tracking AlGOrithm for gamma-rays. *Nuclear Instruments and Methods in Physics Research Section A Accelerators Spectrometers Detectors and Associated Equipment, Volume 622, p. 592*, 2010.

C. Gouiffès, P. Laurent, and P. Ferrando. Prospects in polarimetry with the Simbol-X mission. In *Polarimetry days in Rome: Crab status, theory and prospects*, 2008.

CNES. The project main steps. http://smsc.cnes.fr/SIMBOLX/, 2011. [Online, accessed 11-July-2014].

R. B. Firestone and L.P. Ekström. WWW Table of Radioactive Isotopes, database version 2/28/99. http://ie.lbl.gov/toi/index.htm, 2008. [Online, accessed 11-July-2014].

H. Spieler. *Semiconductor Detector Systems.* Oxford University Press, 2006.

G. Lutz. *Semiconductor Radiation Detectors.* Springer-Verlag Berlin Heidelberg New York, 2001.

T. Takahashi, T. Mitani, Y. Kobayashi, M. Kouda, G. Sato, S. Watanabe, K. Nakazawa, Y. Okada, M. Funaki, R. Ohno, and K. Mori. High Resolution Schottky CdTe Diode Detector. *IEEE Transactions on nuclear science 49, p. 100*, 2002.

K. Nandra, D. Barret, X. Barcons, A. Fabian, J. den Herder, L. Piro, and M. Watson. Athena: The Advanced Telescope for High-Energy Astrophysics. *Misson proposal submitted on behalf of the Athena team*, 2014.

A. Rau, N. Meidinger, K. Nandra, M. Porro, D. Barret, A. Santangelo, C. Schmid, J. Wilms L. Strüder, C. Tenzer, C. Amoros, R. Andritschke, F. Aschauer, A. Bähr, B. Günther, M. Fürmetz, B. Ott, E. Perinati, D. Rambaud, J. Reiffers, J. Treis, A. von Kienlin, and G. Weidenspointner. The Hot and Energetic Universe - The Wide Field Imager (WFI) for Athena+. *ATHENA X-Ray Observatory, online published*, 2013.

S. Hauf. *Studies on the Background of the Wide Field Imager aboard the IXO and ATHENA X-Ray Telescopes*. PhD thesis, Technische Universität Darmstadt, 2012.

Eidesstattliche Erklärung

Ich, Sabina Pürckhauer, Matrikel-Nr. 3260368, versichere hiermit, dass ich meine Diplomarbeit mit dem Thema

Simulation studies of the expected background for X-ray missions

nach §18 Abs. 7 der Diplom-Prüfungsordnung selbstständig verfasst und keine anderen als die angegebenen Quellen und Hilfsmittel benutzt habe, wobei ich alle wörtlichen und sinngemäßen Zitate als solche gekennzeichnet habe. Die Arbeit wurde bisher keiner anderen Prüfungsbehörde vorgelegt und auch nicht veröffentlicht.

Tübingen, den 28. Januar 2015

Sabina Pürckhauer

Statutory declaration

I hereby certify that the diploma theses entitled

Simulation studies of the expected background for X-ray missions

based on section 18 (7) of the examination regulation is entirely my own work except where otherwise indicated. Passages and ideas from other sources have been clearly indicated. This work has not yet been submitted to any testing authority and has not been published so far.

Tübingen, January 28, 2015

Sabina Pürckhauer

Danksagung

Abschließend möchte ich all denen danken, die mich während meines gesamten Studiums und in der Abschlussphase im Besonderen begleitet und gefördert haben.

Ich danke **Prof. Dott. Andrea Santangelo** für die Betreuung meiner Diplomarbeit und auch dafür, dass er durch seinen ganz besonderen Vorlesungsstil mein Interesse an der Astrophysik geweckt hat.
Außerdem danke ich **Dr. Chris Tenzer** für sein Engagement, jede Menge Feedback und konkrete Hilfestellungen beim Simulieren und Schreiben.
Auch geht mein Dank an die Kollegen vom Institut für Astronomie und Astrophysik Tübingen, darunter ganz besonders an **Daniel Maier**, für seine Hilfe bei physikalischen Fragestellungen, die ich teilweise noch gar nicht als solche erkannt hatte und für das Korrekturlesen in einer Zeit, in der er mit dem Schreiben seiner Doktorarbeit sicher schon genug zu tun gehabt hätte.
Selbiges gilt für **Sebastian Diebold**, der mich nicht nur während meines Hiwi-Jobs betreute und auf der Rosenau seinen Kuchen mit mir teilte, sondern sich auch meines Englischs in der Diplomarbeit angenommen hat.
Für Hilfestellungen bei der englischen Sprache danke ich Wiebke Mollik und Neil Heckman.

Weiterhin danke ich meiner Familie für ihre Unterstützung in dieser doch oft stressigen Zeit. Meiner Mutter **Ursula Pürckhauer** für den dauernden Zuspruch, auch wenn sie immer wieder betonte, dass wir das Naturwissenschaftliche nicht von ihr geerbt hätten, meiner Schwester **Tanja Pürckhauer**, dafür, dass sie mich immer angetrieben hat, auch dann wenn es noch gar nicht nötig war, meiner Tante **Evi Pürckhauer**, für ihren professionellen Blick und die schnelle und kurzfristige Organisation von englischsprachigen Korrekturlesern, meinen Großeltern **Ingeborg Pürckhauer**, **Willi** und **Luise Scherer**, dafür dass sie mir jeden Tag wieder zeigen, was Durchhaltevermögen wirklich bedeutet, **Walter Funk**, nicht nur für die finanzielle Unterstützung sondern auch für sein stetes Interesse an mir und meiner Arbeit und **Karin Klein**, für ihr Interesse an Elementarteilchen und Sternen, auch wenn es manchmal sehr verwirrend gewesen sein muss.

Auch möchte ich mich bei allen „Sozraumbewohnern“ bedanken, für ein Band, das hoffentlich auch die Minkowski-Metrik aushält und zu jeder Zeit und an jedem Ort stabil bleibt. Insbesondere geht mein Dank an **Jennifer Bayer** für regelmäßige Programmierwochenenden, bei denen immer nur Kuchen herauskam, an **Erik Hänel** für die vielen Montagabende im Bierkeller, an denen ich den Unistress wieder abschütteln konnte, an **Martin Schmidt** für den Witz mit dem Architekten und Sommertage am Baggersee, an **Daniel Wehner** für die Lasagne und die Hilfe, wenn mich Python wieder zur Verzweiflung brachte, an **Caroline Arnold** für viele Clubhausabende vor und hinter der Theke, an **Matthias Kesenheimer** für unerschütterliche gute Laune und einen Optimismus, von dem ich bis dato glaubte, man käme damit nicht durchs Leben, an **Malte Lütje** für Spiele- und Grillabende sowie dauernde Postillion-Zitate, an **Berthold Reisz** für gemeinsame Wanderausflüge, an **Moritz Stoll** für seinen unvergleichlichen Filmgeschmack, auch wenn ich die besten Sachen bislang nur aus

Erzählungen kenne, **Cornelia Klatt** für die Kekse und **Inka Wolf** für Fachschaftssitzungen, bei denen Baldriantee ausgegeben werden musste.

Mein ganz besonderer Dank gilt meinem Freund **Dennis Aldorf** für die Ruhe, die er ausstrahlt, wenn das Chaos zu groß zu werden scheint. Für geduldiges Korrekturlesen und inhaltliche Diskussionen. Für seine andere Sicht auf die Dinge. Und einfach nur dafür, dass er immer da ist.